Formation of metal nano-size clusters with a DC magnetron-based gas aggregation source

Inauguraldissertation

zur

Erlangung des akademischen Grades eines

Doktors der Naturwissenschaften (Dr. rer. nat.)

der

Mathematisch-Naturwissenschaftlichen Fakultät

der

Ernst-Moritz-Arndt-Universität Greifswald

vorgelegt von

Marina Ganeva

geboren am 27. Juli 1979

geboren in Karelia, Russland

- Greifswald, 2013 -

Dekan:	Prof. Dr. Klaus Fesser
1. Gutachter:	Prof. Dr. Rainer Hippler
2. Gutachter:	Prof. Dr. Hynek Biederman
Tag der Promotion:	21.06.2013

It's a kind of scientific integrity, a principle of scientific thought that corresponds to a kind of utter honesty — a kind of learning over backwards. For example, if you're doing an experiment, you should report everything that you think might make it invalid — not only what you think is right about it; other causes that could possibly explain your results; and things you thought of that you've eliminated by some other experiment, and how they worked — to make sure the other fellow can tell they have been eliminated.

Details that could throw doubt on your interpretation must be given, if you know them. You must do the best you can — if you know anything at all wrong, or possibly wrong — to explain it.

Richard P. Feynman, Cargo Cult Science

Contents

List of symbols and abbreviations

Symbol	Quantity
z_a	atomic number
m_a	atomic mass
ρ	density
T_m	melting temperature
E_{ion}	energy of ionization
r_W	Wigner-Seitz radius, $\left(\frac{3m_a}{4\pi\rho}\right)^{1/3}$
E_{Ar^+}	energy of incident Ar^+ ions (sputtering)
ϵ_0	atomic binding energy in a bulk metal at the melting point
Y	sputtering yield
K	rate constant of a three-body process $2\text{M} + \text{Ar} \rightarrow \text{M}_2 + \text{Ar}$
k_0	reduced rate constant for a cluster collision with a parent atom
k_n	rate constant for a cluster collision with a parent atom
n	number of atoms in cluster
$\overline{n}$	average cluster size (atoms)
f_n	cluster size distribution function
N_{Ar}	density of argon atoms
N_{Cl}	density of clusters
N	density of free metal atoms
N_b	density of metal atoms bounded in clusters
c_b	concentration of metal atoms bounded in clusters: $c_b = N_b/N_{\text{Ar}}$
G	dimensionless parameter defined by equation (2.4)
k	Boltzmann constant
C	normalization constant
t	time
n_{cr}	critical cluster size in atoms (coalescence)
r_{cr}	critical cluster radius (coalescence)
u	reduced cluster size $u = r_c/r_{cr}$ (coalescence)
Δ	degree of superaturation (coalescence)

Symbol	**Quantity**
σ_t	inter-phase tension (coalescence)
V_{M}	atomic volume of the metal (copper or silver)
T	temperature
r_c	cluster radius
d_c	cluster diameter $d_c = 2r_c$
σ	variance
A	specific surface energy of the cluster
D_m	diffusion coefficient for metal atoms in a buffer gas
D_n	diffusion coefficient for cluster of n atoms in a buffer gas
D_0	reduced diffusion coefficient for cluster in a buffer gas
τ_r	residence time of clusters in the aggregation chamber
$\overline{x}$	displacement of the cluster in the aggregation chamber
Z_p	charge of particle, i.e. number of electrons or ions attached to the particle
T_e	electron temperature
T_i	ion temperature
m_e	electron mass
m_i	ion mass
e	elementary charge
ε_0	dielectric constant
λ	mean free path
N_+	density of positively charged clusters
N_-	density of negatively charged clusters
N_0	density of neutral clusters
N_i	ion density
N_e	electron density
σ_g	gas-kinetic cross-section
R	radius if the orifice (aggregation chamber)
w	cluster drift velocity
v_p	measured in the present work cluster drift velocity
G_o	geometrical factor
m_{Cu}	mass of the copper atom
m_{Ar}	mass of the argon atom
M	cluster mass
u_{Ar}	argon flow velocity
p	pressure
Q	argon gas flow rate
ν	number of collisions for a single cluster with the buffer gas atoms per second
N_{beam}	argon density in the beam after the orifice
σ_c	cluster cross-section $\sigma_c = \pi r_c^2$

Symbol	**Quantity**
τ	time of cluster flight from the orifice to the diagnostics, i.e. QMF detection plates
I_d	discharge current
U_d	discharge voltage
U	amplitude of the DC voltage component of the QMF rod bias
V	amplitude of the AC voltage component of the QMF rod bias
ω, f	$\omega = 2\pi f$, frequency of the AC voltage component of the QMF rod bias
a	distance of the QMF rods from the z-axis
k_c	QMF calibration factor, $k_c = 1.3$
d_q	QMF rod diameter, $d_q = 25.4$ mm
L	length of the quadrupole rod, $L = 25$ cm
ΔM_R	pass mass band for the QMF
ΔM_L	limiting QMF resolution
V_z	kinetic energy of the ions entering the QMF
E	kinetic energy of the cluster ions (RFA measurements)
ΔE	RFA resolution (full)
ATL	aggregation tube length
QMF	quadrupole mass filter
RFA	retarding field analyzer
FWHM	full width at half maximum
TEM	transmission electron microscopy
AFM	atomic force microscopy
SEM	scanning electron microscopy
EDX	energy dispersive x-ray
XPS	x-ray photoelectron spectroscopy
kMC	kinetic Monte Carlo
DSMC	direct simulation Monte Carlo
MD	molecular dynamics
IVDF	ion velocity distribution function

Chapter 1

Introduction

Clusters are aggregates of atoms or molecules, generally intermediate in size between individual atoms and aggregates large enough to be called bulk matter [1]. According to their size, clusters are classified as small, medium and large. Properties of small clusters have no simple smooth dependence on the number of component particles. By contrast, properties of medium-sized or large clusters are smoothly varying functions of the number of their component particles. Large clusters typically have dimensions in the order of a few nanometers [1]. Nano-size particles are of interest because they exhibit properties that are not found in the bulk matter [1, 2]. Nanoclusters are widely used for chemical [3–5], electronic and biomedical [6–10] applications.

The present work is focused on the investigation of cluster beams containing copper or silver clusters with sizes in the range of 1–10 nm. Copper clusters of such size are used in the production of antibacterial nanocomposites [11] and in catalysis [12, 13]. Silver nanoparticles exhibit the strongest bactericidal properties [14] and they are also used for the production of nanocomposite materials [15–19].

A cluster beam is entirely characterized by the *size* and *velocity distribution* of the clusters it contains. Both parameters determine the properties of the deposited film. Optical, electronic, catalytic and other properties (e.g. pinning on the surface [20, 21]) of the clusters strongly depend on their size [3, 4, 9, 22–26]. The properties of the deposited film also strongly depend on the size of the "building block"— cluster [22]. For example, in the case of nanocomposites, small changes in the size and shape of the nanoparticles can lead to dramatic changes in the electrical and optical properties of the material [27]. The size of silver nanoparticles is a highly important parameter that influences the interaction with cells such as bacteria [28, 29]. Many technological applications require a good control of parameters such as metal filling factor, particle size distribution and also composition of the particles [18].

The kinetic energy of clusters significantly influences the deposition process [30] and consequently, determines the characteristics of the deposited film. Three modes of cluster-surface interactions can be distinguished [31]: soft-landing, pinning and implantation of clusters. The regime of interaction affects properties of the deposited films such as wettability [31], degree of implantation of the cluster into the surface and roughness

of the film [32–34]. During the impact, the kinetic energy of the cluster is converted into internal energy, which accounts for the magnetic, electric, optical and other properties of clusters [35, 36]. Thus, control of both size and velocity distributions of nanoclusters is required for deposition of thin films with desired properties.

Typically, the cluster source consists of a vaporization source, where the free atoms are produced, and a beam apparatus, where the cluster formation takes place [1, 37, 38]. A gas aggregation source is one of the most flexible beam apparatuses in terms of cluster sizes and cluster material [37]. A magnetron sputtering source is one of the abundant techniques for thin-film deposition used since the early 1970s [39, 40]. Since the 1990s it has also been used as a vaporization source to produce cluster beams [31, 41]. Compared to the other vaporization techniques, planar magnetron-based cluster sources have a number of advantages: efficient sputtering [40], a broad cluster mass range, high deposition rate, high cluster ionization degree, etc. [41, 42]. A main disadvantage of this technique is its problematic reliability [43]. This is caused by a number of factors which are difficult to control. One of these factors is a continuous deformation of the target surface due to the sputtering. The target erosion influences the cluster size distribution [43–45], the ion distribution function in the near-cathode region [46], the deposition rate at the substrate [47], and it leads to a low target utilization. Since the problem of target utilization is of great importance for the thin film deposition industry, there are a number of solutions aimed at remedying inefficient target utilization, such as rotatable magnetrons [48, 49], target-hollow magnetrons [50] and rectangular magnetrons with full target erosion [51]. A detailed review of magnetron sputtering techniques can be found in [52, 53]. In spite of the copper nanoclusters were recently obtained using a high power pulsed hollow cathode technique [54], as far as I am aware, only conventional magnetrons are used nowadays in nanocluster sources.

In recent years, there has been increasing interest in studying the size distribution of cluster beams produced by magnetron sputtering, using either quadrupole [55–59] or time-of-flight mass-spectrometry [43, 60]. The investigation of clusters deposited on the substrate with or without mass selection [16, 17, 61–64] has also gained importance. For an accurate study it is necessary to consider the effects that may dramatically influence the properties of the cluster beam, but that cannot be easily controlled. One of the aims of this thesis is to investigate these effects.

The subject of the present thesis is an experimental and theoretical study of the properties of the cluster beam produced by a conventional DC magnetron-based gas aggregation source. This study is important for the understanding of the fundamental processes underlying cluster formation, cluster flow and cluster charging, which is in turn needed for practical applications to tune the characteristics of the produced cluster beam. In the present work, the effect of the magnetron target lifetime on the cluster size distribution was systematically investigated and quantitatively characterized. To my knowledge, this has so far not been investigated by previous researchers. With the findings of this study, a stable beam of clusters of the desired size can be produced. The method developed here for the measurement of the velocity distribution functions of nano-size cluster ions allows to determine the cluster-surface interaction mode during the deposition. It also gives additional information about cluster and buffer gas flow

regime, cluster charges, and the parameters of cluster containing secondary plasma in the aggregation region.

This is a cumulative dissertation. The second chapter describes the theoretical background of cluster formation, charging, and flow processes which is needed for analysis and understanding of the experimental results. The equipment and methods used during this study are presented in the third chapter. The experimental results are included as research papers that have been submitted to, or published in peer-review journals. The last chapter summarizes the main achievements of the present work. The appendices contain the information collected during this work, which may be useful for further research or for other Ph.D. students.

Chapter 2

Theoretical background

2.1. Formation and growth of clusters in a buffer gas

Cluster formation can be divided into two steps: nucleation and growth. *Nucleation* is the process by which clusters of a stable phase form in a metastable phase [65, 66]. A metastable state for a gas aggregation source is a supersaturated vapor of sputtered metal particles. A comprehensive review of the various nucleation theories and their comparison can be found in [65–67]. The nucleation process starts from the fluctuation, which leads to the formation of a small quantity (cluster) of a new phase called *nucleus* [31, 66, 68–70]. In terms of supersaturated vapor of metal particles (M) in the buffer gas (Ar), this process can be described as a three-body collision

$$\mathrm{M} + \mathrm{M} + \mathrm{Ar} \rightarrow \mathrm{M}_2 + \mathrm{Ar} \tag{2.1}$$

where the third partner (Ar) is needed to take the excess of energy resulting from the bond formation, and to stabilize the nascent dimer [31]. The rate constants of the process (2.1) K for copper and silver are given in table 3.1. According to phase transitions theory [68, 70], only those nuclei with a size above a certain value are stable and can serve for further cluster growth. This value is called the *critical size* [68] and depends on the experimental conditions (pressure, temperature, supersaturation, etc.). Theoretical approach [69, 71–73] considers a dimer as a stable nucleus for cluster growth.

Further cluster growth is governed by four main processes shown in Fig. 2.1: atom attachment, coagulation (kinetic and diffusion modes), coalescence (Oswald ripening) and aggregation [69, 74]. *Attachment of atoms* (Fig. 2.1a) is a process of cluster growth, when the metal atoms are attached to the cluster M_n consisting of n atoms

$$\mathrm{M}_n + \mathrm{M} \rightarrow \mathrm{M}_{n+1} \tag{2.2}$$

It is assumed that subsequent collisions of a growing cluster with gas atoms will lead to transfer of the energy resulting from the bond formation to the gas. The rate constant k_n for the process (2.2) depends on the cluster size [69, 71, 72]

$$k_n = k_0 n^{2/3} \tag{2.3}$$

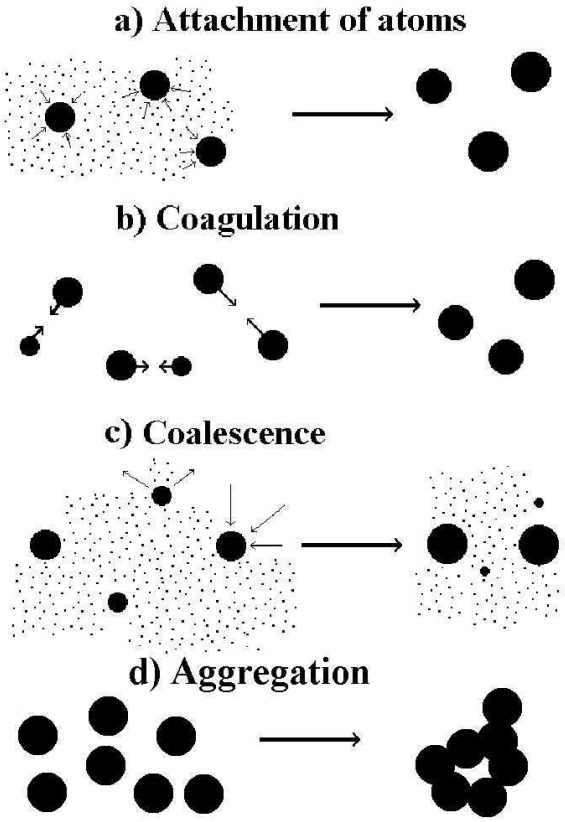

Figure 2.1.: Mechanisms of cluster growth. Reprinted from [74].

where k_0 is a reduced rate constant depending on the materials and experimental conditions, and n is the number of cluster atoms. Values of k_0 for copper and silver are given in table 3.1. Rate constants for the cluster growth process (2.2) are much higher than for a dimer formation process (2.1). This results in a large average cluster size. The character of the process (2.2) is determined by the value of the dimensionless parameter G [71]

$$G = \frac{k_0}{KN_{Ar}} \tag{2.4}$$

where N_{Ar} is the density of the buffer gas (argon). For the considered experimental conditions and materials in the present work, $G \gg 1$. The theoretical approach [71], which is based on the solution of balance equation, provides the following expressions for the average cluster size $\overline{n}$, density of clusters N_{cl}, and cluster size distribution function f_n

$$\overline{n} = 0.31G^{3/4} \tag{2.5}$$

$$N_{cl} = 3.2NG^{-3/4} \tag{2.6}$$

$$f_n = \frac{C}{n^{2/3}} \tag{2.7}$$

where N is the density of free metal atoms, and C is a normalization constant.

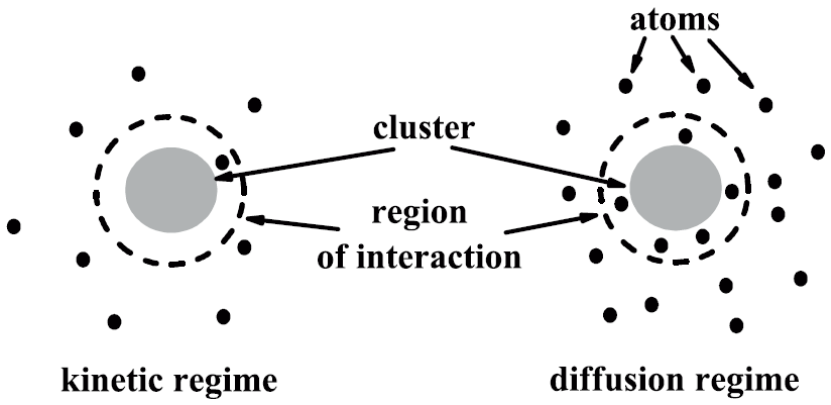

Figure 2.2.: Kinetic and diffusion regime of cluster interaction with atoms of a surrounding gas. Reprinted from [74].

The second mechanism of cluster growth is coagulation (Fig. 2.1b). *Coagulation* is defined as the formation of a single liquid drop resulting from contact of two liquid drops [69, 74].

$$\mathrm{M}_{n-m} + \mathrm{M}_m \rightarrow \mathrm{M}_n \tag{2.8}$$

where n and m are the number of atoms in the cluster. Taking into account both the motion of an individual cluster in a buffer gas and the relative motion of two clusters, two coagulation regimes can be distinguished: kinetic and diffusion. The difference between these two regimes is illustrated in Fig. 2.2: in the kinetic regime only one particle at a time strongly interacts with the cluster under consideration, whereas in the diffusion regime many particles strongly interact with the cluster simultaneously [74]. For the coagulation of liquid copper clusters in argon, the criterion for the diffusion regime has the form [74]

$$N_{\mathrm{Ar}}\overline{n}^{3/4} \gg \sqrt{c_b} \times 3 \times 10^{23} cm^{-3} \tag{2.9}$$

where $c_b = N_b/N_{\mathrm{Ar}}$ is a concentration of bound atoms in clusters, and N_b is a density of atoms bound in clusters. For the typical experimental conditions in the present work, $N_{\mathrm{Ar}} \approx 4 \times 10^{15}$ cm^{-3} and $\overline{n} \sim 10^4$ atoms. Hence, $N_{\mathrm{Ar}}\overline{n}^{3/4} \approx 4 \times 10^{18}$. Thus, to fulfill the criterion (2.9) for the diffusion regime, c_b must be below 10^{-10}. A theoretical estimation for cluster generation in a magnetron plasma [71] provides $c_b \sim 0.5$. This suggests that, as a rule, in our nanocluster source we have a kinetic regime of cluster coagulation. The theoretical approach based on the solution of the Smolukhovski equation for the kinetic regime of cluster coagulation [74] provides the following expressions for the cluster size distribution function f_n and average cluster size $\overline{n}$

$$\overline{n} = 6.3\,(N_b k_0 t)^{1.2} \tag{2.10}$$

$$f_n = \frac{N_b}{\overline{n}^2} \exp\left(-\frac{n}{\overline{n}}\right) \tag{2.11}$$

where t is time.

Coalescence (or Oswald ripening, Fig. 2.1c) is a process of growth of large clusters while the small clusters evaporate [69]. This process takes place when the supersaturation degree becomes very slight [75]. The main parameter of the coalescence process is the critical cluster size n_{cr}, or critical cluster radius r_{cr}, with which the cluster is in equilibrium with the medium. Critical cluster size separates clusters into two groups: smaller clusters with size $n < n_{cr}$ will evaporate, but larger clusters with size $n > n_{cr}$ will grow due to the atom attachment [68, 74–76]. For the degree of supersaturation Δ, the critical radius is defined as [75]

$$r_{cr} = \frac{\alpha}{\Delta} \tag{2.12}$$

where α is a parameter containing the inter-phase tension σ_t, the atomic volume of the solute V_{M}, the concentration of the saturated solution C_∞ and the temperature T [75]

$$\alpha = \frac{2\sigma_t}{kT} V_{\mathrm{M}} C_\infty \tag{2.13}$$

As a solution we consider a vapor of metal atoms in a buffer gas, and as a solute metal, i.e. copper or silver, atoms. In the framework of the liquid drop model [77], the connection between n_{cr} and r_{cr} is expressed as [74]

$$r_{cr} = r_W n_{cr}^{1/3} \tag{2.14}$$

where r_W is the Wigner-Seitz radius. Values of r_W for silver and copper are given in table 3.1.

The theoretical approach [74] distinguishes between diffusion and kinetic coalescence regimes. For the diffusion regime, the average cluster size $\overline{n}$ and cluster size distribution function f_n are expressed as [74]

$$\overline{n} = 1.135 n_{cr} \tag{2.15}$$

$$f_n = \frac{n_{cr}}{\overline{n}} \frac{N_b}{3u^2} P_{dif}(u) \tag{2.16}$$

where $u = r_c/r_{cr}$ is a reduced cluster size, r_c is a cluster radius, and the distribution function $P_{dif}(u)$ is defined as [74]

$$P_{dif}(u) = \begin{cases} 64.9 \dfrac{u^2 \exp\left[-1(1-2u/3)\right]}{(u+3)^{7/3}(3/2-u)^{11/3}} & \text{if } u < 3/2, \\ 0 & \text{if } u > 3/2. \end{cases} \tag{2.17}$$

The average cluster size $\overline{n}$ growth in time as

$$\overline{n} = 1.4 \frac{A}{T} D_m r_W N t \tag{2.18}$$

where A is a specific surface energy of the cluster and D_m is the diffusion coefficient of the metal atoms in a buffer gas. For the kinetic coalescence regime the following

dependencies are given [74]

$$\overline{n} = 1.123 n_{cr} \tag{2.19}$$

$$P_{kin}(u) = \begin{cases} 232 \exp(-1.18u) \dfrac{u^3 \exp[-1/(1-2u/3)]}{(u+3)^{7/3}(3/2-u)^{11/3}} & \text{if } u < 3/2, \\ 0 & \text{if } u > 3/2. \end{cases} \tag{2.20}$$

where the average cluster size $\overline{n}$ growth in time as [74]

$$\overline{n} = 0.014 \left(\frac{A}{T} k_0 N t \right)^{3/2} \tag{2.21}$$

Analysis of the cluster growth in the inert-gas evaporation source in the framework of statistical theory of coalescence [78] results in a log-normal distribution function

$$f_n = \frac{1}{\sqrt{2\pi} \log \sigma} \exp \left(- \frac{\log d_c - \log \overline{d_c}}{\sqrt{2} \log \sigma} \right)^2 \tag{2.22}$$

where d_c is a cluster diameter, $d_c = 2 r_W (n)^{1/3}$.

Finally, *aggregation* (Fig. 2.1d) is a process where solid clusters are joined due to their contact, while partially preserving their initial shape [74]. This process can result in the growth of fractal aggregates or the joining of small fractal aggregates into a larger one [69]. Fractal properties are described by the fractal dimensionality. Performed during the present work investigation of the morphology of copper and silver clusters deposited on the substrate [45, 63, 64] has not revealed any fractal aggregates formed in the cluster beam. This suggests that this process either does not take place, or it is negligible in the nanocluster sources under consideration.

Alongside the general concepts of cluster growth and the above analytical models, some studies have attempted a computer simulation of cluster growth processes. Typically Monte Carlo (MC) [79], kinetic Monte Carlo (kMC) [80], molecular dynamics (MD) [81], or a combination of the above [82] are used. The experimental conditions of [79] are the closest to the present work. This is a Monte Carlo simulation of growth of Cu clusters in Ar buffer gas in a cylindrical gas aggregation source. The following processes are considered:

1. elastic collisions between atoms
2. metastable dimer formation: $\mathrm{Cu} + \mathrm{Cu} \rightarrow \mathrm{Cu}_2^*$; the excited dimer can be stabilized by collision with a Cu or Ar atom within its lifetime
3. coagulation
4. inelastic Ar-Cu_n collisions; this constitutes the main mechanism of collisional cooling of Cu clusters
5. cluster decay: $\mathrm{Cu}_n \rightarrow \mathrm{Cu}_{n-1} + \mathrm{Cu}$

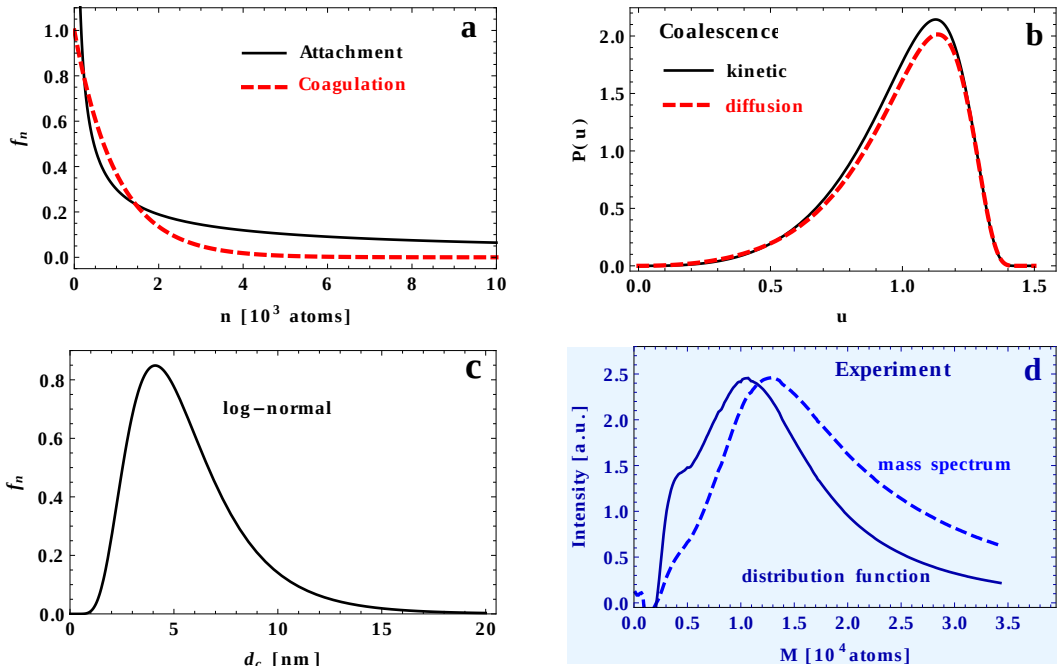

Figure 2.3.: Summary of the shape of cluster size distribution functions f_n for different cluster formation processes. **a:** atom attachment (black solid line) and coagulation (red dashed line), **b:** coalescence, kinetic (black solid line) and diffusion (red dashed line) regimes, **c:** log-normal distribution obtained from statistical theory of coalescence [78], **d:** experimental results of the present work, i.e. typical mass spectra (blue dashed line) and the cluster size distribution function evaluated from it (navy solid line). The experimental results (**d**) are highlighted with a blue background.

This simulation [79] results in a cluster size distribution which is close to log-normal (2.22), that is in a good agreement with the theoretical approach of [78].

Figure 2.3 summarizes the shape of the cluster size distribution functions for the cluster growth processes under consideration. As can be seen, these processes result in quite different distribution functions (Fig. 2.3a–c), none of which is completely the same, as typically observed in the experiment (Fig. 2.3d). This suggests that there are several processes going on simultaneously in the gas aggregation source, and which process is dominant will depend on the experimental conditions. Moreover, the experimental cluster size distribution is a result of the contribution of both cluster formation and cluster flow processes. Even if the cluster formation process results in a monotonically decreasing function, the mass spectrum with a maximum as shown in Fig. 2.3d may be observed. This effect can be explained by the loss of small clusters in the aggregation chamber due to attachment to the walls. The average displacement of clusters in the aggregation chamber $\overline{x} = \sqrt{4D_n\tau_r}$, where D_n is the diffusion coefficient of clusters in a buffer gas and τ_r is the residence time of clusters in the aggregation chamber, may be comparable to the chamber radius. For example, for the typical experimental conditions

$p = 18.7$ Pa, $T = 300$ K in the present study, the diffusion coefficient for clusters of size $n = 1.5 \times 10^4$ atoms in argon is $D_n = 6.3$ cm^2/s. Assuming the residence time of clusters in the aggregation chamber $\tau_r = 1$ s, we obtain $\overline{x} \approx 5$ cm, which corresponds to the chamber radius. Since the diffusion coefficient D_n decreases with cluster size [74], the displacement $\overline{x}$ will be smaller for larger clusters [83]. Thus, for a proper comparison of experimental and theoretical cluster size distribution, an understanding of the cluster and buffer gas flow character is required.

2.2. Cluster flow with a buffer gas

Analysis of the cluster flow character is a complicated problem which involves both gas flow and cluster motion processes. Three regions with different flow character can be distinguished: aggregation chamber, transition through the orifice, and beam propagation after the orifice. Since the rarefied gas flow through a thin slit or an orifice is of great practical interest [84], much effort is given to study it experimentally [85–87], by a numerical direct Monte Carlo simulation [84, 88–94], or analytically [69, 71, 72, 74, 95]. As the analytical approach also takes into account the cluster motion in a buffer gas, it is reasonable to use this approach for the cluster flow analysis in the present work.

The regime of flow propagation under the typical experimental conditions in the present work, $p = 18.7$ Pa, $T = 300$ K corresponds to the number density of argon atoms $N_{\mathrm{Ar}} = 4.5 \times 10^{21}$ m^{-3} and the mean free path of argon atoms in argon $\lambda = 1/(N_{\mathrm{Ar}}\sigma_g) = 0.6$ mm, where $\sigma_g = 3.7 \times 10^{-19}$ m^2 is the gas-kinetic cross-section for collision of two argon atoms at room temperature. As can be seen, the mean free path of argon atoms significantly exceeds a typical cluster radius (2.5–5 nm) that corresponds to a kinetic regime of atom-cluster interaction [74]. According to [94], the small ratio of the mean free path to the orifice radius $\lambda/R = 0.4$ for the typical $R = 1.5$ mm allows to apply an analytical model [72] based on the kinetic Boltzmann equation for determining the cluster drift velocity. The analytical model [72] was developed taking into account the experimental results of Shyjumon [96] obtained on the nanocluster source NC-200, which is also used in the present work. Therefore, it is reasonable to use the model [72] for comparison with the experimental results of the present work. According to [72], there is an equilibrium inside the aggregation chamber of the nanocluster source between the drift velocities of buffer gas (Ar) atoms and clusters. Thus, they move with the thermal velocity $\sqrt{(8kT)/(\pi m)}$. However, Ar atoms become accelerated near the output orifice. There is insufficient time to reach equilibrium again, and hence, the clusters become significantly slower than the Ar atoms. Solution of the kinetic Boltzmann equation for clusters in a gas flow [72] provides the expression for the cluster drift velocity at an orifice. Making all the necessary substitutions yields the following expression for the drift velocity w of copper clusters in argon

$$w = \frac{3.77\, R^{2/3}\, r_W^{4/3}}{m_{\mathrm{Cu}}^{4/9}\, G_o^{2/3}} \left(\frac{m_{\mathrm{Ar}}}{kT}\right)^{1/3} \frac{u_{\mathrm{Ar}}^{1/3}\, p^{2/3}}{M^{2/9}} \tag{2.23}$$

where R is the orifice radius, r_W is the Wigner-Seitz radius, m_{Cu} and m_{Ar} are the mass

of Cu and Ar atoms, respectively, k is the Boltzmann constant, and T and p are gas temperature and pressure in the aggregation chamber, respectively. G_o is a geometrical factor related to the orifice and nozzle shapes and contributes to the typical time for the variation of the flow velocity. For the case considered in the model [72] with a conic orifice with an angle φ between cone walls and the tube axis $G_o = \tan\varphi$. The argon flow velocity u_{Ar} can be evaluated as [71]

$$u_{\mathrm{Ar}} = \frac{Q}{\pi R^2 N_{\mathrm{Ar}}}, \tag{2.24}$$

where Q is the gas flow rate, and N_{Ar} the density of argon atoms in the aggregation chamber. Thus, although the analytical approach [72] provides the cluster drift velocity at the orifice, it does not consider further cluster motion.

Analysis of the cluster motion after transition through the orifice [83] shows that if the distance is long enough, clusters can become significantly accelerated due to collision with argon atoms in the beam and cluster-cluster interaction. An equilibrium drift velocity of clusters is established after $\sim M/m_{Ar}$ collisions with buffer gas atoms [71]. For clusters of size 5–10 nm the value of $M/m_{Ar} \approx (0.8\text{–}5) \times 10^4$. For a single cluster the number of collisions with the buffer gas atoms per second is

$$\nu = N_{\mathrm{beam}} \langle u_{\mathrm{Ar}} - v_p \rangle \, \sigma_c, \tag{2.25}$$

where $\langle u_{\mathrm{Ar}} - v_p \rangle$ is the average relative velocity of clusters in argon, N_{beam} is the argon density in the beam after the orifice, and $\sigma_c = \pi r_c^2$ is the cluster cross-section. In the present work, pressure in the aggregation chamber was varied in the range of 18–80 Pa for different argon flows that corresponds to an argon density in the beam [74] $N_{\mathrm{beam}} = 0.77 N_{\mathrm{Ar}} = (3.4\text{–}14) \times 10^{21}$ m^{-3} at the temperature of 300 K. The measured cluster velocity values v_p are in the range of 80–180 m/s [83]. For $r_c = 3.5$ nm, the approximate time of flight τ of the cluster over the 30 cm distance from the orifice to the QMF detection plates is in the range of 1.5–3 ms. Hence, $\nu\tau \sim (4\text{–}8) \times 10^4$. So, the cluster on its path after the orifice has about $(4\text{–}8) \times 10^4$ collisions with neutral gas atoms. Such a number of collisions is comparable to M/m_{Ar} and may significantly accelerate the cluster.

2.3. Cluster charging processes

The experimental cluster size distribution depends on both the ratio between positive and negative clusters, and the cluster charge. There is a tacit assumption that nano-size clusters produced by a gas aggregation source are either singly charged or neutral [1, 15, 41–43], while usually dust particles in a plasma are multiply charged [97–101]. For example, theoretical analysis of cluster charging processes in low-pressure plasmas [97] with T_e in the range of a few eV suggests the charge value Z_p to be below 10 for particles with a diameter $d_c \lesssim 10$ nm.

The theoretical approach [74] suggests that small clusters in the rarefied gas are neutral or singly charged in the kinetic regime of cluster charging if the potential energy of a

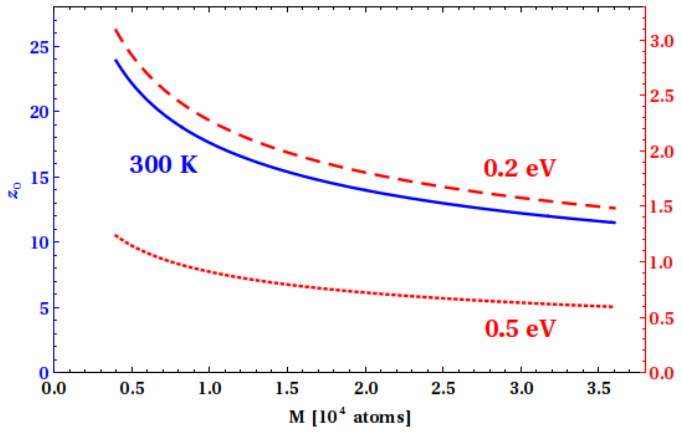

Figure 2.4.: Factor z_0 defined by equation (2.27) for different temperatures T: $T = 300$ K (blue solid line), $T = 0.2$ eV (red dashed line), and $T = 0.5$ eV (red dotted line).

singly charged particle

$$\frac{1}{4\pi\varepsilon_0}\frac{e^2}{r_c} \tag{2.26}$$

significantly exceeds the thermal energy of an electron or ion kT where $T = T_e$ or T_i for electron or ion, respectively. The criterion for the kinetic regime [74] $r_c \ll \lambda$ is fulfilled under the experimental conditions in the present work: estimations [83] provide a mean free path $\lambda \approx 0.6$ mm, that is 5–6 orders larger than the typical cluster radius. Thus, for a single charge of clusters the ratio between cluster potential energy and thermal energy of electron or ion should be

$$z_0 = \frac{1}{4\pi\varepsilon_0}\frac{e^2}{r_c}\frac{1}{kT} \gg 1 \tag{2.27}$$

where e is the elementary charge, r_c cluster radius, and k the Boltzmann constant. Figure 2.4 shows the value of z_0 for different temperatures T: $T = 300$ K (blue solid line), $T = 0.2$ eV (red dashed line), and $T = 0.5$ eV (red dotted line) for the cluster sizes considered in the present work. As one can see, to fulfill the criterion (2.27) T_e and T_i should be below 0.5 eV. Since ions in the secondary plasma are thermalized due to collisions with the buffer gas, it is reasonable to suggest that T_i is equal to the gas temperature, i.e. $T_i = 300$ K. Thus, for ions the criterion (2.27) is fulfilled.

Table 2.1 summarizes the experimental data on measurements of the electron temperature in the magnetron discharge performed by various researchers. For those investigations where two-temperature electron distribution functions were measured, either the cold electrons, or the effective temperature is considered, depending on which of them is given in the reference. With the exception of the near-cathode region, the amount of hot electrons is significantly lower than the amount of cold electrons. Thus, the temperature of the hot electrons does not noticeably influence the electron mobility in the

T_e [eV]	Pressure [Pa]	I_d [A]	Z [mm]	Target	Reference
0.2	18.7	0.4	50–120	Cu	[83]
0.5	11	0.32	20–50	Cu	[102]*
0.6–1.2	2	0.22–0.25	20–120	Cu	[103]
1	4	0.1	35	Cu	[104]
5	4	0.1	5	Cu	[104]
5	0.6	0.1	35	Cu	[104]
2	2	0.2	5-10	Cu	[105]
3	0.96	0.15	10.3	Cu	[106]
0.2–0.8	5.3	0.86	100	Ag	[107]
0.3–2.5	5.3	0.86	50	Ag	[107]
0.2–2	0.6	0.86	100	Ag	[107]
0.3–0.7	5.3	0.6	30–100	Ag	[108]
0.2–0.4	0.4, 5	0.75	15–80	Ti	[109]
0.97	0.4	?	80	Ti	[110]
2	0.7	0.3	88	Ti	[111]
2.2	0.8	0.15	40	C	[112]
3	0.8	0.10	40	C	[112]
5	0.8	0.05	40	C	[112]
4.85	1.07	0.1	70	Si	[113]
7	0.4	RF	120	h-BN	[114]

Table 2.1.: Overview of experimental measurements of the electron temperature T_e in the magnetron discharge. I_d is a discharge current, Z is a distance from the cathode surface, Target is a cathode material. Argon was used as a working gas for all references except [102]. *The results from [102] are measured for He, but it is claimed [102] that a similar results have been observed for Ar. The first row indicates T_e evaluated in the present work by the analysis of cluster IVDFs.

aggregation region and hence, in the framework of the theoretical model [71, 95], does not affect the cluster charge. The first row of table 2.1 shows the typical experimental conditions of the present work. None of the T_e values presented in table 2.1 were measured at experimental conditions similar to the present work. As can be seen in table 2.1, in the present work there are the highest pressure, discharge current, and distance from the cathode. The closest are the experimental conditions of [102] (second row, $T_e = 0.5$ eV). The measurements [102] were performed for He as a buffer gas, but it is claimed, that a similar results for an Ar were observed. An analysis of further rows of table 2.1 and the corresponding references show that T_e decreases with distance from the target [103, 104, 107, 109, 110, 112], with pressure in the magnetron chamber [103–105, 109, 112, 113], and with discharge current increase [112]. Since in the present work the pressure, discharge current, and distance from the target are higher than in [102], it can be concluded that the T_e for the considered experimental conditions should be

below 0.5 eV. Thus, the electron temperature also fulfills the criterion (2.27) and the clusters produced in the present work appear to be singly charged or neutral.

In high pressure gas aggregation sources [15, 45, 115] clusters may form in the regions near the magnetron cathode, where the electron temperature is essentially higher than in the secondary plasma. According to criterion (2.27) these cluster ions should be multiply charged. However, experiment [115] confirms the above suggestion about the single charge of nanoparticles with a diameter below 30 nm. It is explained in [115] by the loss of charge of multiply charged cluster ions due to recombination in the aggregation region.

The theoretical approach [71, 72, 74, 95] considers the following processes of charging and neutralization for singly charged clusters

$$e + \mathrm{M}_n \rightarrow \mathrm{M}_n^- \tag{2.28}$$

$$e + \mathrm{M}_n^+ \rightarrow \mathrm{M}_n \tag{2.29}$$

$$\mathrm{A}^+ + \mathrm{M}_n \rightarrow \mathrm{M}_n^+ + \mathrm{A} \tag{2.30}$$

$$\mathrm{A}^+ + \mathrm{M}_n^- \rightarrow \mathrm{M}_n + \mathrm{A} \tag{2.31}$$

Solution of the set of corresponding balance equations results in the following expressions for the ratio between densities of positive N_+, negative N_-, and neutral N_0 clusters [71, 72, 74, 95]

$$\frac{N_-}{N_0} = \sqrt{\frac{T_e m_i}{T_i m_e}} \frac{N_e}{N_i} \frac{1}{1 + z_0(T_i)} \tag{2.32}$$

$$\frac{N_+}{N_0} = \sqrt{\frac{T_i m_e}{T_e m_i}} \frac{N_i}{N_e} \frac{1}{1 + z_0(T_e)} \tag{2.33}$$

where m_e and m_i are the electron and ion mass respectively, N_e and N_i are the electron and ion density, respectively, and z_0 is defined by equation (2.27). This allows derivation of the following relation for N_+/N_- ratio

$$\frac{N_+}{N_-} = \frac{m_e}{m_i} \left(\frac{N_i}{N_e}\right)^2 \frac{kT_i + \dfrac{e^2}{4\pi\varepsilon_0}\dfrac{1}{r_c}}{kT_e + \dfrac{e^2}{4\pi\varepsilon_0}\dfrac{1}{r_c}} \tag{2.34}$$

The expression (2.34) will be further used [83] for comparison of the experimental results of the present work with the theoretical model.

Chapter 3

Materials and Methods

3.1. Materials

Copper and silver were used as materials for the cluster production. Ar with or without admixture of He was used as a buffer gas. The table below summarizes the most important properties of the materials used in the present work.

	Cu	Ag	Reference
z_a	29	47	
m_a [amu]	63.546(3)	107.8682(2)	[116]
ρ [g/cm^3]	8.95	10.47	[116]
T_m [K]	1358	1235	[74]
E_{ion} [eV]	7.7264	7.5762	[116]
r_W [nm]	0.147	0.166	[71]
ϵ_0 [eV]	3.40	2.87	[71]
Y [atoms/ion] at 300 eV, normal incidence			
Ar→target	1.05	1.28	[117]
He→target	0.160	0.120	[117]
Cluster formation			
K [10^{-33} cm^{6}s^{-1}]	3.0	5.5	[71]
k_0 [10^{-11} cm^{3}s^{-1}]	4.2	3.8	[69]

Table 3.1.: Common properties of Cu and Ag influencing cluster formation.

3.2. Magnetron Sputtering

Sputtering is the removal of target surface atoms due to energetic particle bombardment [118]. In this process, target atoms are removed from the surface by collisions between a projectile and/or produces recoil atoms and the atoms in the near-surface

layers of the target material [119]. *Sputtering yield*, i.e. the number of atoms ejected from a target surface per incident ion, is the most fundamental parameter of sputtering processes [120]. The two most abundant ways to assess sputtering yield are the TRIM software [121, 122], based on a Monte Carlo simulation of the sputtering process, and the semi-empirical Yamamura approach [123–125]. A detailed description of the estimation of sputtering yield for copper target using the Yamamura approach is provided in appendix A. In Fig. 3.1 energy (left) and angular (right) dependence of sputtering yield Y calculated using the Yamamura approach (solid line, equations (A.1) and (A.11)) are compared with TRIM simulations [117] (•) and with experimental data of [126] (▲) and [127] (▼). Comparison with experimental data is provided only for a normal incidence. All sources produce a similar results, but the angular dependence for TRIM calculations [117] is less pronounced.

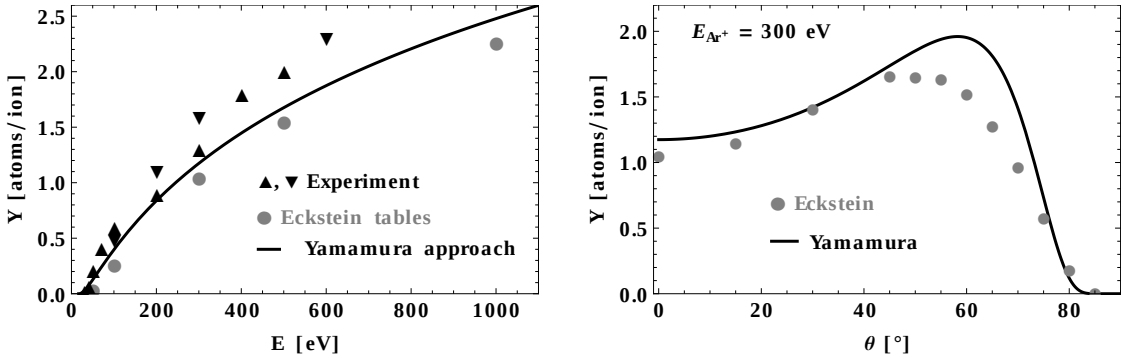

Figure 3.1.: Calculated dependence of the sputtering yield Y for Cu target on the energy E of incident Ar^+ ions for normal incidence (left, solid line), using the equation (A.1). Calculated angular dependence of sputtering yield for energy of incident Ar ions $E = 300$ eV (right, solid line), using the equation (A.11). TRIM calculations [117] (•). Experimental data: [126] (▲) and [127] (▼).

Magnetrons are defined as diode sputtering sources in which magnetic fields are used in concert with the cathode surface to form electron traps which are configured in such a way that the $\mathbf{E} \times \mathbf{B}$ electron currents close on themselves [39]. In comparison with non-magnetron sputtering, magnetron sputtering allows us to achieve a significantly higher performance. High discharge currents can be obtained almost independently of the voltage even at low pressures. This characterizes the *magnetron mode* of operation [39]. The increased ionization efficiency achieved in the magnetron mode allows maintaining the discharge at lower operating pressures and lower operating voltages than is possible in the basic sputtering mode [128].

The schematics of a typical planar magnetron with a circular target is displayed in the center of Fig. 3.2. The magnetron consists of a grounded anode, and a target acting as a cathode biased with negative voltage. The magnet assembly contains a ring-like and a cylindric magnets. The resulting magnetic field configuration is shown as red dashed lines in Fig. 3.2. The electric field direction is indicated with the blue arrow. Such configuration accelerates the buffer gas ions towards the cathode, which causes

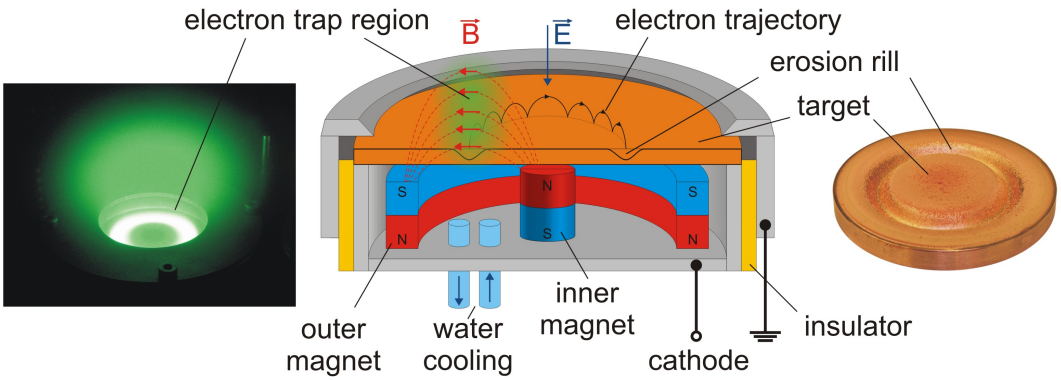

Figure 3.2.: Schematics of a typical planar magnetron with a circular target (center). Copper target (right). Photo of the magnetron discharge with Ar as the buffer gas and Cu as the target material (left). Thanks to Steffen Drache for this picture.

sputtering of the target atoms by an energetic ion impact. Secondary electrons are also emitted from the target surface as a result of the ion bombardment. These electrons play an important role in maintaining the plasma [128]. The magnetic field configuration confines the electrons in the region marked with the red arrows in Fig. 3.2. Electrons circulate around the magnetic field lines, and therefore travel for a much longer time in the plasma than in non-magnetized plasmas [129]. This causes an effective ionization of the buffer gas atoms in the electron trap region and a high sputtering rate in this region. This results in a non-uniform target erosion, i.e. the formation of a deep and narrow erosion groove. The typical erosion rill is shown on the photo of the copper target in Fig. 3.2(right).

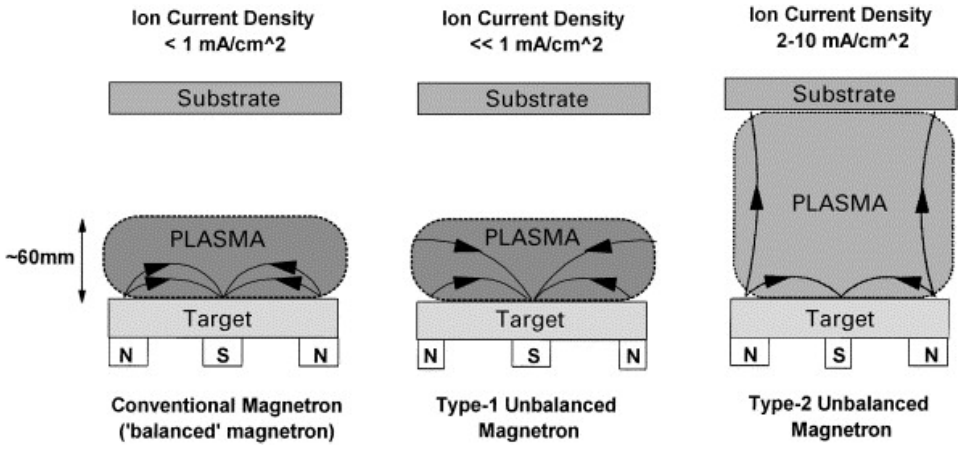

Figure 3.3.: Plasma confinement in different magnetron modes. Reprinted from [128].

In the late 1980s unbalanced magnetrons were developed. In an unbalanced magnetron the outer ring of the magnets is strengthened relative to the central pole. Thus, not all

field lines are closed between the central and the outer magnets. This means that the plasma is no longer confined to the target region, but is also allowed to flow towards the substrate [128]. Fig. 3.3 [128] shows the plasma confinement in different magnetron modes. On the left-hand side, the balanced magnetron (closed magnetic field lines) similar to one used in the present work is shown. In the center and right the two types of unbalanced magnetrons are displayed. In type-2 magnetrons, some magnetic field lines are directed towards the substrate.

The type of magnetron mode influences not only the plasma confinement, but also the target profile, deposition rate and plasma parameters (see, for example [111]). As far as I am aware, unbalanced magnetrons and their assemblies are commonly used for deposition of atomic films, but in the nanocluster sources only conventional balanced magnetrons are applied. In the present work, a conventional balanced planar magnetron with a circular target of 2"diameter and of 5 mm thickness was used.

3.3. Production of nanocluster beam

3.3.1. Nanocluster source NC-200 (Greifswald)

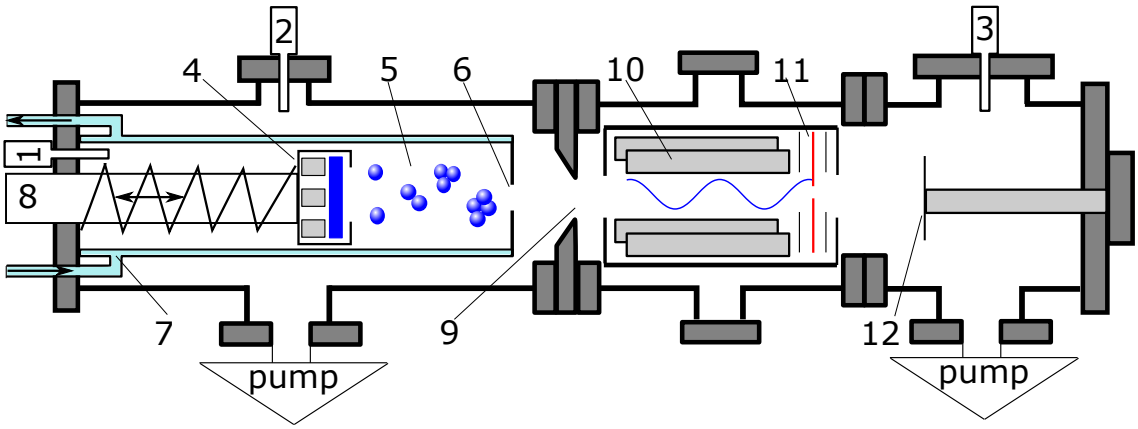

Figure 3.4.: Schematics of the nanocluster source. 1,2,3 — Pressure gauges. Magnetron section: 4 — magnetron, 5 — aggregation region, 6 — variable output orifice, 7 — inlets for cooling of the aggregation chamber walls, 8 — interfaces for connection of Ar, water cooling of the magnetron magnets and power supply; screws for setting the variable orifice diameter and length of the aggregation region, 9 — orifice. Quadrupole Mass Filter (QMF): 10 — quadrupole rods, 11 — detection plate. Deposition chamber: 12 — substrate holder. Reprinted from [44].

The nanocluster source NC-200, produced by Oxford Applied Research, is a commercially available gas aggregation source based on magnetron sputtering. It contains three sections: the magnetron and aggregation chamber, the quadrupole mass filter (QMF), and the deposition chamber. Three pressure gauges are installed at positions marked 1,

2 and 3 in Fig. 3.4: gauge 1 is attached to the magnetron chamber, gauge 2 — to the outer magnetron chamber and gauge 3 — to the deposition chamber. Pressure in the magnetron chamber was measured using the pressure sensor Balzers TPR 018. Since the pirani pressure gauges are gas-dependent, the correction coefficient 1.7 (for Argon) was applied for the pressure evaluation. The magnetron (4) is used as a source of free metal atoms needed for cluster formation. It is equipped with a circular Cu target of 2" diameter and of 5 mm thickness. Sputtered atoms proceed together with a buffer gas flow through the aggregation chamber (5), towards the output orifice (6). The aggregation chamber (5) is a cylinder with a radius of 5 cm and a variable aggregation length (ATL) in the range of 5–22 cm. The walls of the aggregation chamber can be cooled by water or liquid nitrogen. The length of the aggregation chamber can be controlled using the vacuum spring (double-sided arrow). The road (8) has interface connections for mass flow controllers, i.e. MKS 247 4 Channel Readout and type 1179A mass flow controller, water cooling of the magnetron magnets and electrical power supply (Glassman LV 600-1.7). The cluster beam enters the mass filter through the orifice (9). To measure the cluster size distributions, a commercially available quadrupole mass filter QMF200 (Oxford Applied Research) was used. After passing through the quadrupole mass filter, the mass selected clusters proceed to the deposition chamber where they can be deposited on the substrate fixed on the holder (12). The range of experimental conditions and their typical values are listed in table 3.3.2.

3.3.2. High pressure nanocluster source (Kiel)

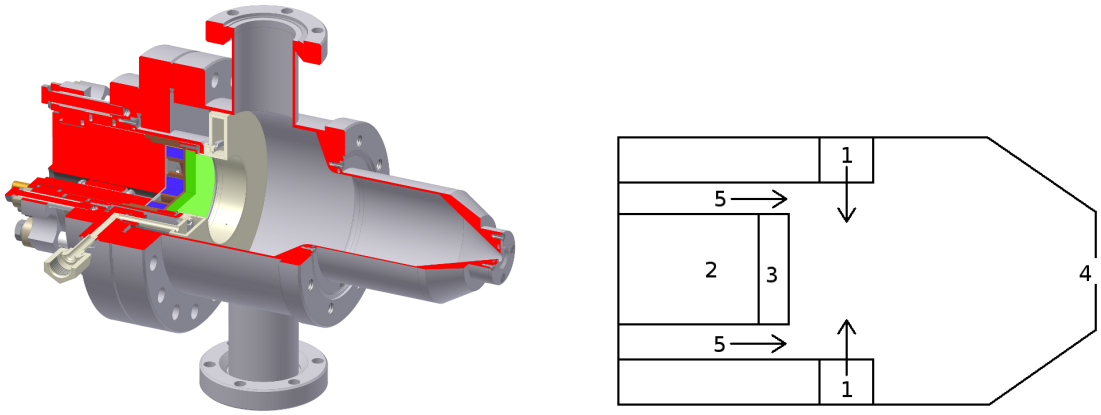

Figure 3.5.: Left: 3D picture of the cluster source, reprinted from [130]. Right: schematics of the cluster source as a sectional drawing: 1 — He gas inlet ring, 2 —Magnetron cathode with water cooling, 3 —Ag target mounted on the magnetron cathode, 4 —Orifice, 5 —Gas line for Ar. Reprinted from [45]. Thanks to Tilo Peter for these pictures.

Fig. 3.5 shows the schematics (right) and 3D drawing (left) of the home built high pressure nanocluster source (Kiel), developed for the production of nanocomposite films.

NC-200 (Greifswald)			High pressure source (Kiel)	
Parameter	**Range**	**Typical**	**Range**	**Typical**
Q_{Ar} [sccm]	5–100	15	20–110	113
Q_{He} [sccm]	0–50	0	30–100	0
P_1 [Pa]	5–80	18.7	20–200	200
P_2 [Pa]	0.3–1	0.4	0.1–1	0.3
P_3 [Pa]	0.02–0.2	0.03	—	—
T [K]	100–300	300	—	300
ATL [cm]	5–22	12	10–18	8.5+9.8
d_i [mm]	1–10	3	2–5	3
d_o [mm]	1–10	8	—	—
I_d [A]	0.1–1.6	0.4	0.2–0.6	0.2
U_d [V]	200–400	300	180–400	260
Chamber radius [cm]	—	5	—	5.2 and 3

Table 3.2.: Range of experimental parameters and their typical values. Q_{Ar} and Q_{He} are the Ar and He gas flow rate respectively. P_1 is the pressure in the magnetron chamber. P_2 and P_3 are the pressures in the outer magnetron chamber and the deposition chamber respectively (pressure gauges 2 and 3 in Fig. 3.4). T is the temperature of the aggregation chamber walls. ATL is the aggregation tube length. d_i is the inner orifice diameter (6 in Fig. 3.4 or 4 in Fig. 3.5). d_o is the outer orifice diameter (9 in Fig. 3.4). I_d and U_d are the discharge current and voltage respectively.

This is the similar type of gas aggregation source as the NC-200, but with a different geometry, which allows higher pressures at comparable gas flow rates. The aggregation chamber consists of two sections (Fig. 3.5 left): a cylindrical section of 8.5 cm length and 10.4 cm diameter, and a cone-end cap of 9.8 cm length and 6 cm diameter. The balanced magnetron (Thin Film Consulting ION'X 2UHV, 2 in Fig. 3.5), equipped with a circular silver target of 2 inch diameter and 5 mm thickness, is used as a a vaporization source. It is connected to a DC power supply (Advanced Energy, MDX 500). An Ar/He mixture is employed as a working gas and the pressure was varied between 20 and 200 Pa, while the He partial pressure is varied between 0 and 30 Pa, with gas flow rates between 20 and 110 sccm for Ar and between 30 and 100 sccm for He. The working gas conditions were controlled and monitored by a two channel flux controller system (MKS Multi Gas Controller, 647C and 2 MKS Mass-Flow Controllers). Table 3.3.2 summarizes the range of experimental conditions and their typical values for both nanocluster sources.

3.4. Remote control

A remote control of the experimental setup, i.e. NC-200, was developed to improve the quality of control of the experimental parameters and accuracy of diagnostics. It consists of following independent blocks (Fig. 3.6)

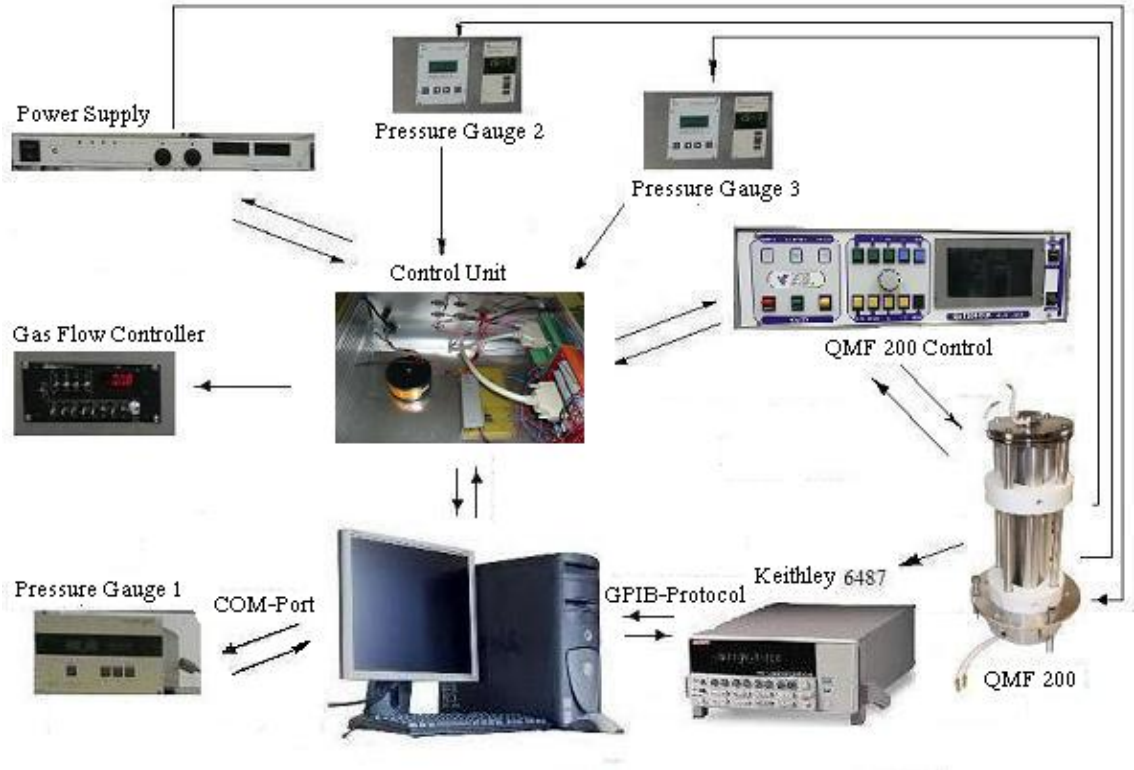

Figure 3.6.: Diagram of the remote control developed in the present work. Most of the devices are controlled via the control unit box (photo in the center) where interface connections to measurement cards and additional electronics are placed. Pressure gauge 1 control Balzers IMG 300 and femtoamperemeter Keithley 6487 are controlled directly from the computer via RS-232 and GPIB protocols respectively. Thanks to Anastasia Schiller for this picture.

- temperature control, i.e. temperature measurement and cooling control,
- pressure measurement,
- gas flow control (two channels),
- discharge control,
- QMF control.

The MKS 247 gas flow controller, pressure gauges 2 and 3 (Fig. 3.4), power supply, and the QMF200 control are controlled via the control unit box (Fig. 3.6, photo in the center), where the interface connections to measurement cards and additional electronics are placed. Pressure gauge 1 control Balzers IMG 300 and femtoamperemeter Keithley 6487 are controlled directly from the computer via RS-232 and GPIB protocols, respectively. Details on the control unit box are presented in Fig. B.2 in Appendix B. The operator

panel of the developed Labview software and its description are shown in Fig. B.1 in Appendix B.

The developed control unit has a number of advantages which allow to perform more accurate and reliable experiments. First, the automatic temperature control for the experiments involving cooling of the aggregation chamber walls by liquid nitrogen accurately keeps the temperature at the given threshold. This accuracy is almost impossible to achieve manually due to the amount of experimental parameters to control. The second important advantage concerns the cluster ion measurement directly from the QMF detection plate using a very accurate Keithley 6487 femtoamperemeter. This kind of connection significantly improves the signal-to-noise ratio and avoids the accuracy losses due to the limited resolution of AD and DA converters embedded in the QMF200 control unit. It is, however, not considered by the software delivered together with the QMF. Therefore, I developed the Labview software to enable us to simultaneously control the AC voltage on the QMF rods and the measurement of the cluster ion current on the QMF detection plate. This modification allows measuring the cluster ion current below 10^{-12} A and measurements [45, 83] would not be possible without it. The advantage of the automatic control of the other experimental parameters is a continuous log of all changes of experimental conditions controlled during the experiment. The Labview-software creates the log-file for every experiment and registers all changes of the experimental conditions. This allows us to consider some unexpected changes of experimental parameters that is important for further data processing. Another advantage of the developed system is its flexibility. The software consists of independent modules and can be easily adjusted in order to carry out an experiment in the fastest and the most accurate way.

3.5. Investigation of the cluster beam

3.5.1. Quadrupole mass filter

The quadrupole mass spectrometer was invented in 1953 by Wolfgang Paul [131]. In brief, it consists of four electrodes of cylindrical or hyperbolic shape, which are placed on a distance a from the z-axis. These electrodes are bound in pairs and biased with the AC voltage

$$\pm\frac{1}{2}(U + V\cos\omega t). \tag{3.1}$$

This leads to the motion equations for ions of charge e and mass M [131]

$$\ddot{x} + \frac{e}{Ma^2}\left(U + V\cos\omega t\right)x = 0 \tag{3.2}$$

$$\ddot{y} - \frac{e}{Ma^2}\left(U + V\cos\omega t\right)y = 0 \tag{3.3}$$

$$\ddot{z} = 0 \tag{3.4}$$

The equation (3.4) has the solution $v_z = \dot{z}$ =const. Defining [132]

$$a_u = a_x = -a_y = \frac{4eU}{M\omega^2 a^2} \tag{3.5}$$

$$q_u = q_x = -q_y = \frac{2eV}{M\omega^2 a^2} \tag{3.6}$$

$$\xi = \frac{\omega t}{2} \tag{3.7}$$

both equations (3.2) and (3.3) have the form

$$\frac{d^2u}{d\xi^2} + (a_u - 2q_u \cos 2\xi)\, u = 0 \tag{3.8}$$

where u represents either x or y. The equation (3.8) is a Mathieu equation in its canonical form [132].

Qualitatively, the ion motion in the QMF can be understood by considering the separate effects of the positive $(X - Z)$ and negative $(Y - Z)$ planes. In the positive plane, ions lie at the bottom of the potential well and oscillate under the action of the electric field. The oscillation amplitude increases with the mass of the ion, and therefore heavy ions are more likely to be lost at the QMF rods. Thus, the $X-Z$ plane acts as a low-pass mass filter. In the same manner, the $Y-Z$ plane works as a high-pass mass filter and the combination of both planes can be considered as a band-pass mass filter [133]. Analysis of the solutions of the Mathieu equation (3.8) results in a stability diagram which has been well studied by various researchers [131–139]. The stability diagram represents the field of stability of the solutions of the Mathieu equation as a function of the parameters a_u and q_u. These parameters define the stability of the ion trajectories in the mentioned $X - Z$ and $Y - Z$ planes and allow to determine the peak M and the width ΔM_R of the pass mass band [133] as [140]

$$M = 7 \times 10^7 \frac{k_c V}{f^2 d_q^2} \tag{3.9}$$

$$\Delta M_R = M\ 7.936 \left(0.16784 - \frac{U}{V}\right) \tag{3.10}$$

where $d_q = 25.4$ mm is the QMF rod diameter and k_c is the calibration factor. In the present work I use $k_c = 1.3$ based on the test data of Oxford Applied Research [140]. As can be seen from the equation (3.10), the pass mass band ΔM_R is proportional to the ion mass M. Thus, it will be low for smaller ions and high for heavier ions. Evidently, the real device resolution cannot be infinitely small, but it has a certain limit. For the quadrupole mass filter the limiting resolution ΔM_L is defined by its rod length L, frequency of the AC voltage f, and the kinetic energy of the entering ions V_z [136]

$$\Delta M_L = \frac{4 \times 10^9 V_z}{f^2 L^2}. \tag{3.11}$$

Considering ΔM_L and ΔM_R as two independent contributions to the total mass resolution ΔM, ΔM can be expressed as

$$\Delta M = \sqrt{\Delta M_L^2 + \Delta M_R^2}. \tag{3.12}$$

Furthermore, it is important to mention the following QMF drawbacks concerning its sensitivity, which could be important for reliable and reproducible measurements. First, the QMF sensitivity depends on the resolution, i.e. the U/V ratio [135, 136]. Since the amplitude of ion oscillations in the QMF depends on the U/V [132], an increase in this ratio leads to a greater fraction of the ion flux losses due to the axial dispersion [136]. It is therefore important to keep the ratio U/V constant during the measurement, to avoid distortion of the mass spectra. Second, the QMF sensitivity depends on the ion mass, i.e. heavier ions tend to be transmitted less effectively. This effect is often observed when operating at the highest practical resolution [136]. The highest QMF resolution in the present work is $M/\Delta M \approx 3$. Since in [136] no mass discrimination for sensitivity was observed for resolutions below 40, the effect of the cluster mass on the QMF sensitivity can be neglected for the conditions in the present work.

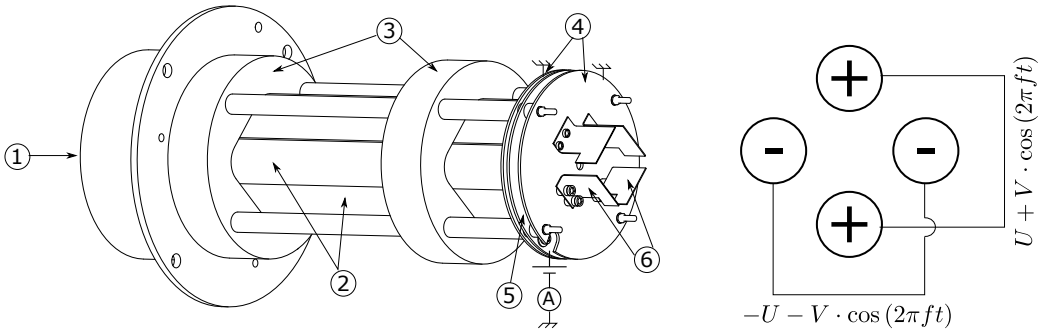

Figure 3.7.: Quadrupole mass spectrometer QMF-200. Left: schematics of the QMF-200, where 1–cluster injection, 2–quadrupole rods, 3–dielectric isolation, 4–grounded plates, 5–ion detector plate, 6–deflection plates. Right: front view of the quadrupole rods. Thanks to Michael Beck for the QMF drawing (left). Reprinted from [45].

In the present work a commercially available quadrupole mass filter QMF200 (Oxford Applied Research) was used to measure the mass spectra of the produced nano-size cluster ions. Fig. 3.7(left) shows the schematics of the QMF200. Cluster ions enter through the aperture 1 and oscillate in the quadrupole field caused by biasing of the QMF rods 2 by a AC voltage (3.1) as shown in Fig. 3.7(right). If their trajectories are stable, they hit the QMF detector plate 5, or they proceed through the detection plate aperture of 4 mm diameter towards the deposition chamber. On their pathway these cluster ions can be focused or deflected by biasing of the deflection plates 6. The inner and outer plates 4 are grounded and have apertures of 12 mm and 6 mm diameter, respectively. The QMF frequency f can be varied in the range of 3–100 kHz, and the amplitude of the AC voltage V in the range of 1–250 V. This limits the mass range of particles to

be measured and filtered to 30–3×10^6 amu [140]. To avoid the aforementioned cluster ion intensity variation due to the resolution change, the ratio U/V is kept constant during the measurement. For the mass spectrometric investigations a typical value of $U/V = 0.1$ was used. For the IVDF measurements of mass selected clusters the value $U/V = 0.12$ was applied.

3.5.2. Evaluation of the cluster size distribution function

The dependence of the total QMF resolution on the cluster mass (3.10)–(3.12) can distort the shape of the mass spectra. Therefore, an evaluation of the cluster size distribution function is required for a proper comparison with the theoretical models to gain information about the cluster formation processes. The mathematical meaning of the distribution function $f(M)$ is a density of particles of size M, that is, the number of particles of size M occurring within the interval ΔM [141]. An analysis of the QMF peak shape [142] and numerical simulations of the QMF transmission [143–145] suggest that the instrument function of QMF can be fairly approximated by the rectangular function. This means the linear particle density within the resolution interval. Considering the proportionality of the measured ion current to the cluster ion density, the following expression can be used to evaluate the cluster size distribution function

$$f(M) = \frac{I(M)}{\Delta M} \tag{3.13}$$

where $f(M)$ is the cluster size distribution function, M the cluster mass, $I(M)$ the cluster ion current measured at the QMF detection plate for clusters of size M, and ΔM is the total QMF resolution evaluated using the equation (3.12). Such a procedure closely approximates the number of particles which would have been observed if equal size intervals had been taken. Simultaneously, it yields a curve more truly representative of the system [141]. A sample cluster size distribution function evaluated in the present work using (3.13) is shown as a solid line in Fig. 2.3d. However, since the limiting QMF resolution depends on the kinetic energy of the entering ions, to evaluate the cluster size distribution function it is necessary to first measure the cluster velocities.

3.5.3. Retarding field analyzer

The measurement of the ion velocity distribution functions is a constantly recurring problem in plasma physics [146]. Retarding field analyzers (RFA) are most often used because of their simple implementation and low costs. In Fig. 3.8 two typical types of RFA are presented. On the right (Fig. 3.8a) the basic RFA is displayed. It consists of a grid or an apertured plate **S**, which can be grounded or biased with a constant voltage V_S, and a collector plate **C** biased with various voltages. Only ions with kinetic energies larger than the resulting potential barrier will eventually reach the collector. Fig. 3.9a shows the ideal current-voltage characteristic for monoenergetic particles. Thus, in ideal case, after the potential barrier exceeds the kinetic energy of ions, zero current is detected. In the case of real experiment, however, the measured current-voltage charac-

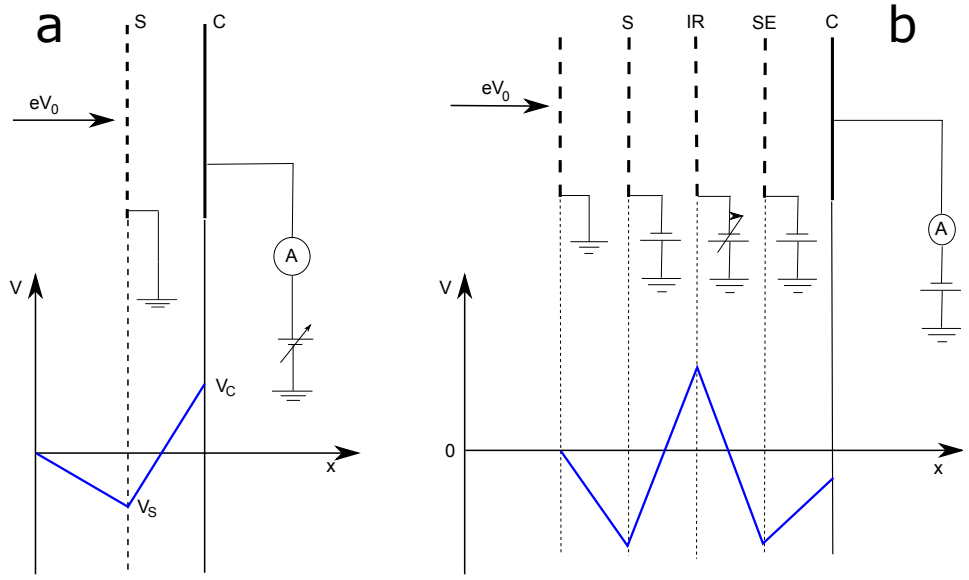

Figure 3.8.: Principles of the retarding field analyzer. a: basic RFA schematics (top) and potential (bottom). b: multi-grid RFA schematics (top) and potential (bottom).

teristic is influenced by such factors as limited RFA resolution and secondary electron emission. Thus, its shape (Fig. 3.9b) differs from the ideal shape. The full width of the real curve ΔV accounts for the RFA resolution caused by a finite angular aperture [147]. The distortion of the measured curve, shown as a dashed line in Fig. 3.9, is caused by effects related to secondary electron emission [147].

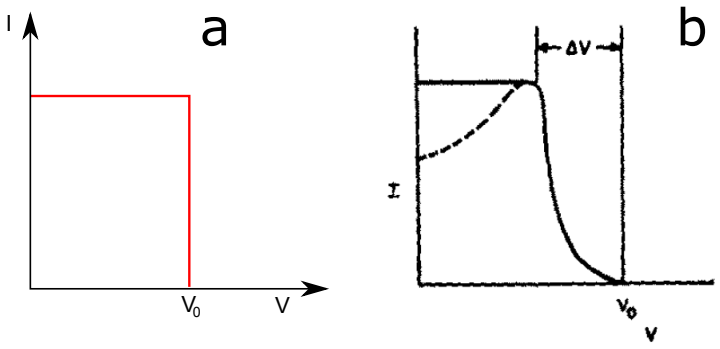

Figure 3.9.: a: Ideal cutoff curve for monoenergetic particles. b: Usual experimental retarding field cutoff curve (reprinted from [147]).

Thus, the main drawback of the basic RFA (Fig. 3.8a) is the absence of secondary electron suppression, which can distort the measured current-voltage characteristic and cause a misinterpretation of the experimental results. To overcome this problem, a multi-grid RFA (Fig. 3.8b) is frequently used for plasma diagnostics [148–151]. The main principle of such an RFA is illustrated in the Fig. 3.8b. The first grid, i.e. floating

grid, is usually grounded to avoid influence of the plasma potential. The charge selection grid **S** is aimed at rejecting particles of unwanted charge and is biased with a constant voltage. The voltage on the ion retarding grid **IR** is swept to measure the current-voltage characteristic. The **SE** is biased with a negative voltage and acts as a secondary electron suppressor. Finally, the ions which penetrate through all grids are detected at the collector plate **C**. The main drawback of the multi-grid RFA is a significant reduction in the signal due to the limited grid transmission. Moreover, computer simulations [152] show that the final transmission strongly depends on the grid arrangement. This serious drawback does not allow us to apply the multi-grid RFA for IVDF measurements of mass selected nanocluster ions. Other drawbacks of the multi-grid RFA are discussed in detail by [146, 151].

The measured current-voltage characteristic using one of the two RFA types allows for evaluation of the ion velocity distribution function (IVDF) as follows. The ion velocity distribution function $f(v)$ is proportional to the derivative of the collection current for a single species [146, 153]

$$\frac{dI(V)}{dV} = \frac{e^2}{M} f(v), \tag{3.14}$$

where V is a retarding potential, M an ion mass, e an elementary charge, and velocity $v = \sqrt{|2eV/M|}$. Thus, the RFA technique allows us to measure the ion velocity distribution function. The difference between energy and velocity distribution functions is discussed in detail by Ellmer et. al. [154].

3.5.4. Measurement of the IVDF of mass selected clusters

A combination of a mass spectrometer and various RFAs is typically applied in plasma monitors [155–158]. In the present work, the IVDFs of mass selected nanoclusters were also measured by a combination of QMF and basic RFA techniques, but with one important difference. Whereas mass selection is commonly placed after the RFA in plasma monitors, in the present work preliminary mass selection is necessary. This is because the broad size range of nanoclusters produced by the source can cause a misleading evaluation of the measured current-voltage characteristics. Thus, in the present work, the RFA is placed after the QMF.

Fig. 3.10 represents the schematics of the connection of the QMF plates as the basic parallel plate retarding field analyzer. The entrance plate with an orifice of radius $r_0 = 6$ mm is grounded. The collector (**C** in Fig. 3.10) is situated at a distance $d = 3$ mm from the entrance plate. Cluster ions of the selected size proceed towards the QMF detector, which is biased by the voltage V in the range of ± 500 V with a step of 1 V, and which acts as a collector **C** of RFA (Fig. 3.10). The limiting resolution of such an RFA is determined mainly by its finite entering aperture and can be estimated as follows [147]:

$$\frac{\Delta E}{E} = \sin^2\left(\frac{r_0}{4d}\right) \approx 0.23, \tag{3.15}$$

where $r_0 = 6$ mm is the aperture radius, and $d = 3$ mm is the interplate distance (Fig. 3.10).

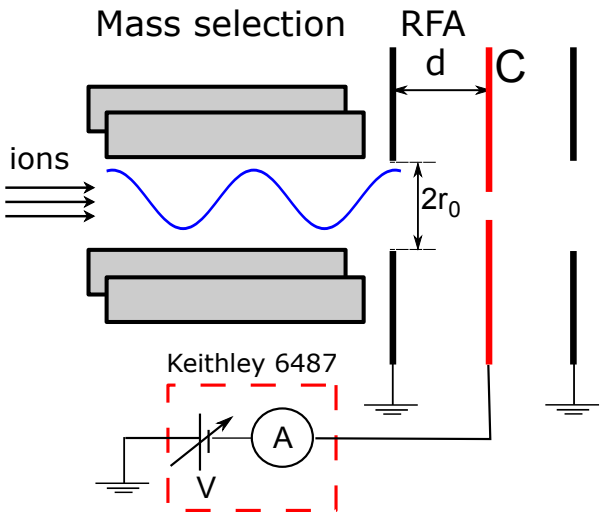

Figure 3.10.: Schematics of the connection of the QMF plates as a basic RFA. **C** is a QMF detector acting as a RFA collector where the ion current is measured. The radius of the input aperture $r_0 = 6$ mm, interplate distance $d = 3$ mm. Radius of the collector aperture is 2 mm. Suggested to be published in [83].

Another important question is whether the QMF influences the cluster ion velocity distribution. Theoretically, according the solution of equation (3.4), the axial velocity is constant. However, one can not exclude the influence of fringing field effects or other effects caused by field imperfections, finite orifice, etcetera [136]. Since theoretically the cluster velocity should not change, and since no IVDF broadening, e.g. simulated for QMF with pre-filter by [159], was observed during the experiments, in the present work the influence of the QMF on the cluster IVDF is neglected. However, to my knowledge, there is a lack of data on this topic in the literature. It is therefore an interesting question for future investigations.

3.6. Investigation of clusters deposited on the surface

3.6.1. TEM

A transmission electron microscope (TEM) typically, consists of an illumination system, a specimen stage, an objective lens system, a magnification system, a data recording system, and a chemical analysis system [160]. The entrance surface of a specimen is illuminated by a parallel, or almost parallel, electron beam. The electron beam is diffracted by the crystal lattices of the specimen and forms Bragg beams which propagate in different directions. The electron-specimen interactions cause phase and amplitude changes in the electron wave. This wave is transmitted non-linearly by the objective lens system. The diffracted beams are focused in the back focal plane where an objective aperture could be applied [160]. A high-resolution TEM image of a crystalline specimen is formed by the interference of the Bragg reflected beams [160].

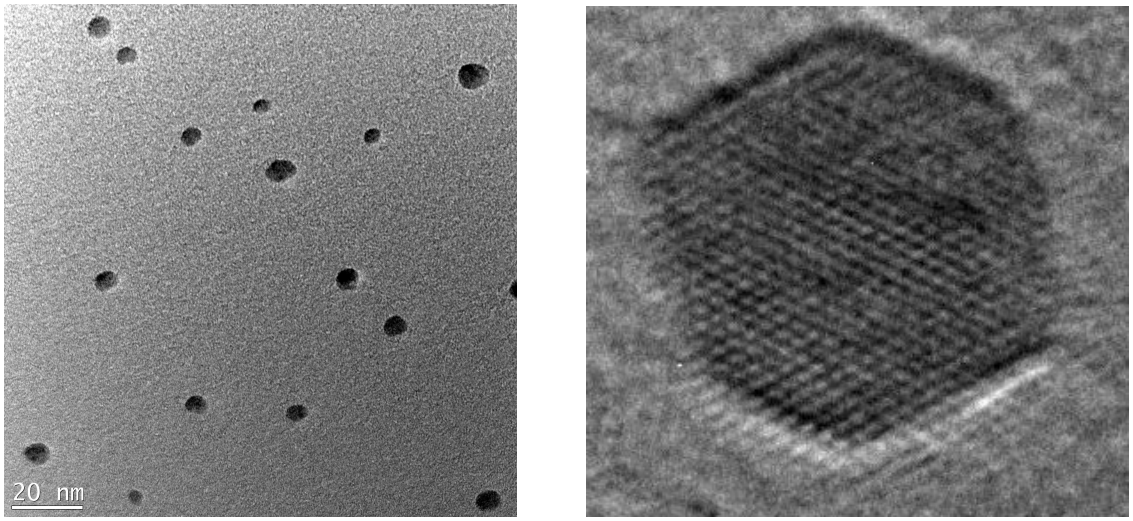

Figure 3.11.: Left: TEM image of deposited silver clusters. Right: high resolution TEM image of a single silver cluster of about 5 nm diameter. Thanks to the group of Prof. Kienle (Kiel) for the pictures.

In the present work, nanocluster samples deposited on carbon coated copper grids were investigated using a TEM Tecnai F 30 G2 produced by Phillips. Fig. 3.11 shows the TEM image of silver clusters deposited using the high pressure nanocluster source (left), and a high-resolution TEM image of a single silver cluster of about 5 nm diameter (right).

3.6.2. AFM

Atomic force microscopy (AFM) was invented in 1985 by Binning, Quate and Gerber [162]. It is based on the measurement of different forces between a sharp tip and the sample surface, e.g. attractive, repulsive, magnetic, electrostatic, van der Waals forces [161]. In Fig. 3.12 (left) the principle of AFM is shown. The tip, typically of nm or μm size, moves across the specimen surface and imaging is accomplished by the measuring of the interaction force via deflection of a soft cantilever [161]. Two AFM modes can be distinguished: contact and tapping. In the contact mode, the tip approaches the sample surface. In the tapping mode, the tip is driven near its resonance frequency by means of a piezo oscillator (Fig. 3.12, left). Thus, only intermittent contact occurs between the tip and the sample [161], which avoids the scratching of soft samples. In the tapping mode, information about the sample surface morphology is retrieved from the amplitude signal of the oscillating cantilever [161]. The AFM can be operated either in constant force mode, or in constant height mode. In the constant force mode, the cantilever deflection is kept constant by readjusting the vertical position of the sample. In the constant height mode, the vertical position of the specimen is kept constant and the varying deflection of the cantilever is recorded [161].

The AFM measurements in the present work were performed using the NanoScope IV

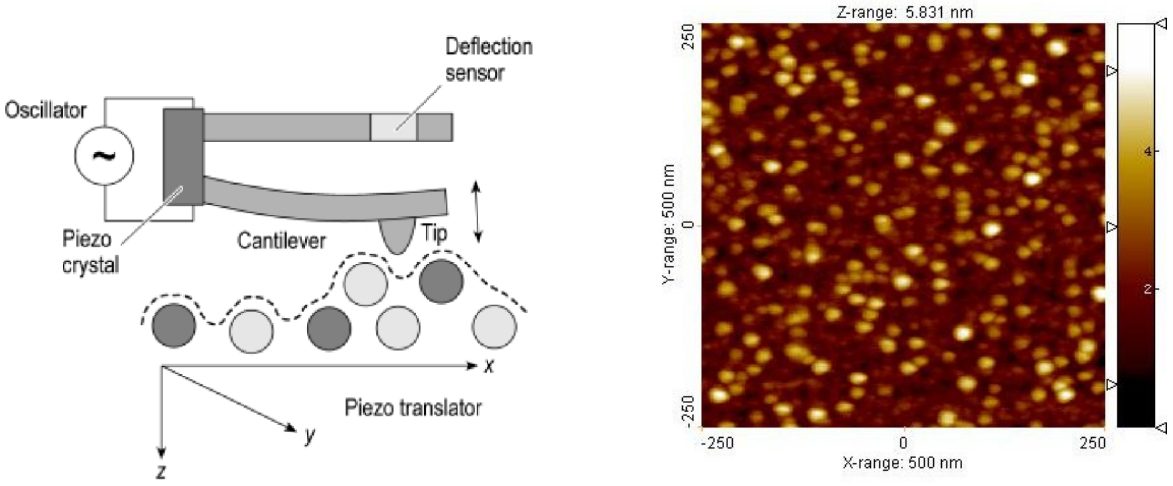

Figure 3.12.: Left: principle of AFM. Reprinted from [161]. Right: AFM image of copper clusters on Si substrate. Thanks to Dr. Oxana Ivanova from the group of Prof. Helm for this picture.

produced by Veeco Instr, USA, in the tapping mode under ambient conditions. Si tips with nominal curvature radii of 10 nm and 12 nm and a resonance frequency of 428 kHz were used.

3.6.3. SEM

Scanning electron microscopy (SEM) was invented in the 1930s [163–165]. A detailed description of SEM principles and limitations is provided in for example [166]. Its operation principles can be summarized as follows. The electron beam of a defined diameter, current and divergence enters the object chamber and interacts with a certain area of a specimen. The wide range of interactions generates a signal of various charged particles and photons, such as elastically scattered, inelastically scattered, backscattered, absorbed, Auger, and secondary electrons, x-ray photons, and photons of visible light. By collecting these signals, image of the specimen morphological structure, chemical spectrum, or diffraction pattern can be obtained. To investigate the whole specimen, the electron beam is shifted using the scanning systems [166, 167]. In the current work, FEG ICON SEM was used.

3.6.4. XPS

X-ray photoelectron spectroscopy (XPS) is used for chemical analysis of the deposited film. The specimen surface is irradiated with soft X-ray photons, which causes the ejection of a core level electron. Because no two elements share the same set of electronic binding energies, the measurement of the photoelectron kinetic energies enables elemental analysis. XPS can be used for the analysis of all elements in the periodic table except

for hydrogen and helium [168].

In the present work, XPS measurements of the deposited copper clusters were performed using the CLAM2 Multi-technique 100 mm hemispherical electron analyzer X-ray photoelectron spectroscope, produced by VG Microtech. Mg Kα radiation with photon energy of 1253 eV was used as the excitation source. Binding energy of Au $4f_{7/2}$, equal to 84 eV, was used as the reference. The XPS spectra were collected in a constant analyzer energy mode at pressure of 10^{-6} Pa in the chamber, and a pass energy of 23.5 eV at 0.125 eV per step.

Chapter 4

Results/Publications

This chapter summarizes the results of the present work, which are published or submitted as peer-reviewed articles.

Section 4.1

This section reports on the development and characterization of the conventional DC magnetron-based nanocluster source. The cluster beam produced by this source was characterized using the QMF and by analysis of clusters deposited on Si substrates. Even though the shift of the cluster mass spectra in time was noted and mentioned, no detailed analysis of this effect was performed.

- A. Majumdar, D. Köpp, **M. Ganeva**, D. Datta, S. Bhattacharyya, and R. Hippler
  Development of metal nanocluster ion source based on DC magnetron plasma sputtering at room temperature
  Review of Scientific Instruments, **80** (9), 095103 (2009).

Section 4.2

This section reports on the systematic investigation and quantitative characterization of the influence of target erosion on the mass spectra of clusters produced in a conventional DC magnetron-based gas aggregation source.

- **M. Ganeva**, A.V. Pipa, and R. Hippler:
  The influence of target erosion on the mass spectra of clusters formed in the planar DC magnetron sputtering source
  Surface and Coatings Technology, **213**, 41–47, (2012).

Section 4.3

Considering the effect of the target lifetime on the cluster mass spectra, it is possible to investigate influence of other experimental parameters, i.e. pressure, buffer gas, discharge power, etcetera, on the mass spectra. This section presents the results of the

mass spectrometric investigations of the beam of nano-size silver cluster ions produced by a high pressure DC magnetron-based nanocluster source.

- **M. Ganeva**, T. Peter, S. Bornholdt, H. Kersten, T. Strunskus, V. Zaporojtchenko, F. Faupel, and R. Hippler
  Mass Spectrometric Investigations of Nano-Size Cluster Ions Produced by High Pressure Magnetron Sputtering
  Contributions to Plasma Physics, **52** (10), 881–889, (2012).

Section 4.4

An important part of the cluster beam characterization is the measuring of its velocity distribution. The technique for measuring the velocity distribution functions of mass-selected nano-size clusters that was developed and applied in the present work, as well as the results, are presented in this section. This section contains also an analysis of the measured IVDF and a comparison of the experimental results with the theoretical model.

- **M. Ganeva**, A.V. Pipa, B.M. Smirnov, P. V. Kashtanov, and R. Hippler:
  Velocity distribution of mass-selected nano-size cluster ions
  Plasma Sources Sci. Technol., **22**, 045011, (2013).

Section 4.5

Finally, the investigation using the AFM, SEM and XPS techniques of Cu clusters deposited on Si substrates is reported in this section.

- A. Majumdar, **M. Ganeva**, D. Köpp, D. Datta, P. Mishra, S. Bhattacharyya, D. Ghose, and R. Hippler
  Surface morphology and composition of films grown by size-selected Cu nanoclusters
  Vacuum, **83** (4), 719–723, (2008).

4.1. Development of metal nanocluster ion source based on DC magnetron plasma sputtering at room temperature

Development of metal nanocluster ion source based on dc magnetron plasma sputtering at room temperature

Abhijit Majumdar,[1,a)] Daniel Köpp,[1] Marina Ganeva,[1] Debasish Datta,[2] Satyaranjan Bhattacharyya,[2] and Rainer Hippler[1]
[1]*Institut für Physik, Ernst-Moritz-Arndt-Universität Greifswald, Felix-Hausdorff-Str. 6, 17489 Greifswald, Germany*
[2]*Surface Physics Division, Saha Institute of Nuclear Physics, 1/AF Bidhan Nagar, Kolkata 700 064, India*

(Received 31 March 2009; accepted 8 August 2009; published online 4 September 2009)

A simple and cost effective nanocluster ion source for the deposition of size selected metal nanocluster has been developed based on the dc magnetron discharge (including pulsed dc discharge). The most important and interesting feature of this cluster source is that it is working at room temperature, cooled by chilled water during the experiment. There is no extraction unit in this device and the cluster streams flow only due to the pressure gradient from source chamber to substrate via quadrupole mass filter. It has provision of multiple substrate holders in the deposition chamber, which can be controlled manually. The facility consists of quadrupole mass filter (QMF 200), which can select masses in the range of 2–125 000 atoms depending on the target materials, with a constant mass resolution ($M/\Delta M \sim 25$). The dc magnetron discharge at a power of about 130 W with Ar as feed/buffer gas was used to produce the Cu nanocluster in an aggregation tube and deposited on Si (100) wafer temperature. © *2009 American Institute of Physics.*
[doi:10.1063/1.3213612]

I. INTRODUCTION

In the recent years the modern microelectronics industries exposed their view for the growth and modification of materials in the manufacturing processes. The applications of room temperature nanocluster are widely taken in the process. The production of microelectronics devices have created an interest in faster and more reliable methods of producing quality epitaxial as well as nanocrystalline thin films.[1,2] The biggest advantage of these nanoclusters is that it is highly reactive as the atoms level exposure on the surface of the materials lead to a very strong interaction between a nanocluster and its surroundings.[3,4] Developing new methods for use in the manufacturing processes require knowledge of the interaction of nanoclusters with their surrounding on the atomic level.

There are several techniques to deposit the nanoclusters, e.g., laser ablation,[5,6] pulsed arc plasma,[7] ion sputtering,[8] and continuous beam techniques by gas condensation.[9,10] Palasantzas *et al.*[11] mentioned the deposition of Cu nanoclusters at room temperature in dc magnetron plasma sputtering technique. The laser ablation technique has become the most popular because of its applicability in the wide range of materials but the pulsed nature of beam can affect the many applications. In the gas condensation technique continuous beam is often achievable and is commonly used to involve evaporation of materials by heating and subsequent cluster condensation by the introduction of inert cooling gas.[12] For the industrial purpose of view it may not be cost effective and may become complicated due to operation technique. Without involving the complication of the target heating process the plasma sputtering has become nowadays a well established technique for thin film deposition. Plasma sputtering with gas condensation was reported in 1986.[13] The technique has been improved and developed through the use of magnetron sputtering.[14–16] The room temperature cluster sources have been growing popularity for the industrial application purpose but the performance and reproducibility of such a cluster source depends on many interrelated factors and it has limitation due its thermal instability at coagulation chamber. To date a detailed account of this type of cluster source has not been reported. However, remarkable advances have taken place in cluster sources of gas condensation techniques. Haberland *et al.*[15–18] developed this kind of nanocluster sources with high fluxes of metal clusters of varied cluster sizes. Binns and co-workers[9,19] reported the design and operation of gas aggregation cluster ion sources at relatively high temperatures. Apart from copper nanocluster deposition on silicon substrates at room temperature,[11,20] De Hosson and co-workers[21–23] reported similar deposition of magnetic materials like, Co, Fe, etc., and discussed various aspects of cluster deposition and characterization in view to meet the advances and challenges of the subject. Apart from the nanoclusters of magnetic materials, this group reported growth front roughening of copper nanocluster films[20,23] having a narrow size distribution of clusters and other aspects of nanosized clusters.

In this paper, we report a detailed account of the design and results of a size selected Cu nanoclusters ion beam source based on dc magnetron plasma sputtering at room temperature. As innovation and motivation of the present

[a)]Author to whom correspondence should be addressed. Electronic mail: majumdar@physik.uni-greifswald.de. FAX: +493834864701.

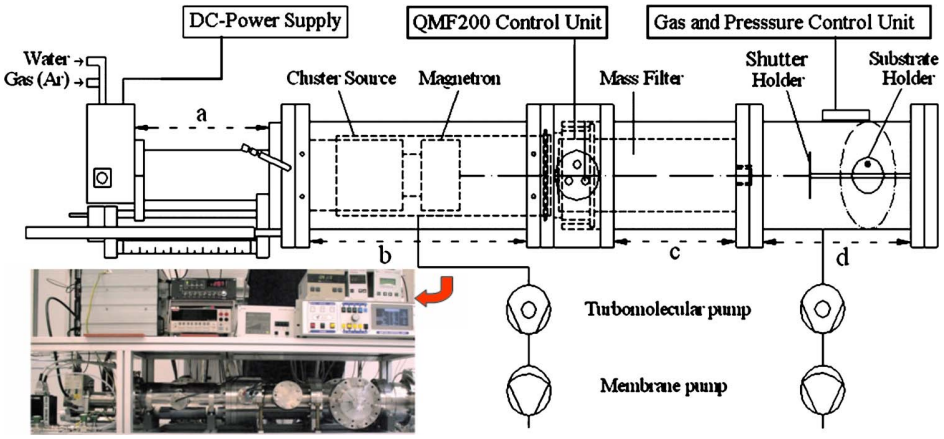

FIG. 1. (Color online) Schematic diagram of nanoclusters ion beam source based on dc magnetron sputtering.

work, the developed source has two major modifications/alterations as compared to other cluster sources reported so far. One of these two major contributions is that the developed source can be operated at room temperature and, therefore, has great advantage for application to the area of industries as well as fundamental researches. The other technical modification or simplicity of the facility is that there is no extraction unit in this device and the cluster streams are moving only due to the pressure gradient from source chamber to substrate via quadrupole mass filter.

II. APPARATUS

The schematic diagram of cluster source apparatus is shown in Fig. 1. The source consists of three main sections: cluster production, cluster beam formation, and mass selection, which are operated by differential pumping arrangement. Including these three sections, the whole cluster source setup is generalized by the assembly of several components which are the following: (A) Magnetron System (a) and sputtering chamber (b), (B) Quadrupole Mass filter unit (c), (C) Deposition chamber (d), (D) Pumping system, (E) Gas flow System, and (F) Electrical inputs

A. Magnetron system (a) and aggregation chamber (b)

The cluster source consists of three differential pumped sections: (i) cluster source [which is referred as sputtering chamber, as sections (a) and (b), length=41 cm], (ii) quadrupole mass filter [QMF 200, referred to as section (c), length=31 cm], and (iii) deposition chamber [referred to as section (d), length=28 cm]. A commercially available NC 200 nanocluster source (Oxford Applied Research) has been employed for the sputtering process. The magnetron gun is mounted on a long axial mount (a), which is enabling to change the distance, between front of the gun and the end of the chamber up to 15 cm (i.e., the aggregation tube length). The Ar is used as sputter gas, which has been injected through a small orifice (~2 mm) from the front side of the magnetron gun. The normal cooling water has been used to cool the magnetron during the discharge. The Ar plasma is ignited by applying a dc high voltage (~320–410 V and I =0.4 A) to the Cu target.[16–18] The Ar flow rate is regulated by mass flow controller (MKS Instruments) at a constant flow of 50 SCCM (standard cubic centimeter/minute). Clusters are formed by the attachment of the sputtered free atoms. The variable aggregation distance from the front of the magnetron gun to the exit nozzle has to be within an optimum range for production of large clusters. However, to obtain maximum cluster peak current there is an optimum aggregation distance of 10–13 cm. This is probably a characteristic of this setup in which the Ar gas is injected from small orifices at the front of the magnetron gun. The cluster and gas mixture leave the source chamber (b) through an aperture diameter of 8 mm, allowing independent control of the gas flow rate and gas pressure. The clusters flow from sputtering chamber toward deposition chamber with a pressure gradient of 10^{-3} mbar via quadrupole mass filter. The typical distance between the target material and the substrate is about 50 cm (depending upon the aggregation tube length).

B. Quadrupole mass filter unit (c)

Quadrupole mass filter (c) (QMF 200, frequency range 3–100 kHz, ac voltage range 0–250 V, dc voltage range 0–50 V, X-Y voltage −100 to +100 V, internal ammeter range ±0.04 to ±10 nA) is placed in between cluster source (b) and deposition chamber (d). Poles diameter and length are 2.54 and 25 cm, respectively. Total length of the quadrupole is 28.5 cm. After leaving the cluster source chamber the clusters and gas mixture enter into the quadrupole mass filter region. The grounded outer aperture diameter is 6 mm. While passing through quadrupole mass filter, it can produce clusters in the size range from 5 up to 125 000 atoms, depending on the target material, with a constant mass resolution ($M/\Delta M \sim 25$). In QMF 200 quadrupole mass filter clusters can be selected according to their mass to charge ratio by the quadrupole electric field so that only ions of a defined mass M will be transmitted.[24] The motion of ions inside the quadrupole is described by Mathieu equation.[25] The mass selection is controlled by the frequency f (kilohertz) and the amplitude of ac voltage V_{ac} (in volts),

$$M = 7 \times 10^7 k \frac{V_{ac}}{f^2 d^2}, \tag{1}$$

where M is the cluster mass in atomic mass units (amu), d =25.4 mm is the rod diameter, and k a correction factor is found to be 1.56.

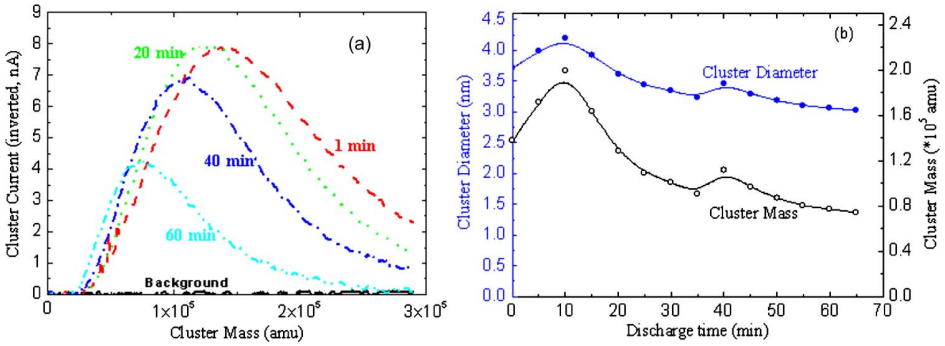

FIG. 2. (Color online) Quadrupole mass spectrum analysis of Cu nanocluster. (a) Variation of cluster mass (amu) and cluster current (nA) with respect to discharge time and (b) reproducibility of cluster diameter (nm) and cluster mass with discharge time.

C. Deposition chamber (d)

The deposition chamber is made of stainless steel. The inner dimensions of the chamber are height of 11.5 cm, length of 28 cm, and width of 2.2 cm. The substrate is placed 12 cm apart from the quadrupole orifice. Diameter of the orifice is 3 mm. Two storage turbo molecular pump (TMP) pump is placed at back side of the substrate holder. Four substrates (Si or glass, etc.) can be placed on this round shape substrate holder (as shown in Fig. 2), which is generally operated manually from outside of the chamber.

D. Pumping system

Vacuum system consists of (i) two turbo molecular pumps (Mod: TMU 521) (Pfeiffer Vacuum, DN 160 CF-F3P, with Electronic driver unit TC 600) and (ii) two roughed by diaphragm pumps (Pfeiffer Vacuum, Mod: MVP 055 −3) for roughing and backing up purpose. The base pressures in the cluster source and deposition chamber are $\sim 10^{-7}$ mbar and $\sim 10^{-8}$ mbar, respectively. After starting the experiment the pressure in the source and the deposition chamber are in the order of 10^{-1} mbar and 10^{-4} mbar, respectively. As the Ar gas flow is started a pressure difference in order of 10^{-3} mbar is generated between the source (magnetron chamber) and deposition chamber.

E. Gas flow system

Gas flow system consists of (i) Baratron (MKS Instruments 247, USA), (ii) multiple mass flow controller (100 SCCM, MKS Instruments, USA), and (iii) gas cylinder (Ar). Out of four channels of mass flow controller, only two channels are used in the prospective experiments. During cluster production, a typical gas pressure in the condensation chamber (d) is maintained and it is about 3.1×10^{1} mbar, with a gas flow rate of 50 SCCM (standard cubic centimeter). As it mentioned earlier that the, orifice diameter of magnetron source is larger than the deposition chamber (from Fig. 1). As the Ar gas flow is started a pressure difference in order of 10^{-3} mbar is generated between the source (magnetron chamber) and the deposition chamber. Due to this pressure gradient the coagulated/fragmented cluster atoms and other particles flow from magnetron source toward the deposition chamber via mass filter.

F. Electrical inputs

The electrical system accompanied by dc power supply [GLASSMAN EUROPE Ltd. (LP 600–2) dc power supply 0–600 V with 0–2 A current]. The whole system (including cluster source, mass filter, and the deposition chamber) is grounded. There was no extra "+/−" potential applied to the substrate to attract/repel the cluster particles toward the deposition chamber. The dc magnetron discharge at a power of about 130 W with Ar as feed gas (50 SCCM) was used to produce the Cu nanocluster at room temperature.

III. OPERATION CONDITIONS AND REPRODUCIBILITY

The whole apparatus has to be evacuated by two TMP pumps along with two membrane pumps, around 2–3 h before any experiment until the base pressure reached up to $\sim 10^{-7}$ mbar in source chamber (a) and in deposition chamber (d) at 10^{-8} mbar. Ar gas has been injected from small orifices at the front of the magnetron gun and 10^{-3} mbar pressure has been maintained by controlling the gas flow system in between source and condensation chamber (d, deposition chamber). The water cooling should be started 30 min or 1 h before the experiment (precooling process). Since the present cluster source is operated at room temperature, the main limitation of room temperature cluster source is that the sputtering yield of the target materials should be high (>1). Discharge power is high in case of lower sputter yield materials and in such case the thermal instability disturbs the cluster formation processes. Lower sputtering yield materials need high discharge power to sputter it and it results to the thermal instability in the source chamber. Due to the high temperature effect and thermal instability in the source chamber the sputter atoms could not get the optimum environment to coagulate to form a cluster. To avoid such circumstances the discharge power will be low to sputter the surface atoms from the target materials. The clusters can be detected only within an optimum range of dc power, depending on the target material. Also, when the dc power is too high the plasma becomes unstable, resulting in secondary plasma as well as an intermittent cluster beam current. Figure 2(a) shows the dynamics of the cluster mass spectra with time. The most probable cluster mass shifted toward the smaller values with time. With the increase in wall (source chamber) temperature the most probable cluster mass also have the same tendency to shift toward smaller mass value (cooling by liquid nitrogen).[26] Figure 2(b) shows the variation of cluster diameter (nanometer) as well as the most probable mass (amu) with discharge time (minute). The decrease in the cluster current with the discharge time can be explained due to an influence of changing of the target pro-

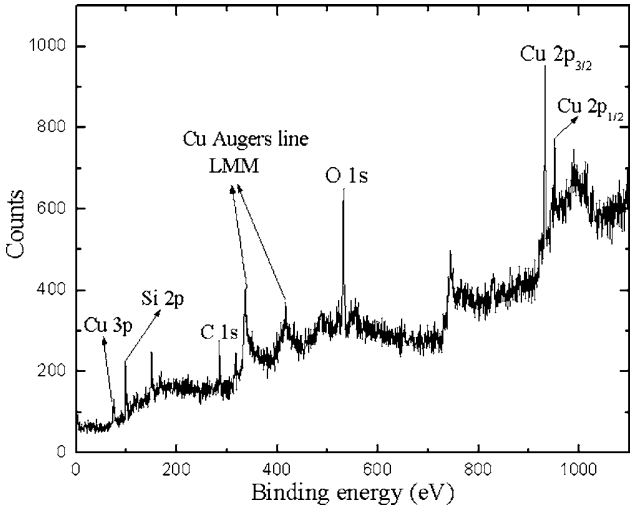

FIG. 3. X-ray photoelectron spectrum of the Cu nanocluster film deposited on Si (100) substrate.

file. It is very interesting to see that the shift of the cluster mass in certain time span is taken place and observation compiled us to reconsider the actual mechanism of cluster formation process in such device.

The reliability of room temperature cluster source is somewhat problematic. Several factors are found to be responsible strongly to influence the cluster production. Instead of liquid nitrogen, the normal chilled water could influence the thermal instability (or thermally nonequilibrium state) in the sputtering unit. Longer time discharge effectively enhanced the generation of secondary plasma in front of the magnetron target material and this creates plasma turbulence inside the source chamber and consequently the cluster formation hampers. The cluster size distribution can be influenced by the deformation of the target surface. When a new smooth target is used, the source produces smaller clusters than when the target is eroded.[12]

IV. RESULTS AND DISCUSSION

A. X-ray photoelectron spectroscopy

X-ray photoelectron spectroscopy (XPS) measurements of the Cu nanoclusters were performed on a VG Microtech (CLAM2: Multitechnique 100 mm hemispherical electron analyzer) x-ray photoelectron spectroscope, using Mg $K\alpha$ radiation (photon energy 1253 eV) as the excitation source and the binding energy of Au (Au $4f_{7/2}$: 84.00 eV) as the reference. The XPS spectra were collected in a constant analyzer energy mode, at a chamber pressure 10^{-8} mbar and pass energy of 23.5 eV at 0.125 eV/step. Figure 3 shows the photoelectron spectrum of the Cu nanocluster film. Cu $2p$, Cu $3p$, Si $2p$, Si $2s$, and O $1s$ bonds have been observed in the XPS analysis. A clear image of the possible chemical bonds of cupper can be deduced from a deconvolution of the individual Cu $2p$ and Cu $3p$ lines into Gaussian line shapes.[27,28] Cu $2p$, Cu $3p$, Si $2p$, Si $2s$, and O $1s$ bonds have been observed in the XPS analysis. The detailed peak analysis is not discussed here. It have been found that copper is ~12.65%, oxygen ~41.28%, metal oxide (CuO) ~ 10.50%, Si ~ 26.43%, and Si–O ~ 9.13% in the deposited Cu nanocluster film. Moreover it is obvious that the deposited Cu nanocluster film is highly oxidized due to air contamination or the oxygen connected to Si wafer surface.

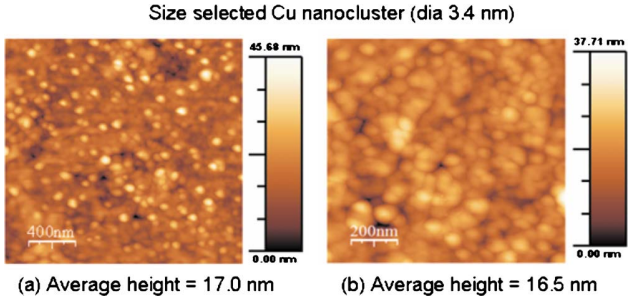

FIG. 4. (Color online) AFM analysis of Cu nanocluster (diameter=3.4) deposited on Si substrate showing two dimensional image with rms roughness of (a) 4.7 nm and average height of 17 nm and (b) 5.4 nm and average height of 16.5 nm. These two images were taken from two regions of the deposited films.

B. Atomic force microscopy

Atomic force microscopy (AFM) of Cu sample was performed in NanoScope IV (Veeco Instr., USA) in the tapping mode under ambient condition using Si tip of nominal radius of curvature 10 nm having a resonance frequency of 428 kHz. The images thus obtained were flattened using the software provided by this AFM. The investigation of the morphology of Cu nanocluster films was carried out to get an idea about the height of the Cu nanoclusters agglomerated on the Si substrate. Figure 4 shows the morphology of the film examined by AFM. The AFM images shown in this figure represent the topographical features due to Cu-nanocluster deposition all over the scanned area. Analysis of the AFM images shows that the average height of the islands is about 17 nm, whereas the diameters of these islands are about 80 nm that we found from scanning electron microscopy (SEM) images (Fig. 5). This means that the clusters are flattened due to impact energy of the clusters on the substrate. The size of the free Cu nanocluster was 3.4 nm and a cluster contained about 1700 Cu atoms.

C. Scanning electron microscopy and energy dispersive x-ray

Cu nanocluster films were examined by SEM with energy dispersive x-ray (EDX) (FEG ICON) facility. The SEM was employed for this investigation in a number of tilt angles to the sample surface to get an idea about the heights of the morphological features. The EDX spectra were taken both in the region and in the spot modes for 100 s in each case. Figure 5 shows the morphological behavior of Cu nanoclusters films deposited on Si (100) substrate. The SEM observation of Cu nanoclusters films reveals that initial nucleation of Cu clusters takes place in the form of isolated island and the arrival of subsequent Cu clusters on to Si substrates has preferential aggregation around the preceding clusters forming a structure as seen in Fig. 5(a). The image of this figure shows that some parts are locally populated by Cu clusters (white contrast in the images), while the remaining (black

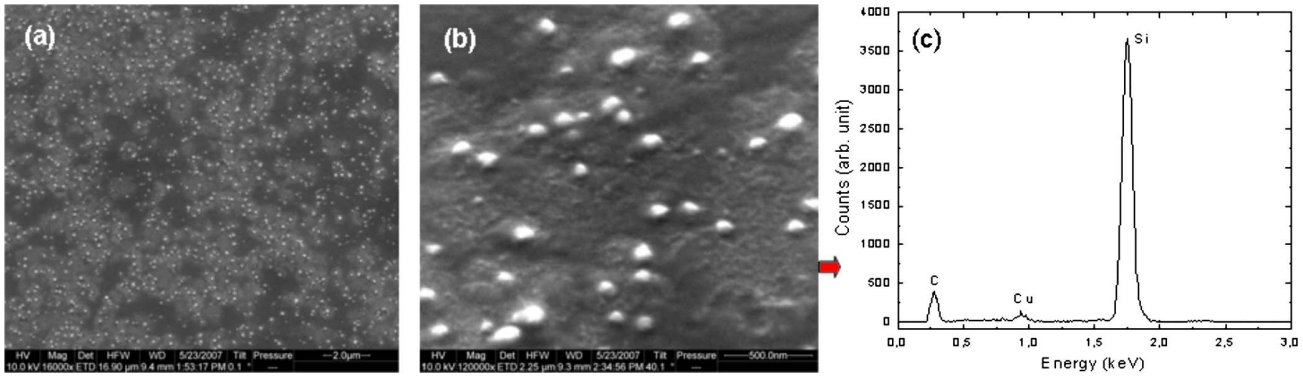

FIG. 5. (Color online) SEM of the size-selected (diameter=3.4 nm) Cu nanocluster film deposited on Si substrate. (a) represents the image of typical morphology at relatively lower magnification. (b) is an image taken at higher magnification at a tilt angle of 40° with surface normal and (c) is its corresponding EDX pattern in the region mode.

region) portion are still Si rich. Some tiny clusters islands are also seen in the image. The morphology of these samples also shows irregular cluster islands with varied size distributions. Figure 5(b) shows an image taken from the central part of the deposited film at higher magnification and here Cu islands are more prominent. Along with the morphological studies, EDX spectra corresponding to the SEM images were taken both at region and spot modes. The SEM studies of Cu nanoclusters films reveal that initial nucleation of Cu clusters takes place in the form of isolated island and the arrival of subsequent Cu clusters on to Si substrates has preferential aggregation around the preceding clusters forming an island structure. The image of this figure shows that some parts are locally populated by Cu clusters (white contrast in the images), while the remaining (black region) portion are still Si rich. Some tiny islands of clusters are also seen in the image. The EDX spectra were taken from a white contrast region, where Cu rich clusters are presumably considered. The EDX pattern clearly shows only a trace signature of Cu has arrived at the region shown in Fig. 5(c).

From the above observations of morphologies using AFM and SEM, one can get an idea about the process of cluster deposition on a surface. In general, during and after the deposition of clusters on a substrate a new kind of interaction between energetic clusters and the surface occurs. Depending on the substrate, diffusion of clusters takes place on the surface. In the present case, initially when Cu nanoclusters are incident on the Si substrate, surface coverage is low and gradually with time, the clusters are diffused on the surface to form islands. It is likely, Cu clusters form a continuous film with a distribution of cluster sizes after possible restructuring due to diffusion and interaction of the clusters.

The final structures of nanoclusters start by the nucleation via one of the following processes, namely, (i) DLA-model (diffusion limited aggregation)[29–32] and (ii) DDA-model (deposition diffusion aggregation).[33] DLA model is based on the mechanism of joining of solid particles on a surface, while DDA model accounts for diffusion motion of particles on the surface. This model developed under various conditions was analyzed[34] and can be applied to the present case. According to DLA model, a cluster is assembled by adding individual particles to it. A definite number of particles are introduced into the formation region initially and the particles coalesce when they collide with one another. This will initially result in the appearance of a larger number of smaller clusters, and subsequent collisions will lead to their aggregation. Deposition on a substrate leads to an ultrathin film initially and then with time a relatively thicker film is grown. Since the functions and dynamic behaviors of particles strongly depend on their size, well-defined monodispersed particles are ideal for the application to advanced devices as well as models for fundamental studies. Although in the present study this aspect was considered a priority, further improvement is necessary to get monodisperse yields with narrow size distribution of nanoparticles using a mass selected charged cluster beam.

V. CONCLUSIONS

In conclusion, a simple and inexpensive metal nanocluster source driven at room temperature is developed to get charged metal nanocluster using magnetron sputtering process. The films thus composed by mass-selected Cu nanoclusters are analyzed by XPS, SEM/EDX, and AFM to get an idea about the morphological evolution on Si substrates. The result is discussed in the light of existing models of nanocluster film formation where the clusters are moving from source to deposition chamber by the ambient pressure gradient. More works in this direction will elucidate better understanding of morphological behavior and other novel properties of metal nanocluster films.

ACKNOWLEDGMENTS

Part of this work was supported by the Deutsche Forschungsgemeinschaft (DFG) through Sonderforschungsbereich SFB/TR24 "Fundamentals of Complex Plasmas," by the Federal Ministry of Education and Research (BMBF) and by The International Max-Planck Research School (IMPRS) on "Bounded Plasmas." We are thankful to Axel Knuth and Henrik Kotzan for the help in building up the experimental setup. Thanks to Professor Debabrata Ghose and Professor T. K. Chini, Saha Institute of Nuclear Physics, Kolkata, India, respectively, for AFM and SEM-EDX measurements.

[1] G. Müller, P. P. Deimal, W. Hellmich, and C. Wagner, Thin Solid Films **296**, 157 (1997).
[2] J. M. Blackburn, D. P. Long, A. Cabanas, and J. J. Watkins, Science **294**, 141 (2001).
[3] S. Lai, J. Gou, V. Petrova, G. Ramanath, and L. Allen, Phys. Rev. Lett. **77**, 99 (1996).
[4] R. Kusche, Th. Hippler, M. Schmidt, B. von Issendorff, and H. Haberland, Eur. Phys. J. D **9**, 1 (1999).
[5] T. G. Dietz, M. A. Duncan, D. E. Powers, and R. E. Smalley, J. Chem. Phys. **74**, 6511 (1981).
[6] P. Milani and W. A. de Heer, Rev. Sci. Instrum. **61**, 1835 (1990).
[7] H. R. Siekman, C. Luder, J. Faehrmann, H. O. Lutz, and K. H. Meiwes Broer, Z. Phys. D: At., Mol. Clusters **20**, 417 (1991).
[8] S. G. Hall, M. B. Nielsen, A. W. Robinson, and R. E. Palmer, Rev. Sci. Instrum. **68**, 3335 (1997).
[9] S. H. Baker, S. C. Thornton, K. W. Edmonds, M. J. Maher, C. Norris, and C. Binns, Rev. Sci. Instrum. **71**, 3178 (2000).
[10] I. M. Goldby, B. von Issendorff, L. Kuipers, and R. E. Palmer, Rev. Sci. Instrum. **68**, 3327 (1997).
[11] G. Palasantzas, S. A. Koch, and J. T. M. De Hosson, Rev. Adv. Mater. Sci. **5**, 25 (2003).
[12] S. Pratontep, S. J. Carroll, C. Xirouchaki, M. Streun, and R. E. Palmer, Rev. Sci. Instrum. **76**, 045103 (2005).
[13] S. Yatsuya, T. Kamakura, K. Yamauchi, and K. Mihama, Jpn. J. Appl. Phys., Part 2 **25**, L42 (1986).
[14] H. Hahn and R. S. Averback, J. Appl. Phys. **67**, 1113 (1990).
[15] H. Haberland, M. Karrais, M. Mall, and Y. Thurner, J. Vac. Sci. Technol. A **10**, 3266 (1992).
[16] H. Haberland, *Clusters of Atoms and Molecules* (Springer, New York, 1994).
[17] H. Haberland, B. von Issendorff, J. Yufeng, and T. Kolar, Phys. Rev. Lett. **69**, 3212 (1992).
[18] H. Haberland, M. Mall, M. Mosseler, Y. Qiang, T. Reiners, and Y. Thurner, J. Vac. Sci. Technol. A **12**, 2925 (1994).
[19] S. H. Baker, S. C. Thornton, A. M. Keen, T. I. Preston, C. Norris, K. W. Edmonds, and C. Binns, Rev. Sci. Instrum. **68**, 1853 (1997).
[20] G. Palasantzas, S. A. Koch, and J. Th. M. De Hosson, Appl. Phys. Lett. **81**, 1089 (2002).
[21] T. Vystavel, G. Palasantzas, S. A. Koch, and J. Th. M. De Hosson, Appl. Phys. Lett. **82**, 197 (2003).
[22] S. A. Koch, R. H. te Velde, G. Palasantzas, and J. Th. M. De Hosson, Appl. Phys. Lett. **84**, 556 (2004).
[23] J. T. M. De Hosson, G. Palasantzas, T. Vystavel, and S. A. Koch, "Structural Stability of Nano-Sized Clusters", *Materials Research Society Symposia Proceedings*, (Mater. Res. Soc. Symp. Proc., Warrendale, PA, 2004) Vol. 791, p. Q.8.2.
[24] Quadrupole mass filter—QMF 200, Oxford applied research, version 1.1.
[25] *Atomic and Molecular Beam Methods*, edited by G. Scoles (Oxford University Press, Oxford, 1988), Vol. 1, Chap. 8.
[26] I. Shyjumon, M. Gopinadhan, C. A. Helm, B. M. Smirnov, and R. Hippler, Thin Solid Films **500**, 41 (2006).
[27] A. Majumdar, G. Das, N. Patel, P. Mishra, D. Ghose, and R. Hippler, J. Electrochem. Soc. **155**, D22 (2008).
[28] A. Majumdar, J. Schäfer, P. Mishra, D. Ghose, J. Meichsner, and R. Hippler, Surf. Coat. Technol. **201**, 6437 (2007).
[29] T. A. Witten and I. M. Sander, Phys. Rev. Lett. **47**, 1400 (1981).
[30] P. Meakin, Phys. Rev. A **27**, 604 (1983).
[31] P. Meakin, Phys. Rev. A **27**, 1495 (1983).
[32] M. Sahimi, M. McKarnin, T. Nordahl, and M. Tirrell, Phys. Rev. A **32**, 590 (1985).
[33] P. Jensen, A. L. Barabási, H. Larralde, S. Havlin, and H. E. Stanley, Phys. Rev. B **50**, 15316 (1994).
[34] B. M. Smirnov, Phys. Rep. **188**, 1 (1990).

4.2. The influence of target erosion on the mass spectra of clusters formed in the planar DC magnetron sputtering source

Surface & Coatings Technology 213 (2012) 41–47

Contents lists available at SciVerse ScienceDirect

Surface & Coatings Technology

journal homepage: www.elsevier.com/locate/surfcoat

The influence of target erosion on the mass spectra of clusters formed in the planar DC magnetron sputtering source

M. Ganeva [a,*], A.V. Pipa [b], R. Hippler [a]

[a] Institut für Physik, Ernst-Moritz-Arndt-Universität Greifswald, Felix-Hausdorff-Strasse 6, 17489 Greifswald, Germany
[b] Leibniz Institute for Plasma Science and Technology (INP Greifswald), Felix-Hausdorff-Strasse 2, 17489 Greifswald, Germany

ARTICLE INFO

Article history:
Received 11 June 2012
Accepted in revised form 4 October 2012
Available online 13 October 2012

Keywords:
Magnetron sputtering
Cluster formation
Gas aggregation
Copper
Nanoclusters

ABSTRACT

The present paper reports on target erosion as one of the crucial parameters influencing the cluster size distribution. Size distributions of nanosized Cu clusters produced by a DC magnetron sputtering source during the lifetime of several different targets were monitored using a quadrupole mass filter. It is indicated that, during the target lifetime, cluster size distribution continuously shifts towards larger cluster sizes and becomes broader. After a certain operation time the cluster size distribution changes abruptly and the cluster formation is stopped. This happens much earlier than the point at which the erosion groove depth reaches the target thickness. It is suggested that a change in the mass spectra during the target lifetime is caused by the variation of the free metal atom density in the aggregation region. This may be due to the alteration of the sputtering yield. It is shown that the variation of the mass spectra correlates with the angular dependence of the sputtering yield.

1. Introduction

Magnetron sputtering is a state-of-the-art technique for thin-film deposition and has been used since the early 1970s [1,2]. Since the 1990s, the magnetron has also been used in gas aggregation sources to produce cluster beams [3,4].

Varying the experimental conditions, it is possible to influence the size distribution of the cluster beam produced by the nanocluster source. In the present work we focus on the clusters of the size of about 1–10 nm. Copper clusters of such a size are being used in the production of antibacterial nanocomposites [5] and in catalysis [6,7].

An overview of the cluster production techniques can be found in [8,9]. Typically, the cluster source consists of the vaporization source, where the free atoms are produced, and the beam apparatus, where the cluster formation takes place. Gas aggregation sources can be considered as one of the most flexible beam apparatuses in terms of cluster sizes and cluster material [8]. In comparison to the other vaporization techniques, planar magnetron based cluster sources have a lot of advantages: very efficient sputtering [2], a broad cluster mass range, high deposition rate, high cluster ionization degree, etc. [4,10]. A main disadvantage of this technique is a problematic reliability [11].

Identification of the parameters which influence the cluster formation and which are difficult to control or even out of our control is important for a stable production of cluster beams with a defined size distribution, for the analysis of cluster formation efficiency, and for fundamental studies of the cluster formation processes. For deposition experiments without mass spectrometric analysis of the cluster beam, the stability of the cluster beam can be a crucial question for their resulting reproducibility.

Clusters are formed from free metal particles sputtered from the target. As a consequence, the target surface is continuously eroded during the magnetron operation. In conventional planar magnetrons the deformation occurs highly localized in the region of the electron confinement. This leads to the formation of a narrow and deep erosion groove and a low target material utilization. Since the problem of target utilization is of great importance for the thin film deposition industry, there are a number of solutions aimed at remedying inefficient target utilization. One could mention rotatable magnetrons [12,13], target-hollow magnetrons [14], rectangular magnetrons with full target erosion [15], etc. A more detailed review of magnetron sputtering techniques can be found in [16,17]. Nevertheless, as far as is known to the authors, only conventional magnetrons are used in nanocluster sources. The present work focuses on the conventional planar magnetron with a circular target.

It was reported that the target erosion influences the ion distribution function in the near-cathode region [18] as well as the deposition rate to the substrate [19]. Based on qualitative observations, it was assumed [11] that it also leads to a variation of the cluster size distribution. The aim of the present work is a quantitative investigation of the development of the cluster size distribution with respect to the target age. Special attention was paid to the reproducibility of the observed effect, measured for several magnetron targets. In addition, an attempt was made to infer the variation of the measured mass spectra by considering the cluster formation and sputtering processes.

* Corresponding author. Tel.: +49 3834 864783; fax: +49 3834 864701.
E-mail address: ganeva@physik.uni-greifswald.de (M. Ganeva).

0257-8972/$ – see front matter © 2012 Elsevier B.V. All rights reserved.
http://dx.doi.org/10.1016/j.surfcoat.2012.10.012

2. Experiment

2.1. DC magnetron nanocluster source

In the present work the nanocluster source NC-200 produced by Oxford Applied Research (Fig. 1) was used. It is a gas aggregation source based on the magnetron sputtering. The source contains three sections: magnetron and aggregation chamber, the quadrupole mass filter, and the deposition chamber. The same nanocluster source was used in [20,21].

Three pressure gauges are installed at the positions marked as 1, 2 and 3 in Fig. 1: gauge 1 is attached to the magnetron chamber, gauge 2 to the outer magnetron chamber, and gauge 3 to the deposition chamber. The balanced magnetron (4) is used as a source of the free Cu atoms needed for cluster formation. The magnetron is equipped with a circular Cu target of 2″ diameter and 5 mm thickness. Sputtered atoms proceed through the aggregation chamber (5) together with a buffer gas flow towards the output orifice (6). The walls of the aggregation chamber can be cooled by water or liquid nitrogen. In the present work, forced cooling was not used and the walls were in contact with the ambient air. The length of the aggregation chamber can be controlled using the vacuum spring (double-sided arrow). The road (8) has interface connections for mass flow controllers, water cooling of the magnetron magnets and an electrical power supply (Glassman LV 600-1.7).

The cluster beam enters the mass filter through the orifice (9). For the measurement of cluster size distributions, the commercially available quadrupole mass filter QMF200 (Oxford Applied Research) was used. We implemented one important modification: the internal amperemeter was replaced by a Keithley K6487 femtoamperemeter which was connected directly to the QMF detection plate (11). Such an improvement allows the measurement of cluster ion currents below 10^{-12} A. The quadrupole rods (10) are arranged in pairs and biased with the AC voltage. Varying the amplitude and frequency of this voltage, clusters are selected according to their charge to mass ratio. In the present work, the amplitude of the AC voltage was varied between 1 and 250 V, the frequency of the AC voltage was 4 kHz unless otherwise specified, and the ratio U/V of amplitudes of DC and AC voltages was equal to 0.100. This QMF system is described in greater detail elsewhere [22]. After passing through the quadrupole mass filter, mass-selected clusters proceed to the deposition chamber where they can be deposited to the substrate fixed on the holder (12).

Fig. 2 presents some details of the magnetron source. The target is situated above the magnets fixed using the target holder (not depicted) and acts as a cathode biased with negative voltage. The anode is grounded, as are the chamber walls. The discharge current and voltage are measured at the power supply.

The magnetron magnetic alignment consists of two pieces: a cylinder of 25 mm diameter and ring of 6 mm thickness and 46 mm outer diameter (cutoff is depicted in Fig. 2). The separation between these magnets is 5 mm and their height is 12 mm. The magnets are continuously cooled by the flowing water (Fig. 2).

Such a configuration corresponds to the balanced magnetron. The magnetic field strength measured directly above the target reaches about 160 mT at the maximum point (center of the target) and rapidly decreases with the distance above the target surface. At a distance of 30 mm and higher it is negligibly small.

2.2. Choice and control of the experimental parameters

The aim of this study is to investigate the influence of the target lifetime on the cluster size distribution. Therefore it is important to fix all other experimental parameters and keep them constant during the experiment. The main parameters influencing the cluster size distribution are: discharge power, pressure in the aggregation chamber, temperature of the aggregation chamber walls, and length of the aggregation region.

A stable beam of Cu clusters can be produced without forced cooling of the aggregation chamber walls. To reduce the experiment costs cooling was not applied. The aggregation chamber walls are assumed to be at room temperature because they were in a contact with ambient air.

The Ar gas flow rate (15 sccm)[1] and the diameter of the variable output orifice (3 mm) determine the pressure in the magnetron chamber (18 Pa).[2] Their values and the length of the aggregation region (12 ± 0.2 cm) were selected in order to obtain a cluster size distribution covering the maximum possible range of cluster sizes lying within the working range of the quadrupole mass filter.

The moderate discharge power of ≈ 120 W was chosen to minimize possible instabilities caused by the system heating.

2.3. Target lifetime

Due to the magnetic field configuration, target sputtering is not uniform but leads to the formation of a groove, also called "race-track" (Fig. 2). Non-uniform target sputtering is a common feature of conventional planar magnetrons [2].

It was not possible to measure the depth of the groove in the "race-track" region during the experiment. Opening of the magnetron chamber causes oxidation of the target surface and injection of impurities from the ambient air inside. This can influence the aging process and for this reason was avoided.

In the present work we use the total energy dissipated in the discharge for a quantitative characterization of the target erosion. The correlation between them can be qualitatively inferred as follows.

In the framework of a semi-empirical approach [23], the number of sputtered atoms N_{Cu} is proportional to the sputtering yield Y, discharge operation time t, and the discharge curirent I_d:

$$N_{Cu} \propto Y\ I_d\ t. \tag{1}$$

Assuming that the sputtering yield Y is linearly proportional to the energy of bombarding argon ions E_{Ar^+} (which is a fair approximation for planar targets in the energy range of 200 eV–300 eV) and considering the proportionality of E_{Ar^+} with the discharge voltage U_d [24], we obtain:

$$N_{Cu} \propto U_d\ I_d\ t = P\ t. \tag{2}$$

Thus, the total energy dissipated in the discharge is related to the total number of sputtered atoms or volume of the erosion groove. The target lifetime is entirely defined by the erosion process. So, in the present work we characterize the target lifetime using the total energy dissipated in the discharge. The lifetime measured in kWh (kilowatt hours) is also utilized in [25–27].

3. Results

3.1. Current–voltage characteristics

The principal peculiarity of the magnetron discharge is that the discharge current may be adjusted nearly independent of voltage [1,28]. The empirical current–voltage relationship for magnetron discharges [1,28,29] is:

$$I_d \propto U_d^n\ , \tag{3}$$

where I_d and U_d are discharge current and voltage respectively, and n is a performance index of the electron trap formed by the magnetic field.

[1] 5% accuracy of the flow reading of MKS 247 4 Channel Readout.

[2] Pirani pressure gauges are gas-dependent. The correction coefficient for argon 1.7 (according to the manual) was taken into account.

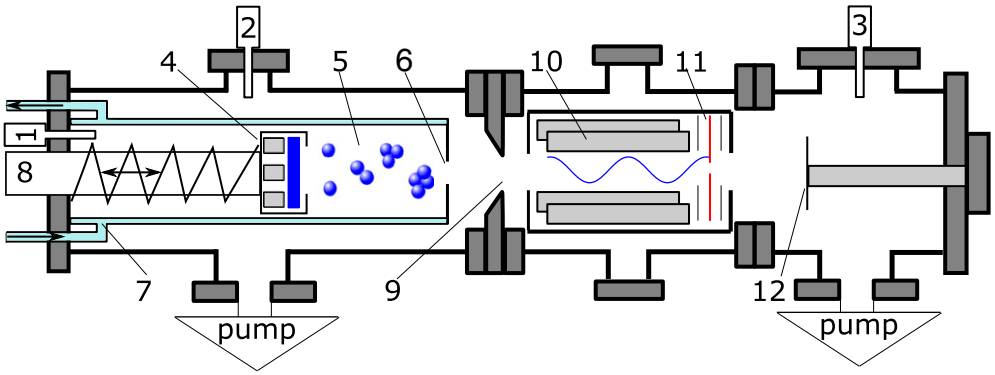

Fig. 1. Schematics of the nanocluster source. 1, 2, 3 — Pressure gauges. Magnetron section: 4 — magnetron, 5 — aggregation region, 6 — variable output orifice, 7 — inlets for cooling of the aggregation chamber walls, 8 — interfaces for connection of Ar, water cooling of the magnetron magnets and power supply; screws for setting the variable orifice diameter and length of the aggregation region, 9 — orifice. Quadrupole Mass Filter (QMF): 10 — quadrupole rods, 11 — detection plate. Deposition chamber: 12 — substrate holder.

Due to the variation of current–voltage characteristics during the target lifetime and for different targets (Figs. 3 and 4), it is important to determine which of the discharge parameters to keep constant. Since small variations of voltage lead to a significant change of current (Eq. (3)), current control should provide better stability in comparison to voltage control.

Fig. 3 displays the measured current–voltage characteristics. Fitting the experimental points with Eq. (3), we obtain $n = 7.55$. The value of the current 0.4 A selected for the experiment (gray dashed line in Fig. 3) is near the lower boundary of magnetron operation for the chosen pressure: below 0.3 A a small change in the current would lead to a significant change in voltage and discharge power. The zoomed inset in Fig. 3 shows details of the relationship between current and voltage for the targets under investigation. Although the discharge current is set with ≈2% accuracy, variation of the discharge voltage for different targets is about 10%.

The points measured with new flat targets are labeled with crosses in Fig. 3. For these points, the influence of target erosion can be excluded. Accuracy of the current control should not have a significant effect: the I-V plot almost resembles a vertical line in this range. Deviations in voltage for new targets seem to be due to difficulties in precise adjustment of the inter-electrode distance. This assumption is based on the fact that the minimal voltage values were obtained for the target mounted with a distance to the anode of ≈0.3 mm. Data points for this target are shown as black squares in Fig. 3.

It is necessary to mention that the Glassman power supply has a fairly low meter accuracy: 7 V for voltage and 0.018 A for current. Therefore, initial voltage variation for new flat targets can be caused not only by an anode positioning error and oxide layer on the target surface (that may have different thicknesses on different targets), but also by the meter accuracy.

In Fig. 4a the discharge voltage is presented as a function of the target lifetime. As one can see, the voltage continuously decreases during the target lifetime. This tendency is very well reproducible for all targets except one with an intentionally increased inter-electrode distance. For a constant discharge current, the discharge power (Fig. 4b) shows the same behavior during the target lifetime as the discharge voltage. As indicated in Fig. 4b, the variation of the discharge power is in the range of 10%.

The stability of the Glassman power supply is quite good: 300 mV for voltage and 0.85 mA for current. Thus the observed voltage variation of about 30 V with target age, is higher than the voltmeter uncertainty.

3.2. Development of the mass spectra with target lifetime

Fig. 5. depicts the dynamics of the mass spectra for the target α during its lifetime. The current–voltage characteristics of the discharge during the lifetime of this target are labeled with open circles in Figs. 3 and 4.

After 0.1 kWh of target lifetime, cluster size distribution continuously shifts towards larger cluster sizes (Fig. 5). Also the cluster size distribution becomes broader. This process continues until the lifetime of 0.7 kWh is reached. Between 0.7 kWh and 0.8 kWh the cluster size distribution abruptly changes (see black solid line in Fig. 5): clusters become much smaller and their intensity decreases. After a longer source operation of more than 1.2 kWh of target lifetime the cluster ion signal disappears completely.

Hence, in order to obtain clusters, we have to change the target already after 1.2 kWh of its lifetime, i.e. at an erosion groove depth of ≈3.8 mm. Usually we do this immediately after an abrupt change of the mass spectra, i.e. after 0.8 kWh; this corresponds to an erosion

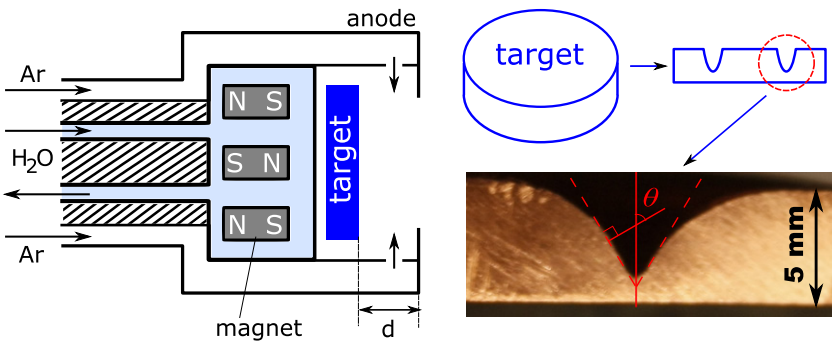

Fig. 2. Schematics of the magnetron. A circular Cu target of 2″ in diameter is situated above the water-cooled magnets. d — is a distance between the cathode (target) biased by the negative DC voltage and a grounded anode. Typically, we keep $d = 0.3$ mm. The photo shows a magnified cutoff of the race-track profile. Dashed lines on the photo correspond to $\theta = 60°$.

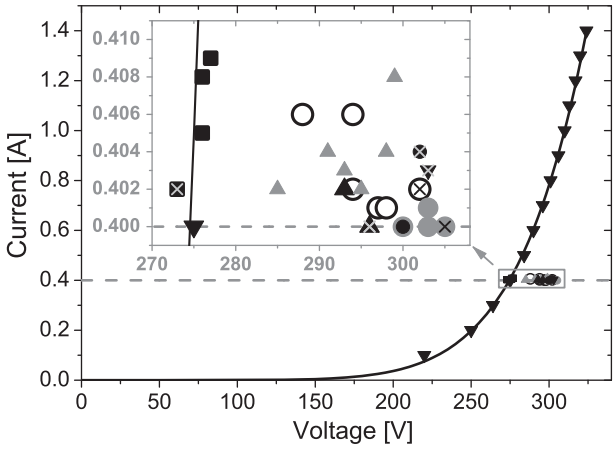

Fig. 3. Measured current–voltage characteristics of the magnetron discharge. Solid line is a fit to the experimental data by Eq. (3). The gray dashed line indicates the selected current value 0.4 A. Points represent the measured current and voltage values for targets under investigation (different symbols correspond to the different targets). The inset shows those data in detail. Filled black squares are the data points measured for the target at nearly twice the cathode–anode distance. Crosses label the measurements with new flat targets.

groove depth of ≈3 mm. The photo of the target profile in Fig. 2 indicates that the target is not yet sputtered completely. The end of the target lifetime calculated using the online calculator provided by Gencoa Ltd. [25] is for our experimental conditions 3.2 kWh. Thus, it can be concluded that the end of the target lifetime with respect to the cluster formation is significantly shorter than with respect to atomic film deposition.

Fig. 5 shows that the cluster size distribution changes continuously. During the recording of the mass spectra the experimental conditions were kept constant. Thus irreversible changes are most probably caused by target erosion. No stabilization of the mass spectrum was observed. Therefore, in order to have well-defined conditions for the formation of a cluster beam, the experiment should be so fast that no significant changes occur and the target lifetime should be monitored.

3.3. Reproducibility

It is reasonable to examine whether the shift of mass spectra in time is reproducible for measurements with different targets. For this purpose the measured mass spectra for seven different copper targets are grouped according to their lifetime ranges and presented in Fig. 6. All mass spectra except one (marked γ^* which was taken at 5 kHz) were measured at the QMF frequency of 4 kHz to avoid any change of frequency influencing the intensity of cluster ions. In

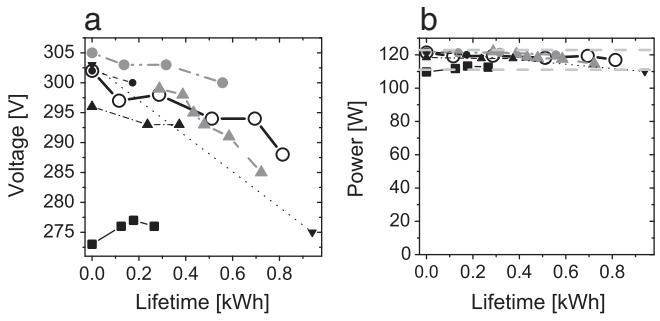

Fig. 4. Discharge voltage (a, left) and discharge power (b, right) *versus* target lifetime at a constant discharge current. ■: measurements with a cathode–anode distance of $d \approx 0.5$ mm; other symbols: measurements with $d \approx 0.3$ mm.

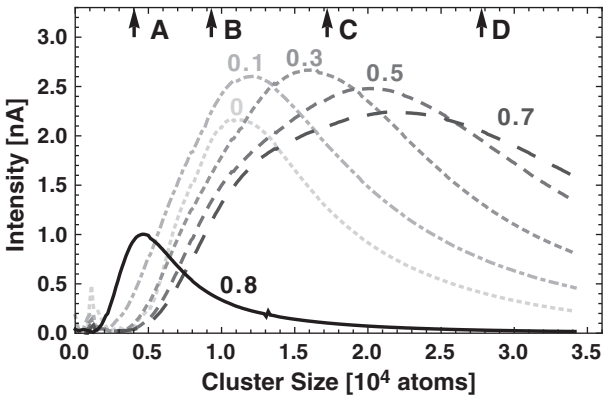

Fig. 5. Mass spectra for the target α measured at different target lifetimes: 0 kWh, 0.1 kWh, 0.3 kWh, 0.5 kWh, 0.7 kWh and 0.8 kWh. Arrows and labels "A, B, C, D" are markers of the cluster sizes selected for further analysis.

between the measurements the targets were operated also in other experimental conditions.

The mass spectra for new flat targets (lifetime 0 kWh) are presented in Fig. 6a. The large difference between the cluster size distributions for different targets (α, β, γ, δ and) is probably caused by different oxide layers on the target surface or by a variation of the inter-electrode distance.

Fig. 6b shows the mass spectra measured at the target lifetime of 0.12 ± 0.05 kWh: α 0.12 kWh, β 0.17 kWh, γ^* 0.07 kWh, and δ 0.12 kWh. Some minor differences are noted; they are significantly reduced in comparison to the zero lifetime measurements. Apparently, sputtering of the oxide layer — cleaning of the target surface in plasma — results in a better quantitative agreement for mass spectra measurements with different targets.

Fig. 6c shows the collected cluster size distributions measured at the lifetime of 0.65 ± 0.05 kWh: α 0.70 kWh, γ 0.70 kWh, ζ 0.61 kWh, and ω 0.61 kWh. In comparison with the previous figure, a shift of the cluster size distribution towards larger cluster sizes is noted. In addition, the cluster size distribution for all targets becomes broader.

Fig. 6d presents mass spectra measured at the lifetime of $0.75 \pm$ 0.07 kWh for targets: α 0.81 kWh, ζ 0.72 kWh, and ω 0.68 kWh. This figure indicates that an abrupt change of the mass spectra at a target lifetime of $\approx 0.7 - 0.8$ kWh is well reproducible.

Other researchers also noted a change of the mass spectra during the target lifetime (private communications). In the present work it is indicated that the variations in the mass spectra are qualitatively similar for all targets considered. Quantitative differences may be explained by the precision of control of the experimental parameters or different operation conditions for targets between the points measured.

3.4. Behavior of different cluster sizes

In order to estimate the typical time of the mass spectrum shift during long-time experiments, it is convenient to examine the development of the cluster intensity with the target lifetime for a given cluster size. Several cluster sizes (marked with arrows A, B, C and D in Fig. 5) were selected for monitoring. The result is presented in Fig. 7: A: 4×10^3 atoms, B: 9×10^3 atoms, C: 17×10^3 atoms, and D: 28×10^3 atoms. Different symbols represent measurements with different targets.

The intensity of small clusters consisting of about 4×10^3 atoms (Fig. 7A) slightly increases during the beginning of the target lifetime. After 0.3 kWh, clusters of this size almost disappear and only after an abrupt change of the cluster size distribution at about 0.6 kWh can we detect them again. The number of clusters of the size of approximately 9×10^3 atoms (Fig. 7B) reaches its maximum at 0.1–0.2 kWh, after which the intensity continuously decreases, almost vanishing at

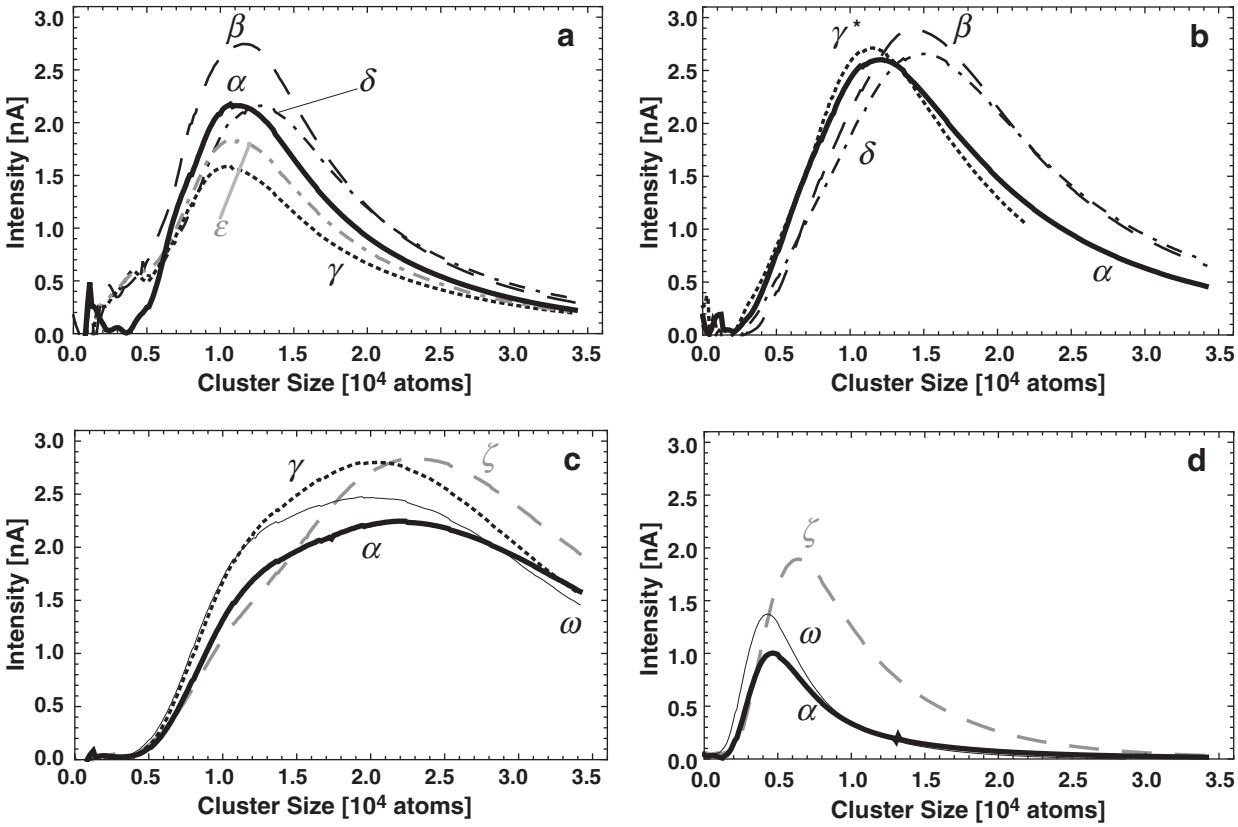

Fig. 6. Variation of mass spectra during the target lifetime measured for different targets (indicated by different line types and symbols). a: lifetime 0 kWh. b: 0.12 ± 0.05 kWh, c: 0.65 ± 0.05 kWh, and d: 0.75 ± 0.07 kWh.

0.8 kWh. The intensity of larger clusters of the size of about 1.7×10^4 atoms (Fig. 7C) slowly increases until 0.2 kWh. Between 0.2 and 0.6 kWh the intensity is fairly stable (within a 10% variation for all targets except δ), and after that rapidly decreases to almost zero. The intensity of the largest clusters with a size of approximately 2.8×10^4 atoms (Fig. 7D) continuously increases until 0.6–0.7 kWh and then rapidly decreases at 0.7–0.8 kWh.

The intensity of mass-selected clusters varies in its behavior for different cluster sizes during the target lifetime. Fig. 7 shows, that clusters of the size 1.7×10^4 atoms have the most stable production in the experimental conditions considered. This size is in the middle of the mass detection region for which the experimental conditions were optimized. Probably the size of mostly stable clusters produced may be influenced by varying the experimental parameters affecting the residence time of clusters in the aggregation chamber.

Nevertheless, during the lifetime of 0.1 kWh, which corresponds to 1 h of experiment duration at a discharge power 100 W, the number of clusters with smaller or larger than optimal sizes can change significantly. This observation is especially important for the deposition experiments without preliminary mass spectrometric analysis of the cluster beam (such as [30,31]). In addition, for the experiments with mass spectrometric studies of the dependence of the cluster size distribution on different experimental conditions such as buffer gas content, pressure, electrical parameters, etc. (for example [22,32–36]) the variation of the mass spectra caused bytarget erosion has to be considered.

4. Discussion

4.1. Target erosion and cluster formation

Cluster formation is governed by three main processes: atom adhesion, coagulation (kinetic and diffusion modes), and coalescence [37]. The density of free metal atoms influences the cluster density in the case of adhesion and the average cluster size in other cases. Currently we do not know which of those processes dominates in our case. The recent work [24] assumes that atom adhesion dominates. The cluster size distribution function derived within that model decreases monotonically with cluster size and, hence, significantly differs from the experimental distribution which shows a clear maximum at a particular cluster mass (see Figs. 5 and 6).

Nevertheless, apart from the particular cluster formation process or the combination of cluster formation processes, it is possible to assert that the density of free metal atoms essentially influences the cluster formation. The number of free metal atoms sputtered from the target per unit time is proportional to the sputtering yield (Eq. (1)). Thus, in the present work, we assume that the change in the cluster size distribution is caused by a variation of the sputtering yield. For example, this change can be related to a dependency of the sputtering yield on the incident angle of impinging Ar^+ ions. A simulation performed by Goeckner et al. [38] indicates that for a flat new target Ar^+ ions strike the cathode surface almost perpendicularly. If we assume that the incidence angle of impinging Ar^+ ions increases with target erosion, then the sputtering yield will follow the variation of the incidence angle during the target lifetime. The angular dependency of the sputtering yield will be discussed below.

4.2. Angular dependency of sputtering yield

According to a simulation performed by Goeckner et al. [38], a large fraction of ions hits the cathode with full energy. For simplicity we assume that all of the impinging Ar^+ ions have a kinetic energy of 300 eV. Such a simplification will not impair our qualitative estimations because the sputtering yield depends monotonously on the

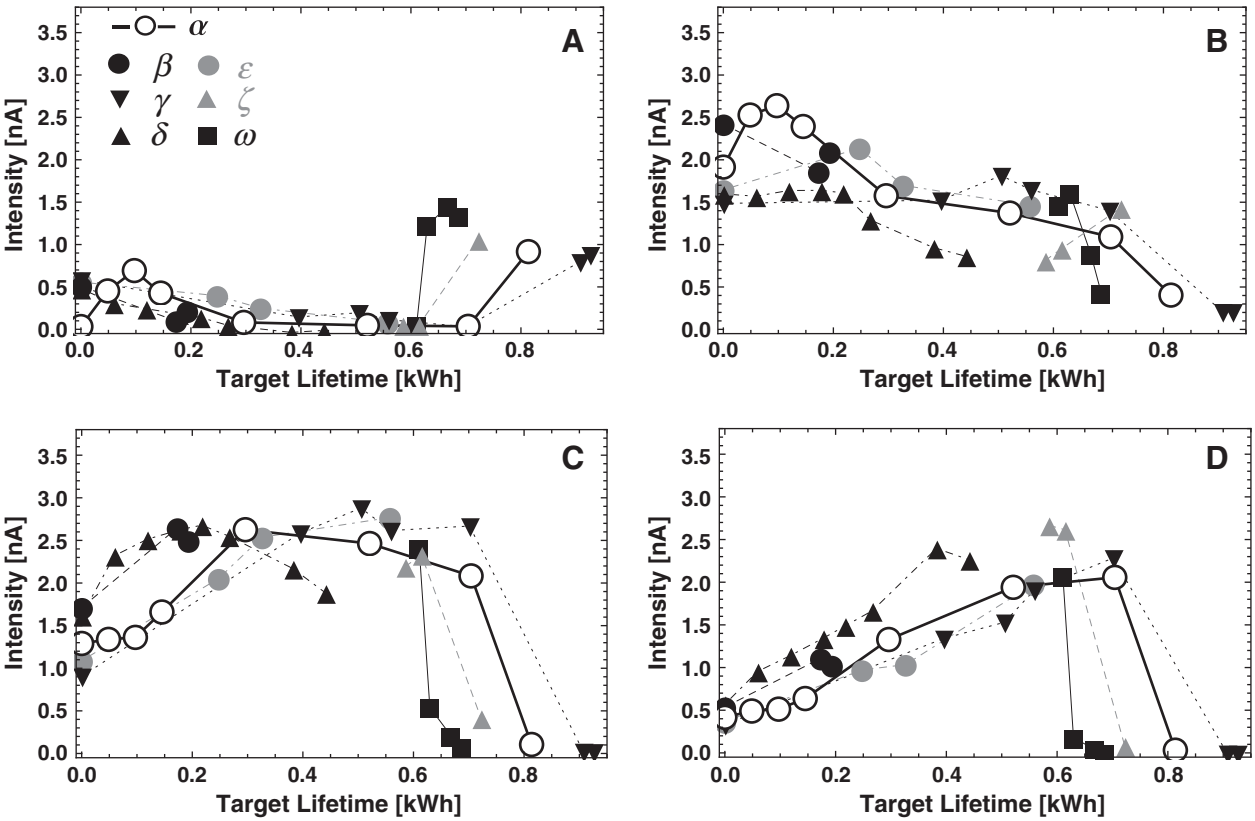

Fig. 7. Intensity of mass-selected clusters vs. target lifetime. Cluster size A: 4×10^3 atoms, B: 9×10^3 atoms, C: 1.7×10^4 atoms, and D: 2.8×10^4 atoms. Different symbols represent measurements with different targets.

incident ion energy for the energy range and materials under consideration here [39–41].

Fig. 8 displays the angular dependency of the sputtering yield. The black curve is calculated by employing the semi-empirical approach of Yamamura [42] making use of expressions for coefficients and their values given elsewhere [43–45]. The gray points are the data provided in data tables [41]. They are calculated using the Monte Carlo program TRIM.SP. In spite of the quantitative difference, both approaches show a similar tendency: while the incident angle is small, the sputtering yield increases with increasing incident angle. After passing a maximum value, sputtering yield decreases with increasing incident angle dropping to zero near the grazing incidence. Processes underlying the angular dependence of the sputtering yield are reviewed in [46].

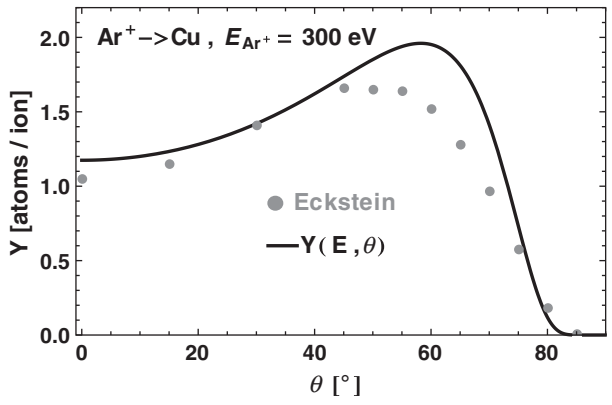

Fig. 8. Angular dependence of sputtering yield. Energy of incident Ar^+ ions is 300 eV. The black curve is calculated in the present work using the Yamamura approach [42]. The gray points are from data tables [41].

We believe that the observed variation of the mass spectra with target lifetime (Fig. 5) correlates with the angular dependence of the sputtering yield. In the beginning the target is flat and the incidence angle of the bombarding ions is normal ($\theta=0°$). The erosion modifies the surface and if the trajectory of ions does not change, the incident angle θ increases. A small increase of θ leads to an increasing sputtering yield (Fig. 8), and thus to higher numbers of free metal atoms. This should either result in a larger number of clusters or the formation of larger clusters [37]. An increasing intensity of larger clusters in the beginning of the target lifetime is clearly seen in Fig. 7C and D. A shift of the most probable cluster mass in Figs. 5 and 6 also indicated the production of larger clusters. When the incident angle reaches a critical value ($\approx60°$), a small increase of the incidence angle leads to a strong reduction of the sputtering yield and consequently to a reduction either of the cluster intensity or their size or both. An abrupt decrease of the cluster intensity and mass of all clusters is observed in the experiment after the critical lifetime is reached (Figs. 5–7). The angle of the erosion groove shown in Fig. 2 with dashed lines corresponds to $\theta=60°$.

In spite of a fair correlation between the angular dependency of the sputtering yield and the time evolution of the mass spectra, the present approach also has its drawbacks:

- The angular dependency of the sputtering yield obtained for a flat cathode is used. The applicability of this data for the present condition is open to discussion. For example, in the case of rough surfaces the angular dependency of the sputtering yield is less pronounced [41].
- The real erosion profile was not considered in the calculation of the angular dependency of the sputtering yield.

- The anisotropy of the spatial distribution of sputtered atoms and their re-deposition were not considered. The angular distributions of ejected atoms depend on the incidence angle of the Ar^+ ions [47].
- A description of the target erosion using the current lifetime definition also requires an additional analysis. Currently, only the discharge power and operation time are considered. However, the erosion profile also depends on the operating pressure [48,49].

5. Conclusions

The results presented show that target lifetime has an essential influence on the cluster size distribution; this cannot be neglected in cases where stable cluster beams of well-defined size distribution are required. It was indicated that the cluster formation stops considerably earlier than the completion of target sputtering, i.e. when the depth of the erosion groove reaches the target thickness. We suggest that the main reason for such an influence is a variation of the sputtering yield with angle of ion incidence which affects the density of the free metal atoms: the sputtering decreases rapidly once a certain incidence angle is reached. A more detailed theoretical analysis is yet required to fully understand the underlying processes.

Acknowledgments

This work was supported by the Deutsche Forschungsgemeinschaft (DFG) through SFB-TR24 *Fundamentals of Complex Plasmas*. Helpful discussions with Prof. Boris Smirnov, Dr. Pavel Kashtanov, and Dr. Vítězslav Straňák and the technical support of Axel Knuth, Robert Mrotzek, and Michael Beck are gratefully acknowledged.

References

[1] J.A. Thornton, A.S. Penfold, in: J.L. Vossen, W. Kern (Eds.), Thin Film Processes, 24–28, Academic Press, Inc., Oval Road, London NW1 7DX, 1978, p. 75.
[2] R.K. Waits, in: J.L. Vossen, W. Kern (Eds.), Thin Film Processes, 24–28, Academic Press, Inc., Oval Road, London NW1 7DX, 1978, p. 131.
[3] V.N. Popok, I. Barke, E.E. Campbell, K.-H. Meiwes-Broer, Surf. Sci. Rep. 66 (2011) 347.
[4] H. Haberland, M. Karrais, M. Mall, Y. Thurner, J. Vac. Sci. Technol. A 10 (1992) 3266.
[5] N. Cioffi, L. Torsi, N. Ditaranto, G. Tantillo, L. Ghibelli, L. Sabbatini, T. Bleve-Zacheo, M. D'Alessio, P.G. Zambonin, E. Traversa, Chem. Mater. 17 (2005) 5255.
[6] T. Ressler, B.L. Kniep, I. Kasatkin, R. Schlögl, Angew. Chem. Int. Ed. 44 (2005) 4704.
[7] S. Vukojevic, O. Trapp, J.-D. Grunwaldt, C. Kiener, F. Schüth, Angew. Chem. Int. Ed. 44 (2005) 7978.
[8] P. Milani, S. Iannotta, Cluster Beam Synthesis of Nanostructured Materials, Springer, 1999.
[9] In: H. Haberland (Ed.), Clusters of Atoms and Molecules I, Springer Verlag, Berlin Heidelberg, 1995.
[10] H. Haberland, M. Mall, M. Moseler, Y. Qiang, T. Reiners, Y. Thurner, J. Vac. Sci. Technol. A 12 (1994) 2925.
[11] S. Pratontep, S.J. Carroll, C. Xirouchaki, M. Streun, R.E. Palmer, Rev. Sci. Instrum. 76 (2005) 045103.
[12] R. De Gryse, D. Depla, S. Mahieu, J. Haemers, Mater. Technol. Adv. Perform. Mater. 26 (2011) 3.
[13] R.D. Gryse, J. Haemers, W. Leroy, D. Depla, Thin Solid Films 520 (2012) 5833.
[14] R. Kukla, T. Krug, R. Ludwig, K. Wilmes, Vacuum 41 (1990) 1968.
[15] C.B. Garrett, 1984. US Patent No 4 444 643.
[16] J. Musil, J. Vlcek, P. Baroch, in: Y. Pauleau (Ed.), Materials Surface Processing by Directed Energy Techniques, Elsevier, 2006, p. 67.
[17] G. Bräuer, B. Szyszka, M. Vergöhl, R. Bandorf, Vacuum 84 (2010) 1354.
[18] T. Welzel, K. Ellmer, Surf. Coat. Technol. 205 (Supplement 2) (2011) S294.
[19] B. Chapman, Glow Discharge Processes, Sputtering and Plasma Etching, John Wiley and Sons, Inc., 1980.
[20] I. Shyjumon, M. Gopinadhan, O. Ivanova, M. Quaas, H. Wulff, C.A. Helm, R. Hippler, Eur. Phys. J. D 37 (2006) 409.
[21] I. Shyjumon, M. Gopinadhan, C.A. Helm, B.M. Smirnov, R. Hippler, Thin Solid Films 500 (2006) 41.
[22] M. Ganeva, T. Peter, S. Bornholdt, H. Kersten, T. Strunskus, V. Zaporojtchenko, F. Faupel, R. Hippler, Contributions to Plasma Physics, 2012.
[23] M. Wolter, H.T. Do, H. Steffen, R. Hippler, J. Phys. D: Appl. Phys. 38 (2005) 2390.
[24] P.V. Kashtanov, B.M. Smirnov, R. Hippler, Physics-Uspekhi 50 (2007) 455.
[25] Gencoa Ltd., Gencoa sputter rate calculator (calc.gencoa.co.uk), 2006.
[26] G.B. Crumley, R.E. Demaray, 1987. European Patent EP0297779 — Magnetron sputtering targets.
[27] M. Abburi, S. Ramaswami, 2002. US Patent No 6 436 207.
[28] J.A. Thornton, Thin Solid Films 80 (1981) 1.
[29] S.M. Rossnagel, H.R. Kaufman, J. Vac. Sci. Technol. A 6 (1988) 223.
[30] T. Peter, M. Wegner, V. Zaporojtchenko, T. Strunskus, S. Bornholdt, H. Kersten, F. Faupel, Surf. Coat. Technol. 205 (2011) S38.
[31] P. Solar, O. Polonskyi, A. Choukourov, A. Artemenko, J. Hanus, H. Biederman, D. Slavinska, Surf. Coat. Technol. 205 (2011) S42.
[32] V. Stranak, S. Block, S. Drache, Z. Hubicka, C.A. Helm, L. Jastrabik, M. Tichy, R. Hippler, Surf. Coat. Technol. 205 (2011) 2755.
[33] A. Marek, J. Valter, S. Kadlec, J. Vyskocil, Surf. Coat. Technol. 205 (2011) S573.
[34] M. Gracia-Pinilla, E. Martínez, G. Vidaurri, E. Pérez-Tijerina, Nanoscale Res. Lett. 5 (2010) 180.
[35] A. Banerjee, R. Krishna, B. Das, Appl. Phys. A Mater. Sci. Process. 90 (2008) 299.
[36] O. Kamalou, J. Rangama, J.-M. Ramillon, P. Guinement, B.A. Huber, Rev. Sci. Instrum. 79 (2008) 063301.
[37] B.M. Smirnov, Physics-Uspekhi 54 (2011) 691.
[38] M.J. Goeckner, J.A. Goree, J. Sheridan, E. Terrence, IEEE Trans. Plasma Sci. 19 (1991) 301.
[39] N. Matsunami, Y. Yamamura, Y. Itikawa, N. Itoh, Y. Kazumata, S. Miyagawa, K. Morita, R. Shimizu, Radiat. Eff. 57 (1981) 15.
[40] Y. Yamamura, N. Matsunami, N. Itoh, Radiat. Eff. 71 (1983) 65.
[41] W. Eckstein, Calculated Sputtering, Reflection and Range Values, Technical Report 9/132, IPP, 2002.
[42] Y. Yamamura, S. Shindo, Radiat. Eff. 80 (1984) 57.
[43] M.P. Seah, C.A. Clifford, F.M. Green, I.S. Gilmore, Surf. Interface Anal. 37 (2005) 444.
[44] Y. Yamamura, H. Tawara, At. Data Nucl. Data Tables 62 (1996) 149.
[45] J. Lindhard, M. Scharff, Phys. Rev. 124 (1961) 128.
[46] T. Ono, T. Kenmotsu, T. Muramoto, in: D. Depla, S. Mahieu (Eds.), volume 109 of *Springer Series in Materials Science*, Springer, Berlin Heidelberg, 2008, p. 1.
[47] M. Stepanova, S.K. Dew, J. Vac. Sci. Technol. A 19 (2001) 2805.
[48] T. Fukami, F. Shintani, M. Naoe, Thin Solid Films 151 (1987) 373.
[49] T. Fukami, T. Sakuma, Jpn. J. Appl. Phys. 21 (1982) 1680.

4.3. Mass Spectrometric Investigations of Nano-Size Cluster Ions Produced by High Pressure Magnetron Sputtering

Contrib. Plasma Phys. **52**, No. 10, 881 – 889 (2012) / **DOI** 10.1002/ctpp.201200046

Mass Spectrometric Investigations of Nano-Size Cluster Ions Produced by High Pressure Magnetron Sputtering

M. Ganeva[1]*, **T. Peter**[2], **S. Bornholdt**[3], **H. Kersten**[3], **T. Strunskus**[2], **V. Zaporojtchenko**[2], **F. Faupel**[2], and **R. Hippler**[1]

[1] Institute of Physics, Ernst-Moritz-Arndt University Greifswald, Felix-Hausdorff-Str. 6, D-17487 Greifswald, Germany

[2] Faculty of Engineering, Institute for Materials Science, Multicomponent Materials, Christian Albrechts University of Kiel, Kaiserstr. 2, D-24143 Kiel, Germany

[3] Institute of Experimental and Applied Physics, Plasma Technology, Christian Albrechts University of Kiel, Leibnitzstr. 11–19, D-24098 Kiel, Germany

Received 22 May 2012, revised 13 June 2012, accepted 13 June 2012
Published online 08 November 2012

Key words Ag nanoparticles, magnetron sputtering, Ag cluster films, quadrupole mass filter, TEM

A comparison of quadrupole mass spectrometric (QMS) and transmission electron microscopic (TEM) characterization of silver nano-cluster deposition produced by a nano-cluster source consisting of a planar DC magnetron sputter source in a high pressure gas aggregation chamber is presented and discussed. Cluster sizes and size distributions detected by the two different techniques are compared and the differences are discussed. The effects of He to Ar ratio, gas flow and magnetron power on the cluster size distribution are evaluated. The influence of the target erosion and aging effects are mentioned, too.

1 Introduction

Synthesis of nanocomposite thin films containing nano-sized clusters gained a lot of interest [1, 2]. For technological applications it is important to understand the fundamental processes underlying the cluster formation and growth. The film morphology and properties strongly depend on the size and shape of the "building blocks" — i.e., the clusters. Also the morphology of the nanoclusters often strongly influences optical and electronic properties of the nanocomposite films [3]. Certain metals, especially silver, are known to have also "biological" properties, e.g., antimicrobial behaviour [4]. The size of silver nanoparticles is a very important parameter that influences the interaction with cells like bacteria [5, 6], e.g., silver nanoparticles mainly in the range of 1–10 nm exhibit strongest bactericidal properties [7]. However, many technological applications require a good control of parameters such as metal filling factor, particle size distribution, and also composition of the particles [8]. Hence, it important to control the size of the deposited clusters for tailoring nanocomposite materials with desired properties. This often makes plasmas as the tool of choice, because plasma deposition offers a good control and stability of the film formation process.

The analysis of the clusters deposited on the surface is a straightforward way to obtain a cluster size distribution. Atomic force microscopy (AFM) and transmission electron microscopy (TEM) are powerful techniques for imaging nanoparticles and also for the characterization of their structure [9–12]. However, it is known that determination of cluster sizes by electron microscopy can be misleading, because surface processes like diffusion or even agglomeration of clusters may change the cluster size distribution at the substrate, which distorts the original cluster size distribution produced by the source. The problem is especially serious for silver [13]. Therefore, it is very important to determine the size distribution of the cluster beam in situ in the gas phase.

A magnetron discharge in combination with a gas aggregation region constitutes a complex plasma in which nano-particles can form and grow to larger sizes [1]. Previous studies report the preparation of nanocomposite

* Corresponding author. E-mail: ganeva@physik.uni-greifswald.de, Phone: +49 3834 864783, Fax: +49 3834 864701

films employing a high pressure magnetron sputtering source [14–16]. Simulations of complex plasma-driven nanocomposite formation were recently reported [17]. In the present study we focus on measuring the size distribution of the cluster beam produced by the DC magnetron sputtering source using a quadrupole mass filter (QMF) [9,10]. We investigate the influence of different experimental parameters such as gas pressure (determined by Ar flow rate), discharge power and He:Ar ratio on the cluster size distribution. We also compare the cluster size distributions measured using the QMF with ones obtained by TEM imaging of deposited cluster films.

2 Experiment

2.1 DC Magnetron nanocluster source

For the particle generation and deposition a home build cluster source consisting of a DC magnetron in an aggregation chamber was used. As sputtering source (Fig. 1) a balanced magnetron (Thin Film Consulting ION'X 2UHV) was used. It was connected to a DC power supply (Advanced Energy, MDX 500). Silver was sputtered from a 2 inch target with sputtering powers ranging from 50 to 120 W. A mixture of Ar and He was employed as working gas and the pressure was varied from 50 to 200 Pa, while the He partial pressure was varied between 0 and 30 Pa with gas flow rates between 20 and 110 sccm for Ar and 30 to 100 sccm for He. The working gas conditions were controlled and monitored by a two channel flux controller system (MKS Multi Gas Controller, 647C and 2 MKS Mass-Flow Controllers). The sputtered silver atoms form nanoclusters while following in the buffer gas stream through an orifice to the main chamber. The length of the aggregation chamber from target to aperture was 18 cm and the diameter of the aperture 3 mm. After passing the aperture the nanoclusters form a focused beam that travels through the main vacuum chamber. The chamber was kept at a pressure in the range of 0.1 to 1 Pa, so the cluster beam can expand on its path through the chamber until the clusters are deposited on a wall or a substrate, respectively.

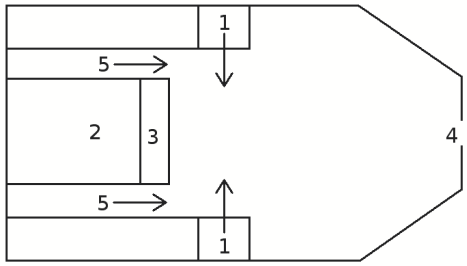

Fig. 1 Schematic design of the cluster source as sectional drawing: 1 — He gas inlet ring, 2 — Magnetron cathode with water cooling, 3 — Ag target mounted on the magnetron cathode, 4 — Orifice, 5 — Gas line for Ar

2.2 Quadrupole Mass Filter

To measure the size distribution of the generated clusters in the beam a quadrupole mass filter QMF200 (Oxford Applied Research) was used (see Fig. 2). It allows the detection of particles up to masses of 3×10^6 amu [19].

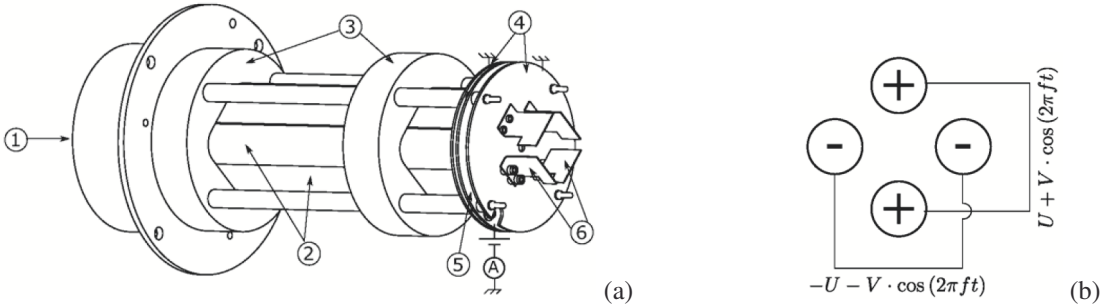

Fig. 2 Quadrupole mass spectrometer QMF-200: (a) schematics of the QMF-200, where 1 – cluster injection, 2 – quadrupole rods, 3 – dielectric isolation, 4 – grounded plates, 5 – ion detector plate, 6 – deflection plates; (b) front view of the quadrupole rods.

The QMF consists of 4 rods, which are arranged in pairs and biased with AC voltage $\pm(U + V \cdot \cos 2\pi f t)$, where f is the frequency. The mass M of particles reaching the detector plate is determined by the expression [19]

$$M = 7 \cdot 10^7 \cdot \frac{kV}{f^2 d^2} \ , \tag{1}$$

where d is the diameter of the quadrupole rods and $k = 1.30$ is a correction factor provided by the manufacturer [19].

The ratio of the amplitudes of DC (U) and AC (V) components of voltage applied to the quadrupole rods defines the resolution, e.g., the width of mass band transmitted through the filter [18, 19]:

$$\frac{\Delta M}{M} = 7.936 \left(0.16784 - \frac{U}{V}\right) \tag{2}$$

To avoid the mass discrimination due to the resolution variation [20] we keep the ratio U/V constant. Current measurements were carried out at $U/V = 0.1$, so the resolution is $\Delta M/M = 0.54$.

To improve the accuracy of the measurements and to reduce noise due to the resolution limits of AD and DA converters, the embedded ampere meter was replaced by a Keithley 6487 femtoamperemeter. The QMF control software was modified to read the cluster ion current directly from the femtoamperemeter. This modification allows the measurement of cluster ion currents below 10^{-12} A.

During processing of the mass spectra we consider following points of the distribution function (Fig. 3): point of the maximum intensity and cluster sizes at the half-maximum points. The first marker allows us to get information about the most probable cluster size and amount of clusters of such size. The second one allows us to estimate the width of the cluster size distribution.

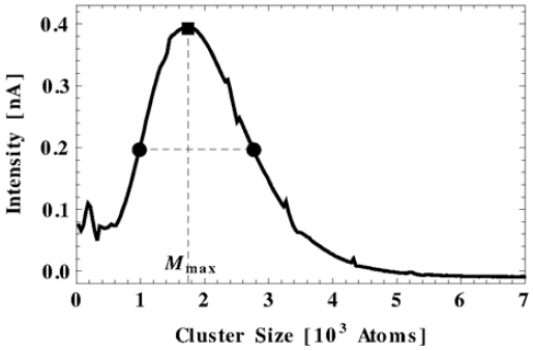

Fig. 3 Typical cluster size distribution (solid line). The black square indicates the point of maximum intensity. Black circles are the half-maximum points.

2.3 Deposition of Ag cluster films

In the present work we have investigated not only the cluster beam itself, but also the clusters deposited on the surface. For this purpose, nanocluster samples deposited on carbon coated copper grids were investigated by TEM (Phillips, Tecnai F 30 G2) to obtain information about their morphology and size distribution. For these measurements the cluster source was covered by a shutter to shield the samples while sputtering and aggregation processes in the cluster source reached stable conditions. After 2 minutes the shutter was opened very briefly (< 1 s) to deposit a fraction of a monolayer of nanoclusters. Single clusters were easily distinguishable in the TEM image. For samples deposited using the QMF the same procedure was used, but because of the long distance between cluster source and substrate a longer deposition time was needed in order to deposit the desired amount of silver nanoclusters.

3 Results and Discussion

3.1 Cluster ion intensity

Based on the analysis of the cluster charging processes [1, 21], it is assumed that most of the clusters are neutral or singly charged under the present experimental conditions.

During the measurements a rather low cluster ion current was observed at the QMF detector. At the same time the QMF rods were contaminated very quickly by a thick layer of deposited silver particles (already after a few hours of operation). We consider two reasons for this unexpected result. The first one is that under the present experimental conditions the source produces mostly neutral particles. It seems to be reasonable: neutral particles hitting the QMF detector do not influence the measured current and their trajectories are independent of the electric field of the QMF, so they move with the gas flow. According to [22], the average transverse cluster velocity is reciprocally proportional to the square root of the cluster mass. Smaller particles thus have a larger scattering angle and could be deposited on the quadrupole rods. Applying the model [21] to our experimental conditions ($T = 300$ K, average cluster radius $r_0 \approx 2.5$ nm) with taking into account electron N_e and Ar^+ ion N_i densities measured by [23], we obtain:

$$\frac{N_-}{N_0} = 0.046, \text{ and } \frac{N_+}{N_0} = 0.04. \tag{3}$$

N_+, N_-, N_0 are the densities of the positive, negative and neutral clusters respectively. Thus, according to the model [21] most of the clusters are neutral.

However this suggestion contradicts to results obtained previously by Haberland [13, 24, 25] who claims that one of the important features of the magnetron based gas aggregation sources is a high percentage (20%–80%) of charged clusters. This was confirmed by Polonskyi et. al. [14]. They observed, that for magnetron current of 0.2 A and the working pressure of 75 Pa about 40% of silver clusters are neutral, 32% are positive and 28% are negative. Using the model [1] and the values of T_e and T_i, electron and ion temperatures respectively, from [23], we obtain for our experimental conditions:

$$\frac{N_-}{N_0} = 0.55, \text{ and } \frac{N_+}{N_0} = 0.72. \tag{4}$$

Thus, according to this model 44% of clusters are neutral, 32% of clusters are positive and 24% of clusters are negative. These values are in good agreement to the observations of Polonskyi et. al. [14].

Depending on the experimental conditions, both, positively and negatively charged clusters were observed in the present work. By biasing the QMF detector it is possible to measure positive and negative clusters separately. The ratio I_+/I_- of intensities of the positive and negative charged clusters yielded in this work is in the range of 0.2 to 1.5 depending on the experimental conditions and the cluster size. Assuming that clusters of the same size have also comparable velocities gives

$$\frac{N_+}{N_-} \approx \frac{I_+}{I_-} = 0.2...1.5. \tag{5}$$

The second possible reason for the low current at the QMF detector is that ions which have a mass to charge ratio m/z outside the quadrupole stability region will have unstable trajectories and crash into the electrodes [20]. This effect is demonstrated by simulation of the ion trajectory by Campana [26]. It is also important that the oscillation amplitude of the ions with stable trajectories is smaller than the distance between the field axis and the electrodes. Otherwise the ion will be lost at the quadrupole rods [20].

Fig. 4 shows the cluster size distributions obtained from TEM analysis of deposited clusters (gray histogram) and from QMF (black solid line). For the evaluation of the cluster diameter from the cluster mass obtained by the QMF measurements, liquid drop model [27] was used. According to this model, the cluster diameter d can be obtained using the following expression:

$$d = 2\, r_w \sqrt[3]{N}\,, \tag{6}$$

where d is the cluster diameter (in nm), r_w is the Wigner-Seitz radius (for Silver $r_w = 0.166$ nm) and N is the amount of atoms in cluster defined as a cluster mass divided by a mass of a single silver atom.

The TEM observations (Fig. 4) show predominantly large clusters which are outside the range of the QMF. It seems that the larger clusters are mainly neutral and formed by aggregation at the substrate surface. To estimate the fraction of clusters aggregated on the surface at low surface coverage, we performed deposition of mass selected clusters. The QMF was set to select the clusters of approximately 5 nm diameter. In Fig. 5 the cluster

size distribution of mass selected clusters deposited on the substrate and analyzed using TEM is shown. Dashed circle indicates large clusters aggregated on the surface: cluster diameter of 20 nm corresponds to a cluster mass of about 2.2×10^6 atoms. TEM image in the inset of figure 5 shows the surface coverage.

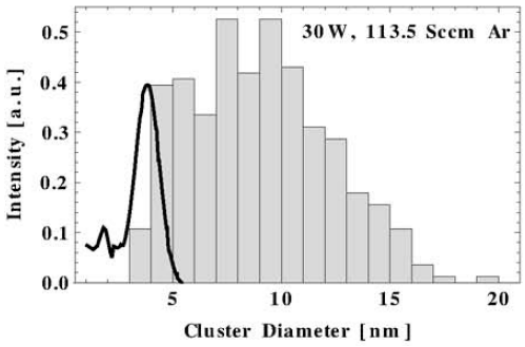

Fig. 4 Comparison of size distribution of clusters in the beam measured using the QMF (black solid curve) with deposited film analyzed using TEM (gray histogram).

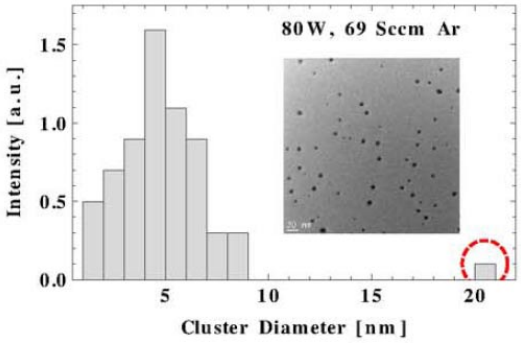

Fig. 5 Deposition of mass selected clusters. Selected cluster size is approximately 5 nm. Red dashed circle indicates large clusters formed by aggregation on the surface.

The study of cluster diffusion on the surface is a challenging task because of the variety and complexity of diffusion processes. Depending on the particular conditions, the cluster motion can proceed in many ways [28]. Generally, cluster mobility decreases and the activation energy for cluster diffusion increases with increasing cluster size [28]. Molecular dynamics simulations [29] have revealed that in dependence on the exact mechanism the energy barrier for a silver cluster of size 201 atoms is in the range of 0.07 eV to 0.43 eV. It is safe to assume that in the present work the clusters on the substrate surface have a thermal energy of about 0.04 eV which corresponds to room temperature (300 K). In the present work clusters consist of about 1000–5000 atoms. Taking the increase of the diffusion activation energy with cluster size into account, we can conclude that surface diffusion has a minor influence on the cluster size distribution on the surface.

3.2 Influence of target erosion

Target erosion is a feature of all planar magnetron based sputtering sources [30]. It can essentially influence the cluster size distribution [31, 32]. Fig. 6 represents the observed influence of the target age on the most probable cluster size and maximal cluster ion current.

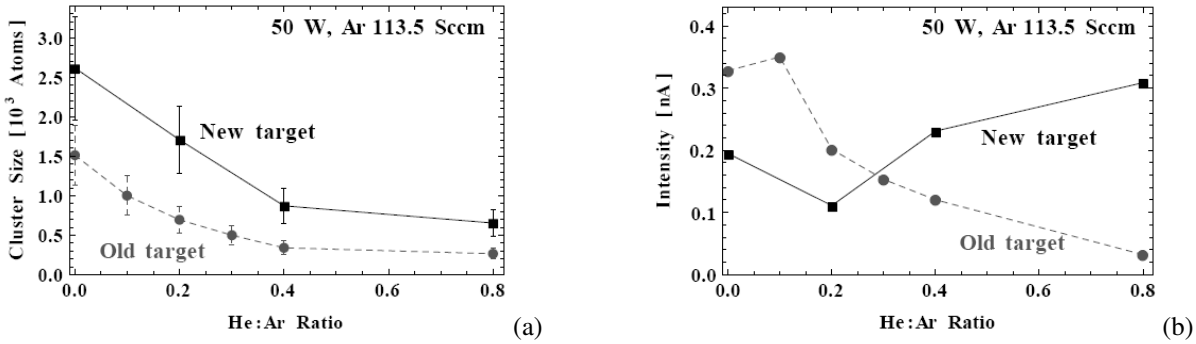

Fig. 6 Influence of the target age on the most probable cluster size (a) and maximum cluster ion intensity (b). Black square symbols (solid line) represent the measurements carried out with a new target and gray filled circles (dashed line) — the used target with a deep sputtered race track profile. Error bars indicate the QMF resolution.

By using an old target with a deep sputtered race track region much smaller clusters are produced and the amount of clusters decreases with addition of He. The new target (with a flat race track profile) shows the same tendency

for the cluster size, but the produced clusters are significantly larger. In contrast the dependence of the cluster ion intensity on the He:Ar ratio is completely different. Contrary to the previous measurements with regard to the He:Ar ratio the cluster ion intensity which is observed with a new target increases with He:Ar ratio. The target erosion influences the total amount of clusters stronger than the He admixture; the variation of the cluster ion current with target age was mentioned in [31] while the effect of the target lifetime on the cluster size distribution is discussed in [32]. Accordingly to [32], the influence of the target erosion is significant for long-term measurements. Small shift of the mass spectra can be seen after 0.1 kWh of magnetron operation, i.e. 1 hour at a discharge power of 100 W. Typical timescales in the present work are about 0.5–1 hour. Thus, we expect that the target erosion has a minor influence on the observations presented below.

3.3 Influence of He:Ar flux ratio on the cluster size distribution

Helium plays an important role in the cluster formation process. It was observed earlier that with an increasing He to Ar flux ratio the size of silver [24, 31] and copper [33] clusters decreases. Fig. 7 represents the measured dependences of cluster size distribution on the He:Ar ratio. It is obvious that the Ag cluster size distribution becomes narrower and shifts towards smaller sizes with increasing He flow. Such dependence is very well reproducible for different Ar flow rates and discharge powers.

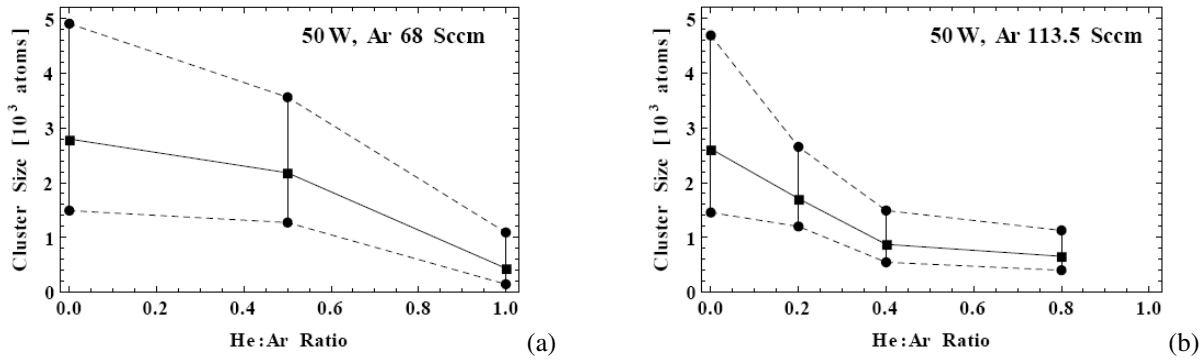

Fig. 7 Influence of the He:Ar flux ratio on the cluster size distribution measured by QMF200 at 50 W discharge power and Ar flow rate 68 sccm (a) and 113.5 sccm (b), respectively. Squares indicate the cluster size with maximum intensity (most probable cluster size). The circles represent the cluster sizes at the half-maximum points (see Fig. 3) of the mass spectra.

Fig. 8(a) shows that the maximum intensity of the cluster size distribution which decreases with He admixture at lower Ar flow rates. At the same time it tends to increase at higher Ar flow rates (Fig. 8(b)).

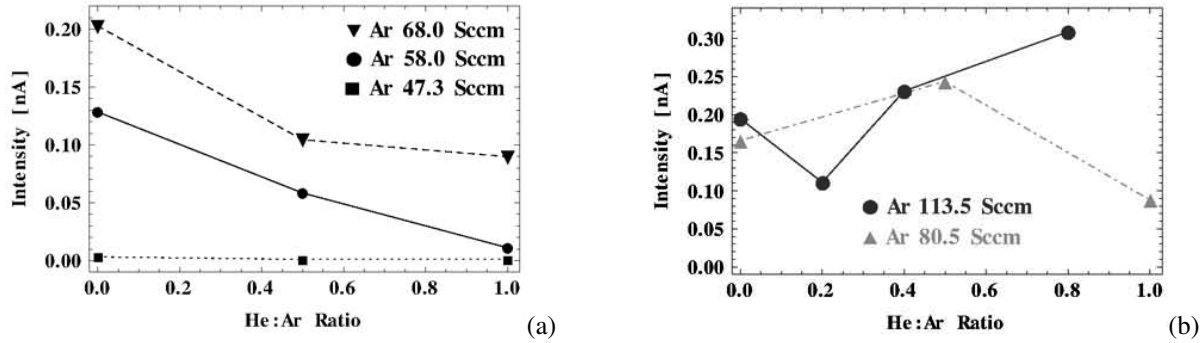

Fig. 8 Influence of the He:Ar flux ratio on the maximal intensity measured by QMF200 at 50 W discharge power and Ar flow rate 47.3–68 sccm (a) and 80.5–113.5 sccm (b).

Pratontep et al. [31] suggest the following explanation of such dependence: more He does not only enhance the growth of large clusters from the cluster seeds; it also generates more nucleation of these seeds. When the latter process becomes dominant, the cluster size will be smaller, assuming that the amount of sputtered material does not change with He fraction [31].

3.4 Discharge Power

Increasing the discharge power usually increases the mean energy of Ar^+ ions, and therefore also the amount of sputtered silver atoms [23] increases. Fig. 9 shows the measured dependence between the cluster size distribution and the discharge power. The black line and points represent the results obtained by the QMF. The gray line and points represent the results obtained by the analysis of deposited clusters by TEM measurements. Because the QMF mass range is limited, it is important to consider also size distributions of deposited clusters to obtain a more comprehensive picture.

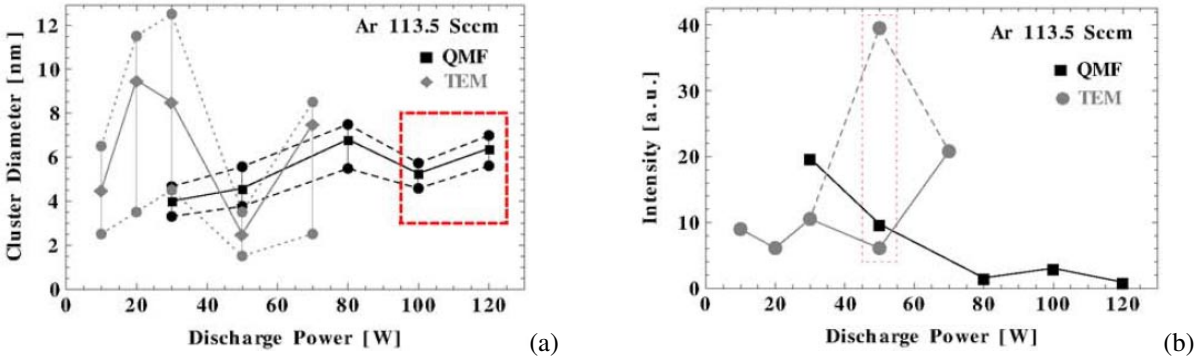

Fig. 9 Influence of the discharge power on the cluster size distribution (a) and maximum intensity (b). Black color represents the QMF measurements (cluster beam), gray — TEM analysis of deposited clusters. Black filled squares and gray filled diamonds on (a) represent the most probable cluster size; black and circles — cluster sizes at half-maximum points. Red dashed rectangle on (a) indicates the range where unreproducible and unstable behavior of the cluster size distribution was observed. Red dotted rectangle on (b) indicates the dispersion of intensity values of deposited clusters caused by non-uniformity of the cluster beam.

Fig. 9a) presents the dependence of the most probable cluster diameter on the discharge power. The error bars give the FWHM of the cluster size distribution. Comparing the results from QMF and TEM, one can conclude that the size distribution of deposited clusters is much broader than that of the cluster beam. At lower discharge powers the TEM results show a lot of large clusters which are out of range for the QMF. These clusters can be produced by the source or can aggregate on the surface after deposition. Formation of large Ag clusters was also reported by [9, 14] with a similar cluster source. Aggregation of silver clusters on the surface was observed and discussed in the framework of the deposition diffusion aggregation (DDA) and the diffusion limited aggregation (DLA) models by Bhattacharyya et. al [11]. At discharge powers from 50 W to 80 W both QMF and TEM show the increase of the most probable cluster size with the discharge power. The cluster size distribution at 50 W is very narrow for both, deposited clusters and the cluster beam. The difference between cluster diameters obtained from QMF and from TEM seems to be caused by different reasons: overestimation of cluster density due to cluster porosity or oxidation, assumption of spherical cluster shape, etc (see [34] for more detailed information). At higher discharge powers (range marked by red dashed rectangle in Fig. 9a) the system becomes unstable and non-reproducible behavior occurs.

Fig. 9b) presents the influence of the discharge power on the maximum cluster intensity. The intensities obtained by QMF and TEM are scaled for better comparison. The results obtained from the TEM analysis of deposited clusters (gray line and points) show an essential variation of the maximum intensity at the same most probable cluster size (range marked by red dotted rectangle in Fig. 9b). Analysis performed in [22] shows that the mean transverse cluster velocity as well as a cluster scattering angle depends on the cluster size. It allows the suggestion that the cluster beam is not uniform. Hence, a small displacement of the substrate from the cluster beam center can lead to a strong intensity variation. In contrast to TEM, position of the QMF detector does not change during the experiment. Therefore we suggest, that the QMF measurements (black line and points on Fig. 9b) reflect the dependence of the maximum cluster intensity on the discharge current more reliably. One can see that it decreases with increase of the discharge power until it reaches 80 W. Previous experiments with a quartz crystal microbalance have shown that at higher powers the system starts to show unstable cluster production rates that fluctuate with time and never reach a steady state. In these QMF measurements the cluster ion intensity drops almost to zero at high powers.

An unstable behaviour of the magnetron system at higher discharge power was also reported in [31]. At discharge powers higher than 80 W an unstable behavior of the plasma occurs and not reproducible mass spectra were observed. Probably it might be caused by heating of the system: the water cooling of the magnetron target becomes insufficient at higher discharge powers. Cooling of the cathode is critical because of high power dissipation at the cathode. For planar magnetron systems cooling limitations will generally determine the maximum operating power of the cathode [30].

3.5 Ar Flow Rate

Ar is responsible for sputtering and acts also as the buffer gas for the cluster formation process. Fig. 10 shows the measured influence of the Ar flow rate on the cluster size distribution.

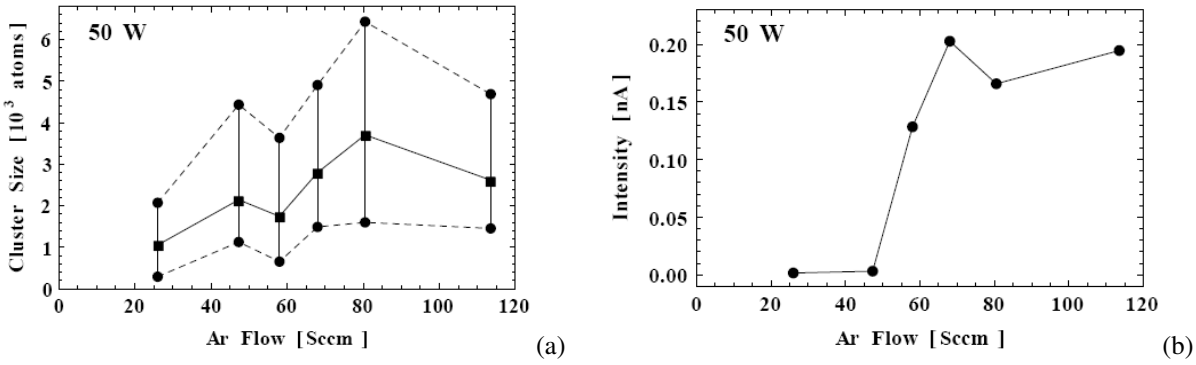

Fig. 10 Influence of the Ar flow rate on the cluster size distribution (a) and maximal intensity (b). Black filled squares on (a) represent the most probable cluster size and black circles — cluster size at half-maximum points.

An increase of the Ar flow rate leads to a higher cluster signal and a slight increase of the cluster size. The same tendency (but for smaller cluster sizes) was observed by [31]. It seems that likely increase of the flow rate leads to a shorter aggregation time and a larger cluster size and width of the mass spectra (Fig. 10a)). These effects are related to an effective transport of material from the aggregation chamber [31], e.g., increase of the maximum cluster ion intensity (Fig. 10b)). At an Ar gas flow rate above 80 sccm the maximum cluster ion intensity does not increase anymore and the cluster size starts to decrease.

4 Conclusions

The influence of the experimental parameters such as discharge power, Ar gas flow rate, and He:Ar ratio on the size distributions of Ag nanoclusters produced by high pressure DC magnetron sputtering source was investigated. Results yielded from mass spectra measured using the quadrupole mass filter (QMF) were compared with analysis of deposited clusters by TEM. Comparison of aforementioned results have revealed that the investigated source produces predominantly large clusters which are out of range of the QMF. It is supposed that cluster aggregation on the surface has a minor influence on the cluster size distributions measured using TEM.

The dependence of the cluster size distribution on the He:Ar ratio indicates that the most probable cluster size decreases with growing fraction of He. Also the mass spectra becomes narrower. Such tendency was observed for different Ar flow rates and different discharge powers. The behaviour of the maximum cluster ion intensity with addition of He is different for lower and for higher Ar gas flow rates. Measured dependence of the cluster size distribution on the Ar flow rate shows that a raising of the Ar flow leads to a larger most probable cluster size and higher maximum cluster ion intensities. Increasing discharge power (Fig. 9) also leads to higher most probable cluster mass but causes lower maximum cluster ion intensities.

Since the QMF only allows the detection of clusters below 10 nm diameter, and source produces predominantly larger clusters, complementary investigations using TEM are necessary for a more detailed study of the dominating mechanisms of the cluster formation in the considered system.

Acknowledgements The work was supported by DFG through SFB-TR24 "Fundamentals of Complex Plasmas", projects B6 and B13. Technical support by Axel Knuth, Robert Mrotzek and Michael Beck is gratefully acknowledged. Thanks to group of Prof. Kienle, CAU Kiel for the TEM measurements. Also we would like to thank Alexandra Pulwicki (DAAD RISE intern) for her help during the measurements and DAAD for support of this internship.

References

[1] P.V. Kashtanov, B.M. Smirnov, and R. Hippler, Physics-Uspekhi **50**, 455–488 (2007).
[2] F. Faupel, V. Zaporojtchenko, T. Strunskus, and M. Elbahri, Advanced Engineering Materials **12**, 1177–1190 (2010).
[3] U. Schürmann, W. Hartung, H. Takele, V. Zaporojtchenko, and F. Faupel, Nanotechnology **16**, 1078 (2005).
[4] S. Liau, D. Read, W. Pugh, J. Furr, and A. Russell, Letters in Applied Microbiology **25**, 279–283 (1997).
[5] H. Lara, N. Ayala-Nez, L. Ixtepan Turrent, and C. Rodrguez Padilla, World Journal of Microbiology and Biotechnology **26**, 615–621 (2010).
[6] C.N. Lok, C.M. Ho, R. Chen, Q.Y. He, W.Y. Yu, H. Sun, P. Tam, J.F. Chiu, and C.M. Che, Journal of Biological Inorganic Chemistry **12**, 527–534 (2007).
[7] J.R. Morones, J.L. Elechiguerra, A. Camacho, K. Holt, J.B. Kouri, J.T. Ramrez, and M. J. Yacaman, Nanotechnology **16**, 2346 (2005).
[8] F. Faupel, V. Zaporojtchenko, H. Greve, U. Schürmann, V.S.K. Chakravadhanula, C. Hanisch, A. Kulkarni, A. Gerber, E. Quandt, and R. Podschun, Contrib. Plasma Phys. **47**, 537–544 (2007).
[9] I. Shyjumon, M. Gopinadhan, O. Ivanova, M. Quaas, H. Wulff, C.A. Helm, and R. Hippler, The European Physical Journal D - Atomic, Molecular, Optical and Plasma Physics **37**, 409–415 (2006).
[10] I. Shyjumon, M. Gopinadhan, C.A. Helm, B.M. Smirnov, and R. Hippler, Thin Solid Films **500**, 41–51 (2006).
[11] S.R. Bhattacharyya, D. Datta, I. Shyjumon, B.M. Smirnov, T.K. Chini, D. Ghose, and R. Hippler, Journal of Physics D: Applied Physics **42**, 035306 (2009).
[12] Z.L. Wang, The Journal of Physical Chemistry B **104**, 1153–1175 (2000).
[13] H. Haberland, M. Karrais, M. Mall, and Y. Thurner, J. Vac. Sci. Technol. A **10**, 3266–3271 (1992).
[14] O. Polonskyi, P. Solar, O. Kylian, M. Drabik, A. Artemenko, J. Kousal, J. Hanus, J. Pesicka, I. Matolinova, E. Kolibalova, D. Slavinska, and H. Biederman, Thin Solid Films **520**, 4155–4162 (2012).
[15] T. Peter, M. Wegner, V. Zaporojtchenko, T. Strunskus, S. Bornholdt, H. Kersten, and F. Faupel, Surface and Coatings Technology **205**, 38–S41 (2011).
[16] S. Bornholdt, T. Peter, T. Strunskus, V. Zaporojtchenko, F. Faupel, and H. Kersten, Surface and Coatings Technology **205**, 388–392 (2011).
[17] M. Bonitz, L. Rosenthal, K. Fujioka, V. Zaporojtchenko, F. Faupel, and H. Kersten, Contrib. Plasma Phys. **52**, 890 (2012).
[18] Oxford Applied Research, Quadrupole Mass Filter QMF200.
[19] D. Bassi, Ionization detectors ii: Mass selection and ion detection, in: Atomic and Molecular Beam Methods, edited by G. Scoles (Oxford University Press, 1988), pp. 180–192.
[20] W. Paul, H.P. Reinhard, and U. von Zahn, Zeitschrift für Physik **152**, 143–182 (1958).
[21] B.M. Smirnov, I. Shyjumon, and R. Hippler, Phys. Rev. E **75**, 066402 (2007).
[22] M. Ganeva, P.V. Kashtanov, B.M. Smirnov, and R. Hippler, Expansion of dense gas flow into vacuum, in preparation, 2012.
[23] R. Hippler, S. Wrehde, V. Stranak, O. Zhigalov, H. Steffen, M. Tichy, M. Quaas, and H. Wulff, Contrib. Plasma Phys. **45**, 348–357 (2005).
[24] H. Haberland, M. Mall, M. Moseler, Y. Qiang, T. Reiners, and Y. Thurner, J. Vac. Sci. Technol. A **12**, 2925–2930 (1994).
[25] H. Haberland (ed.), Clusters of atoms and molecules I (Springer Verlag Berlin Heidelberg, 1995).
[26] J. Campana, International Journal of Mass Spectrometry and Ion Physics **33**, 101–117 (1980).
[27] M. Seidl and M. Brack, Annals of Physics **245**, 275–310 (1996).
[28] K. Oura, V.G. Lifshits, A.A. Saranin, A.V. Zotov, and M. Katayama, Surface Science: An Introduction (Springer Verlag Berlin Heidelberg, 2003).
[29] F. Baletto, C. Mottet, and R. Ferrando, Surface Science **446**, 31–45 (2000).
[30] R.K. Waits, Planar magnetron sputtering, in: Thin film processes, edited by J.L. Vossen and W. Kern (Academic Press, Inc., 24–28 Oval Road, London NW1 7DX, 1978), pp. 131–173.
[31] S. Pratontep, S.J. Carroll, C. Xirouchaki, M. Streun, and R. E. Palmer, Rev. Sci. Instrum. **76**, 045103 (2005).
[32] M. Ganeva, A.V. Pipa, and R. Hippler, Influence of target erosion on the cluster formation in the planar dc magnetron sputtering source, Submitted to Surface and Coatings Technology, 2012.
[33] M. Gracia-Pinilla, E. Martnez, G. Vidaurri, and E. Prez-Tijerina, Nanoscale Research Letters **5**, 180–188 (2010).
[34] V. Stranak, S. Block, S. Drache, Z. Hubicka, C.A. Helm, L. Jastrabik, M. Tichy, and R. Hippler, Surface and Coatings Technology **205**, 2755–2762 (2011).

4.4. Velocity distribution of mass-selected nano-size cluster ions

Plasma Sources Sci. Technol. **22** (2013) 045011 (10pp) doi:10.1088/0963-0252/22/4/045011

Velocity distribution of mass-selected nano-size cluster ions

Marina Ganeva[1], Andrei V Pipa[2], Boris M Smirnov[3], Pavel V Kashtanov[3] and Rainer Hippler[1]

[1] Institute of Physics, University Greifswald, Felix-Hausdorff-Strasse 6, 17489 Greifswald, Germany
[2] Leibniz Institute for Plasma Science and Technology (INP Greifswald), Felix-Hausdorff-Strasse 2, 17489 Greifswald, Germany
[3] Joint Institute for High Temperatures, Russian Academy of Sciences, Bldg. 2, Izhorskaya ul. 13, Moscow 125412, Russia

E-mail: ganeva@physik.uni-greifswald.de

Received 29 January 2013, in final form 7 May 2013
Published 26 June 2013
Online at stacks.iop.org/PSST/22/045011

Abstract
The paper reports on an experimental investigation of the ion velocity distribution function (IVDF) for mass-selected copper cluster ions with a diameter in the range 5–10 nm. The cluster ion beam is produced by a dc magnetron-based gas aggregation source. The measurements are carried out by means of a quadrupole mass filter combined with a basic retarding field analyser. The most probable cluster velocities are in the range 80–180 m s^{-1}; decreasing with cluster size and increasing with buffer gas (Ar) flow. Experimental results are compared with the theoretical model of Smirnov *et al*. Noted discrepancies are explained by the interaction of clusters with buffer gas atoms outside the aggregation chamber during the passage from the orifice towards the detector. This interaction is not included in the theoretical model. Both positively and negatively charged clusters are investigated. The density ratio of positively to negatively charged clusters in the beam is evaluated from the measured IVDFs and compared with the theoretical model.

(Some figures may appear in colour only in the online journal)

1. Introduction

Clusters are small agglomerates of atoms or molecules. Nano-size clusters have a wide range of applications. For example, copper clusters of size 1–10 nm are used for the production of antibacterial nanocomposite films [1] and in catalysis [2, 3]. The size of the clusters and their velocity distribution significantly influence the deposition process [4] and, hence, determine the characteristics of the deposited film. Three modes of cluster–surface interactions can be distinguished [5]: soft-landing, pinning and implantation of clusters. The regime of the interaction affects such properties of the deposited films as wettability [5], degree of implantation of cluster into the surface, and roughness of the film [6–8]. During the impact, the kinetic energy of the cluster is converted into internal energy which accounts for magnetic, electric, optical and other properties of clusters [9, 10]. Thus, control of the kinetic energy of mass-selected nanoclusters is required for deposition of thin films with desired properties.

The measurement of the energy or velocity distribution of charged particles is a constantly recurring problem in plasma physics [11, 12]. Retarding field analyzers (RFAs) are one of the abundantly used solutions for this task due to their easy use and simple implementation [11–15]. In the case where mass discrimination is needed, a combination of mass and energy analyzer, typically known as a plasma monitor, is used [16–19]. However, as far as is known to the authors, the technique has not yet been applied to investigate the velocity distribution of nano-size clusters.

Several attempts to assess cluster drift velocities using analytical models [20, 21], hybrid simulations [22] and experimentation [22] have been made. The experimental work [22] briefly reports on the measurement of the velocity of clusters of 7–50 nm diameter using an electrostatic deflection setup. In the absence of mass selection the size of deflected clusters was determined using the transmission electron microscopy (TEM) technique. This method has certain disadvantages: (i) determination of cluster sizes by electron

microscopy can be misleading, as surface processes such as diffusion or even agglomeration of clusters may change the size distribution at the substrate; (ii) depending on the cluster energy, the shape and size of the cluster may change after the deposition; (iii) the technique does not allow the measurement of the velocity distribution function of the cluster ions.

In this work, the ion velocity distribution function (IVDF) of mass-selected nanoclusters by means of a combination of a quadrupole mass filter (QMF) and basic RFA was investigated. Measurement of the velocity distribution of mass-selected nanoclusters is a challenging task due to the technical problems related to the detection of the very low cluster ion signal. To overcome these difficulties, the detection plates of the QMF were used as an RFA.

The combination of mass and energy analyser is typically used in plasma monitors [16–19]. In such systems the ions first enter the energy analyser and then proceed to the mass spectrometer. For the beam of the nano-sized cluster ions considered in this work, preliminary mass selection is necessary because the broad size range of nanoclusters produced by the source can cause a misleading evaluation of the measured current–voltage characteristics. Another advantage of such positioning of the RFA is that the measured velocities correspond to the ones achieved when cluster ions hit the substrate surface. Thus, the measured velocities account for the properties of the deposited film.

2. Experimental setup

2.1. Production of a beam of nano-sized clusters

Copper nanoclusters are produced with the help of a dc magnetron-based gas aggregation source NC-200 (Oxford Applied Research). A detailed description and schematics of the source are provided elsewhere [23]. Clusters are formed from the Cu atoms sputtered from the target and proceed, together with the flow of buffer gas (Ar), towards the output orifice. In this work a circular orifice with a diameter of 3 mm was used. The experimental conditions of this work are: discharge power 120 W, the temperature of aggregation chamber walls 300 K, aggregation length 12 cm; Ar flow was varied from 15 to 100 sccm, which corresponds to a pressure variation in the aggregation chamber from 19 to 80 Pa, respectively. For mass selection a modified QMF, the QMF-200 produced by Oxford Applied Research was used. After leaving the aggregation chamber through the orifice, clusters enter the QMF, where they are filtered according to their mass-to-charge ratio.

Neither QMF nor RFA distinguish between particles with the same mass-to-charge ratio. There is a tacit assumption that nano-size clusters produced by a gas aggregation source are either singly charged or neutral [24–27]. Numerical simulations [28] show that the probability of multiply charged clusters leaving the aggregation chamber is negligible. Recent experimental studies [29] for Ag clusters produced by a high-pressure gas aggregation source do not reveal any multiply charged clusters of diameter below 30 nm. Other experimental studies of deposited mass-selected Cu clusters of size 6–19 nm

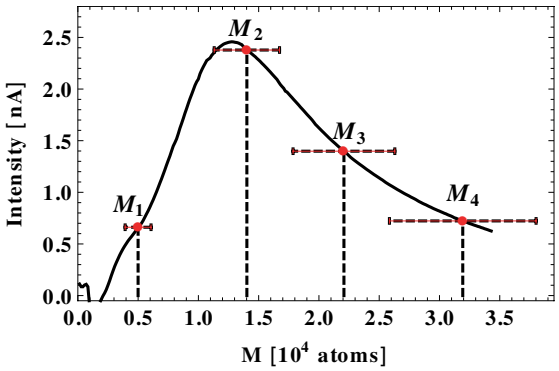

Figure 1. Typical mass spectrum. Circles indicate the cluster masses selected for the investigation. $M_1 = 0.5 \times 10^4$ atoms, $M_2 = 1.4 \times 10^4$ atoms, $M_3 = 2.2 \times 10^4$ atoms and $M_4 = 3.2 \times 10^4$ atoms. Horizontal bars show the resolution of the QMF.

claim that no significant contributions from multiply charged clusters was found [30]. For further analysis we thus consider all clusters to be singly charged or neutral.

Figure 1 shows a typical mass spectrum of cluster ions produced by the nanocluster source. It is important to note that the magnetron target lifetime significantly influences the cluster mass spectrum [23]. Mass discrimination is, hence, necessary to ensure a proper mass selection of the clusters. Furthermore, the mass distribution of the cluster beam produced is very broad and mass filter implementation allows the selection of a relatively narrow mass range that significantly reduces the uncertainty of the mass determination.

For a detailed investigation of the velocity distributions, four cluster masses were selected. Circles in figure 1 indicate the selected cluster masses: $M_1 = 0.5 \times 10^4$ atoms, $M_2 = 1.4 \times 10^4$ atoms, $M_3 = 2.2 \times 10^4$ atoms and $M_4 = 3.2 \times 10^4$ atoms. Corresponding cluster diameters estimated from the liquid drop model [31] are $D_1 = 5$ nm, $D_2 = 7.1$ nm, $D_3 = 8.2$ nm and $D_4 = 9.3$ nm.

Horizontal bars in figure 1 indicate the resolution ΔM of the QMF. The resolution is mainly given by two contributions: the resolution ΔM_L of the QMF and the width ΔM_R of the mass band transmitted through the filter. ΔM_L depends on the QMF geometry and is proportional to the energy of the injected cluster ions [32]. ΔM_R is determined by the amplitude ratio of the ac and dc voltage components applied to the QMF rods [33, 34] and is proportional to the cluster mass. We consider ΔM_L and ΔM_R as two independent contributions to the total mass resolution ΔM, i.e.

$$\Delta M = \sqrt{\Delta M_L^2 + \Delta M_R^2}. \quad (1)$$

Thus, the total QMF resolution depends on the cluster energy. ΔM is important for the evaluation of the cluster mass distribution function from the mass spectra.

2.2. Measurement of the velocity distribution

In the standard configuration of the commercially available QMF-200, the cluster ion current is measured by the control unit. However, the embedded amperemeter has a low accuracy

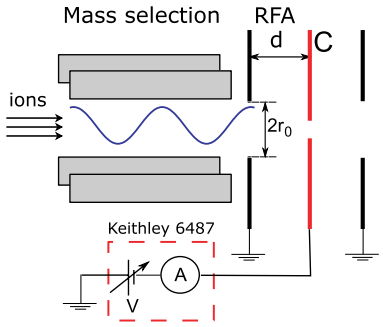

Figure 2. Connection schematics of the QMF plates as a basic RFA. C is a QMF collector acting as a RFA where the ion current is measured. Radius of the input aperture $r_0 = 6$ mm, interplate distance $d = 3$ mm. The radius of the collector aperture is 2 mm.

of ± 0.04 nA that significantly restricts the sensitivity of the experimental setup [34]. This drawback can be overcome by replacing the internal amperemeter with an external femtoamperemeter. In this work, a Keithley 6487 sourcemeter with an interface for connection to the QMF was used. It provides a femtoamperemeter and a voltage source which allows for accurate control of the collector potential. The sourcemeter thus enables the use of the QMF detection plate as a basic RFA. To control the modified mass spectrometric system, self-developed software was used.

Figure 2 presents connection schematics of the QMF plates as a basic parallel-plate RFA. The entrance plate with an orifice of radius $r_0 = 6$ mm is grounded. The collector C is situated at a distance of $d = 3$ mm from the entrance plate. Cluster ions of selected mass proceed towards the QMF collector C which can be biased by a voltage V in the range ± 500 V with a step size of 1 V. Only ions having kinetic energies E larger than the potential barrier will eventually reach the collector.

The IVDF $f(v)$ is proportional to the derivative of the collection current. For a single species [12, 15]

$$\frac{\mathrm{d}I(V)}{\mathrm{d}V} = \frac{e^2}{M} f(v), \tag{2}$$

where V is the retarding potential, M is the ion mass, e is the elementary charge and $v = \sqrt{|2eV/M|}$. The RFA technique allows measurement of the IVDF. The difference between energy and velocity distribution functions is discussed by Ellmer *et al* [16] in detail.

The limiting resolution Δv_{RFA} of the basic RFA is determined mainly by its finite entrance aperture and can be estimated as [11]

$$\frac{\Delta v_{\mathrm{RFA}}}{v} = \frac{1}{2}\frac{\Delta E}{E} = \frac{1}{2}\sin^2\left(\frac{r_0}{4d}\right) \approx 0.115. \tag{3}$$

Δv_{RFA} accounts for the full-width at half-maximum (FWHM) of the RFA instrument function.

Typically, the measurement of current–voltage characteristics takes about 3–5 min. Since the magnetron target lifetime under the experimental conditions considered is limited to 6–7 h [23], it was necessary to keep the experiment time as short as possible. On the other hand, averaging of multiple curves provides a better signal-to-noise ratio. Taking both factors into account, current–voltage characteristics for conditions with high signal-to-noise ratio was typically measured three times, and up to eight times for lower signals. Typical current–voltage curves measured for the cluster ions of mass M_2 are presented in figure 3.

As can be seen in figure 3, the measured current–voltage characteristics are affected by the common disadvantages of the basic RFA technique: the absence of charge selection and secondary electron emission. After all negatively charged ions are rejected by the retarding potential, the measured current value is not zero, as it would be in the case of an ideal cutoff curve, but equal to the total current of the positively charged clusters I_+ (figure 3, left). The case is similar for the positively charged clusters. However, the constant shift of the cutoff curve has no influence on the evaluation of the cluster velocities, as only the derivatives of the current–voltage characteristics are of interest.

The smooth variation of the current with a voltage of near zero (the regions marked by the dashed rectangle in figure 3) seems to be caused by secondary electron emission [11] which is a well-known disadvantage of the basic RFA. These distortions of the current–voltage characteristics cause artefacts in the evaluated velocity distribution function. In this work these artefacts are ignored. For the differentiation of the measured curves, linear interpolation was used. The resulting IVDFs are presented in figures 4 and 5.

3. Results and discussion

3.1. Cluster size distribution

We want to emphasize that the mass spectrum in figure 1 has a maximum, while the theoretical analysis [35, 36] shows that cluster growth in a uniform plasma will result in a monotonic function. Indeed, if clusters are formed from an atomic vapour in a uniform gas, as takes place during cluster growth in a magnetron discharge, the size dependence for the distribution function has the form [35] $f_n \sim n^{-2/3}$, where n is the number of cluster atoms. The observed size distribution (figure 1) is explained by the loss of small clusters in the aggregation chamber as a result of cluster attachment to the walls. In this case the average displacement of clusters in the aggregation chamber $\bar{x} = \sqrt{4D_n\tau_r}$ (D_n is the diffusion coefficient of clusters in a buffer gas, τ_{r} is the residence time of clusters in the aggregation chamber) is comparable to the chamber radius. Under the present experimental conditions ($p = 19$ Pa, $T = 300$ K) for clusters of size $n = 1.5 \times 10^4$ atoms, the diffusion coefficient in argon is $D_n = 6.3\,\mathrm{cm^2\,s^{-1}}$. For a residence time of clusters in the aggregation chamber of $\tau_{\mathrm{r}} = 1$ s this yields an average displacement of clusters in the aggregation chamber of $\bar{x} \approx 5$ cm, which corresponds to the chamber radius. Since the diffusion coefficient D_n decreases with cluster size [37], the displacement $\bar{x}$ will be smaller for larger clusters. Thus, this effect can cause the mass spectra with a maximum, as shown in figure 1.

3.2. Cluster velocity distribution function

For an Ar flow of 15 sccm a sufficiently large signal for both positively and negatively charged copper clusters was detected.

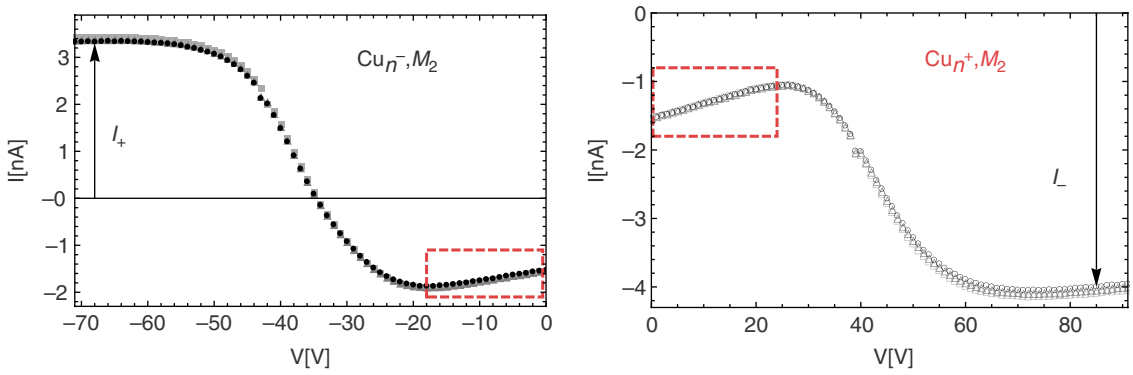

Figure 3. Typical ion current–voltage characteristics measured for negative (left) and positive (right) cluster ions of mass M_2. Dashed rectangle indicates the distortion of the measured curve due to secondary electron emission [11]. Arrows marked with I_+ and I_- show the current value of positive and negative cluster ions correspondingly.

Figure 4 displays the velocity distributions for positive (right) and negative (left) cluster ions of mass M_2, M_3 and M_4. The negative tail of the measured data at a lower velocity range is related to secondary electron emission. Since the suggested effect is more pronounced at lower collector voltages [11], we suppose that it has a minor influence in the velocity range of interest here. It can also be seen in figure 4 that the measured velocity distributions are slightly asymmetric in the lower velocity range. This seems to be caused by the aforementioned secondary electron emission effect and is in close agreement with a decrease of its influence for a higher velocities. Thus, in this work the negative tail points will be ignored.

The experimental data are fitted with a Gauss function:

$$f_G(v) = \frac{a}{\sigma\sqrt{2\pi}} \exp\left[-\frac{(v - v_p)^2}{2\sigma^2}\right]. \quad (4)$$

The fit parameter a accounts for the density of clusters divided by the cluster mass, v_p is the most probable velocity and σ is related to the FWHM of the distribution as

$$\mathrm{FWHM} = 2\sigma\sqrt{2\log 2}. \quad (5)$$

Error bars in figure 4 show the measurement error Δv caused by the limited resolution of QMF and RFA. The thick solid lines in figure 4 are a fit of the measured data points with Gauss function (4). Thin lines indicate the fit error. The fit coefficients are presented in table 1. As can be seen in figure 4, the fit function (4) shows close agreement with the measured velocity distributions. It also appears that the width of the distribution is nearly the same for the clusters of mass M_2, M_3 and M_4 (figure 4 and table 1).

As the velocity resolution of the used RFA is rather low, it is reasonable to question whether the width of the measured IVDFs is defined by the intrinsic distribution function or by the instrument function of the RFA. We assume the instrument function of the RFA to be a Gaussian function with FWHM equal to Δv_{RFA} given by equation (3). The evaluated FWHM of the intrinsic IVDF is shown in table 1. As one can see, the correction on the instrument function does not exceed the estimated experimental error. Thus, the width of the measured IVDF is mainly defined by the width of the intrinsic distribution function.

In contrast to the larger cluster masses, the distributions for clusters of mass M_1 (figure 5) are significantly broader (especially for positive clusters) and asymmetric; this can be interpreted as the presence of two cluster groups. The reasons for the different IVDF shape are not yet understood. A possible explanation may be that clusters during the passage from the orifice towards the detector undergo two different kinds of interactions: collisions with fast argon atoms and interaction with slow, charged clusters. Smaller clusters are efficiently accelerated in collisions with buffer gas atoms which can lead to formation of the faster group of clusters of mass M_1. The slower group then should be a consequence of an interaction with slow, charged clusters. Alternatively, broadening of the IVDF may be caused by the presence of the multiply charged clusters, e.g. doubly charged clusters of mass $2 \times M_1$ could appear with a similar velocities to the slow group, whereas singly charged clusters of mass M_1 are fast. A third explanation is that the second velocity group may be caused by fragmentation of larger clusters during the pathway from the orifice to the detector. Additional investigations are thus required for an accurate conclusion.

3.3. *Cluster drift velocity*

The regime of flow propagation under experimental conditions $p = 19\,\mathrm{Pa}$, $T = 300\,\mathrm{K}$ corresponds to the density of argon atoms in the aggregation chamber $N_{Ar} = 4.5 \times 10^{21}\,\mathrm{m}^{-3}$ and the mean free path of argon atoms in argon $\lambda = 1/(N_{Ar}\sigma_g) = 0.6\,\mathrm{mm}$, where $\sigma_g = 3.7 \times 10^{-19}\,\mathrm{m}^2$ is the gas-kinetic cross-section for the collision of two argon atoms at room temperature. As is seen, the mean free path of argon atoms significantly exceeds the typical cluster radius (2.5–5 nm), which corresponds to a kinetic regime of the atom–cluster interaction [37], i.e. each time only one atom strongly interacts with a cluster.

The small ratio of the mean free path to the orifice radius $\lambda/R = 0.4$ allows the application of an analytical model [20] for determining the cluster drift velocity. According to the analytical model [20], there is an equilibrium inside the aggregation chamber of the nanocluster source between the drift velocities of buffer gas (Ar) atoms and clusters. However, near the output orifice Ar atoms become accelerated. The

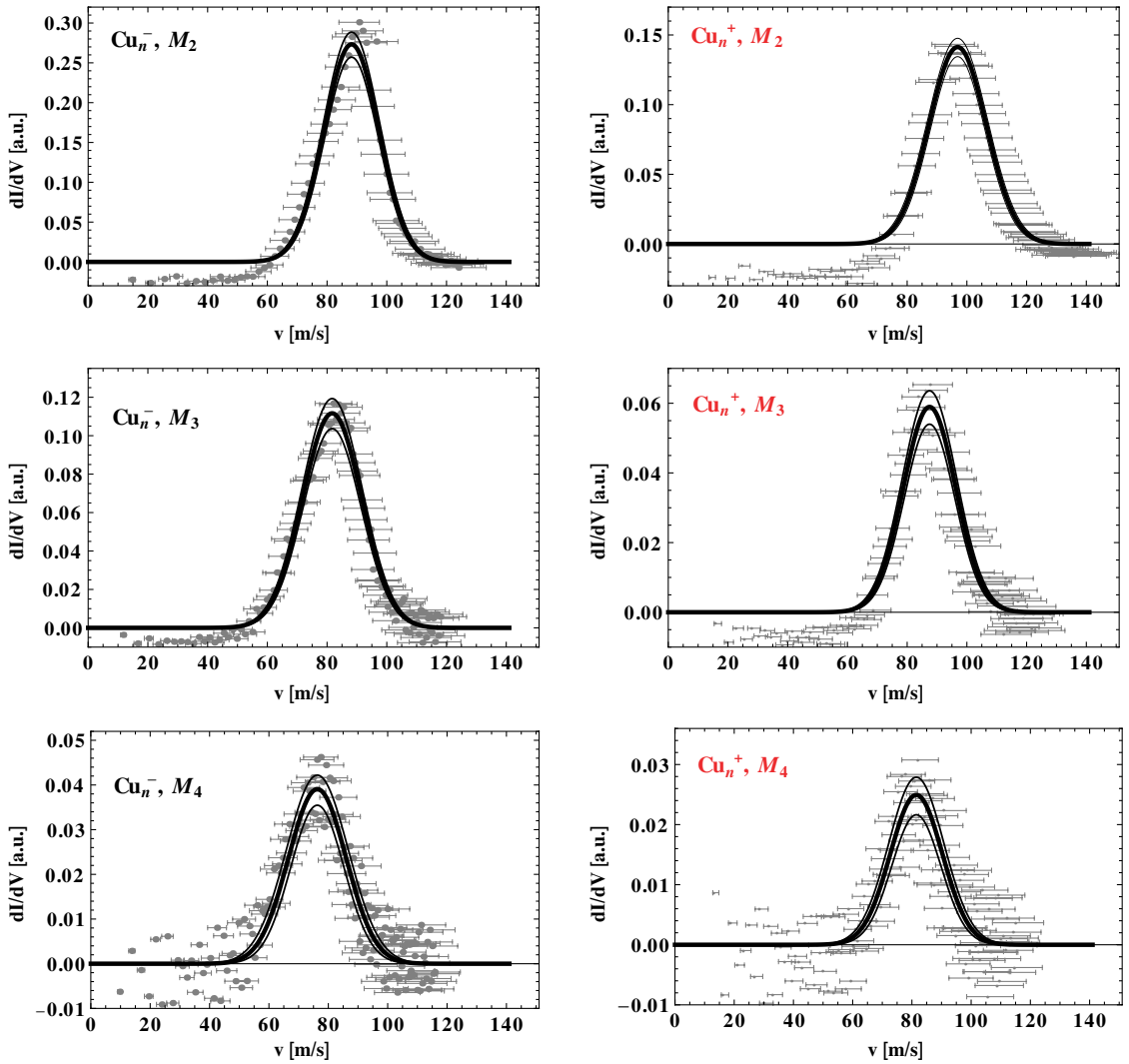

Figure 4. Evaluated IVDFs for positive (right) and negative (left) cluster ions of mass M_2, M_3 and M_4. Data points are obtained from the differentiation of the measured curves. The thick solid line corresponds to the fit of these points using equation (4). Thin lines show the fit error. Experimental conditions: Ar flow 15 sccm, discharge power 120 W, pressure 19 Pa.

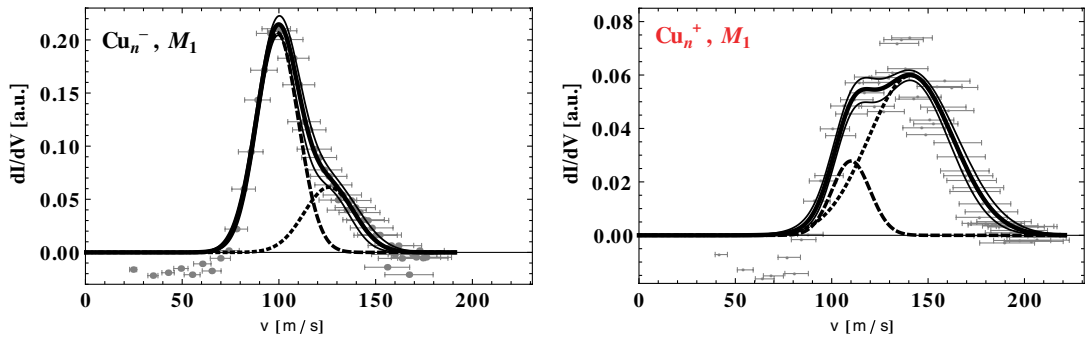

Figure 5. Evaluated IVDFs for positive (right) and negative (left) clusters of mass M_1. Data points are obtained from the differentiation of the measured curves. The thick solid line shows the fit of these points using the sum of two equations (4). Dotted and dashed lines show the contribution of different peaks. Thin solid lines indicate the fit error.

time is too short to reach equilibrium again, and hence, the clusters become significantly slower than the Ar atoms. Nevertheless, an increase in the Ar flow will further accelerate the clusters. Figure 6 shows the measured dependence of the most probable velocity on the Ar flow Q for negatively charged clusters of mass M_2. The size of the error bars is related to the signal-to-noise ratio for the measured current–voltage characteristics. It is seen that an increase in the buffer gas flow accelerates the clusters; this is in qualitative agreement with the theoretical model [20]. The asterisk indicates recent velocity measurements [22] for silver clusters of a diameter of 7 nm. The value differs significantly from our results. The difference

Table 1. Fit coefficients for Gauss function (4) for measured cluster IVDFs presented in figures 4 and 5.

	Negative clusters			
Mass	a_- (a.u.)	v_p^- (m s^{-1})	FWHM$^-$ (m s^{-1})	FWHM^{*-} (m s^{-1})
M_1 fast	2.0 ± 0.5	126 ± 10	31 ± 6	27
M_1 slow	5.6 ± 0.3	99 ± 8	25 ± 4	22
M_2	6.3 ± 0.5	88 ± 7	22 ± 3	19
M_3	2.77 ± 0.25	82 ± 6	23 ± 2	21
M_4	0.95 ± 0.15	76 ± 6	23 ± 4	21
	Positive clusters			
Mass	a_+ (a.u.)	v_p^+ (m s^{-1})	FWHM$^+$ (m s^{-1})	FWHM^{*+} (m s^{-1})
M_1 fast	3.3 ± 0.4	141 ± 11	52 ± 6	47
M_1 slow	0.69 ± 0.01	110 ± 8	23 ± 2	19
M_2	3.4 ± 0.3	97 ± 7	23 ± 2	20
M_3	1.30 ± 0.15	88 ± 7	21 ± 3	18
M_4	0.55 ± 0.10	82 ± 6	21 ± 3	19

Note: FWHM* were evaluated by deconvolution with the RFA instrument function.

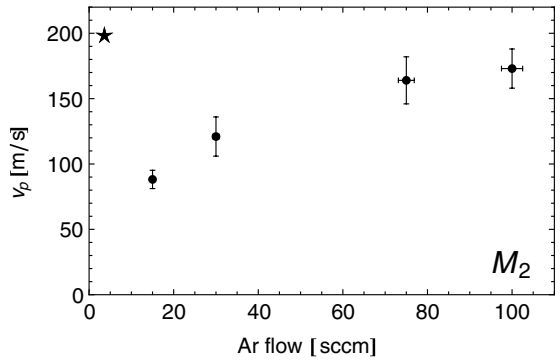

Figure 6. Dependence of the most probable velocity v_p of negatively charged clusters of mass M_2 on the Ar flow. The asterisk indicates the velocity value for clusters of diameter 7 nm measured in [22].

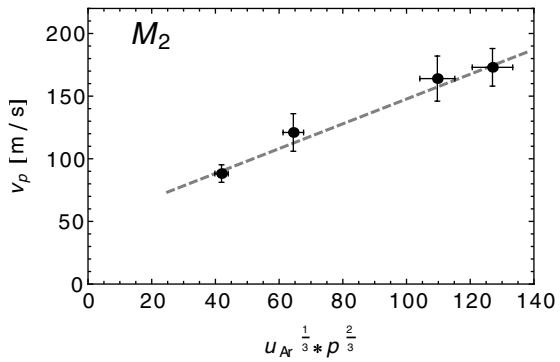

Figure 7. Dependence of the most probable cluster velocity on the Ar flow for clusters of mass M_2 plotted versus $u_{\mathrm{Ar}}^{\frac{1}{3}} p^{\frac{2}{3}}$. The dashed line represents a linear fit of the data points with equation (8).

can be explained by different output orifice geometries and an essentially higher pressure in [22] that significantly affects the gas flow and, hence, the cluster velocity.

The model [20] allows us to derive the following expression for the cluster drift velocity w:

$$w = \frac{3.77 R^{2/3} r_{\mathrm{W}}^{4/3}}{m_{\mathrm{Cu}}^{4/9} G^{2/3}} \left(\frac{m_{\mathrm{Ar}}}{kT}\right)^{1/3} \frac{u_{\mathrm{Ar}}^{1/3} p^{2/3}}{M^{2/9}}, \tag{6}$$

where R is the orifice radius, r_{W} is the Wigner–Seitz radius ($r_{\mathrm{W}} = 0.147$ nm for copper), m_{Cu} and m_{Ar} are the masses of Cu and Ar atoms, respectively, k is the Boltzmann constant, and T and p are the gas temperature and pressure in the aggregation chamber, respectively. G is a geometrical factor related to orifice and nozzle shape and contributing to the typical time for the variation of the flow velocity. The argon flow velocity u_{Ar} can be evaluated as [21]

$$u_{\mathrm{Ar}} = \frac{Q}{\pi R^2 N_{\mathrm{Ar}}}, \tag{7}$$

where Q is the gas flow. For comparison with the theoretical model [20] we will use the most probable cluster velocity v_p obtained from the measured cluster velocity distribution function.

Considering the dependence (6), a quantitative comparison of experimental data with the theoretical model can be done. In figure 7 the measured cluster velocities are plotted versus $u_{\mathrm{Ar}}^{\frac{1}{3}} p^{\frac{2}{3}}$. The dashed line represents a linear fit of the data points using

$$v_p = v_0 + \eta M^{-\frac{2}{9}} u_{\mathrm{Ar}}^{\frac{1}{3}} p^{\frac{2}{3}}, \tag{8}$$

where the fit parameters $v_0 = 48 \pm 6$ m s^{-1} and $\eta = 8.3 \pm 0.5$.

Equation (8) represents the theoretical dependence (6) with an additional offset velocity v_0. Since the model [20] evaluates the cluster drift velocity at the orifice, whereby the cluster velocity was measured at a distance of about 30 cm away from the orifice, it is reasonable to assume that the offset v_0 is caused by the further cluster acceleration during their way from the orifice towards the QMF detection plates. Let us estimate whether collisions with neutral argon atoms outside of the aggregation chamber may influence the cluster velocity. An equilibrium drift velocity of clusters is established after $\sim M/m_{\mathrm{Ar}}$ collisions with buffer gas atoms [21]. For clusters

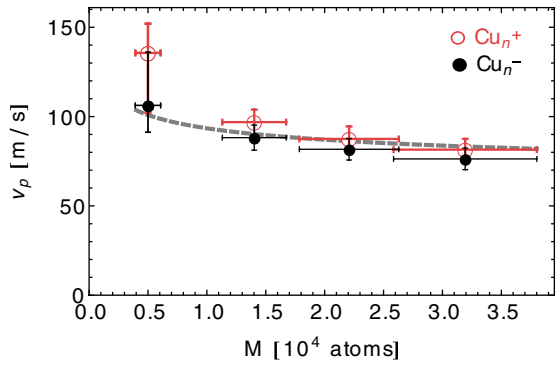

Figure 8. Dependence of the most probable cluster velocity v_p on the cluster mass. Closed symbols indicate negative clusters, open symbols positive clusters. For clusters of mass M_1: weighted-mean velocities are shown, vertical bars represent the observed velocity range for fast and slow cluster groups. The dashed curve represents the dependence (8) with fit coefficients obtained from figure 7.

of mass M_1–M_4 the value of $M/m_{Ar} \approx (0.8\text{–}5) \times 10^4$. The number of collisions for a single cluster with the buffer gas atoms per second is

$$\nu = N_b \langle u_{Ar} - v_p \rangle \sigma, \tag{9}$$

where $\langle u_{Ar} - v_p \rangle$ is the average relative velocity of clusters in argon, N_b is the argon atom density in the beam behind the orifice and $\sigma = \pi r_c^2$ is the cluster cross-section. $N_b = 0.77 N_{Ar}$ depends on the argon density N_{Ar} in the aggregation chamber [37]. During our experiment the pressure in the aggregation chamber was varied within the range 19–80 Pa for different argon flows; this corresponds to $N_b = (3.4\text{–}14) \times 10^{21}\,\mathrm{m}^{-3}$ at $T = 300\,\mathrm{K}$. The measured cluster velocities v_p (figures 6 and 7) are in the range of about 80–180 m s^{-1}. Considering that the radius r_c for clusters of mass M_2 is 3.5 nm and the approximate time of flight τ of the cluster over the 30 cm distance from the orifice to the QMF detection plates is in the range 1.5–3 ms, we obtain $\nu\tau \sim (4\text{–}8) \times 10^4$. Thus, the cluster under way from the orifice has about $(4\text{–}8) \times 10^4$ collisions with neutral gas atoms. The number of collisions is thus comparable to M/m_{Ar} and may significantly accelerate the cluster. Hence, the offset v_0 accounts for the effect of a cluster acceleration after passage through an orifice.

Equation (8) also allows for a quantitative comparison of the measured dependence of cluster velocity on the cluster mass (figure 8) with the theoretical model [20]. The measured velocity distribution function allows for an accurate determination of the most probable velocity v_p for all selected cluster masses with the exception of M_1. For clusters with mass M_1, significantly broader and asymmetric IVDFs were observed (figure 5) that do not allow for an unambiguous determination of the most probable velocity. Therefore, for clusters of mass M_1, weighted-mean velocities are taken. They are shown as points in figure 8 and error bars on the velocity axis represent the observed velocity range. Full error bars on the mass axis show the QMF resolution ΔM evaluated using expression (1). For clusters of mass M_2–M_4, error bars on the velocity axis represent the experimental error.

A decrease in the most probable cluster velocity with increasing cluster mass for both positively and negatively charged clusters can be seen in figure 8. The present results are in qualitative agreement with other observations and with hybrid simulations [22]. The dashed line in figure 8 represents the dependence (8) with fit coefficients obtained from figure 7. In spite of the dashed line being in the range of the measurement error, as one can clearly see in figure 8, the dependence (8) decreases more slowly with the cluster mass than the experimental points. It is reasonable to suggest that for this discrepancy the effect of the cluster acceleration after the orifice is responsible. During the collision, elastic energy transfer from an Ar atom to the cluster is proportional to m_{Ar}/M. Thus, the acceleration of bigger clusters is slower and requires more collisions. It is evident that the probability of collision is higher for larger clusters: the collision cross-section increases with the cluster radius as an r_c^2 [20] while the cluster mass $M \propto r_c^3$ [31]. Thus, even with a higher probability of collision, acceleration of larger clusters is less effective than the smaller ones. This allows us to conclude that the offset v_0 decreases with cluster size increase; this can distort the dependence of the cluster velocity on the cluster mass (figure 8).

In figures 4, 5 and 8 it is clearly seen that the most probable velocity for positive clusters is slightly higher than for negative clusters. We assume that this effect is related to a potential drop near the chamber walls: on one hand, a secondary plasma near the orifice where clusters are accelerated is positively charged, and on the other hand, walls near the orifice are negatively charged. The resulting total electric potential ΔV near the orifice can be estimated from the energy conservation law as follows:

$$-2e\Delta V = \frac{M}{2}[(v_p^+)^2 - (v_p^-)^2], \tag{10}$$

where M is the cluster mass. On the basis of the data of figure 4 and table 1 we obtain $\Delta V = -4 \pm 1\,\mathrm{V}$ for all considered cluster masses. However, a more detailed theoretical analysis is necessary to understand the processes.

3.4. Cluster charge

A further benefit of the cluster IVDF measurement is the additional information about the relative amount of positively and negatively charged clusters in the beam. A theoretical analysis of the cluster charging processes [21, 38] allows the derivation of the following relation for the density ratio of positively (N_+) and negatively (N_-) charged cluster ions:

$$\frac{N_+}{N_-} = \frac{m_e}{m_i}\left(\frac{N_i}{N_e}\right)^2 \frac{kT_i + \dfrac{e^2}{4\pi\epsilon_0}\dfrac{1}{r_c}}{kT_e + \dfrac{e^2}{4\pi\epsilon_0}\dfrac{1}{r_c}}, \tag{11}$$

where m_e and m_i are the electron and ion mass, respectively, N_e and N_i are the electron and ion density, respectively, T_e and T_i are the electron and ion temperatures, respectively, e is the elementary charge, ϵ_0 is the vacuum permittivity and r_c is the cluster radius. The ratio N_+/N_- is thus entirely defined by the plasma parameters and by the cluster size.

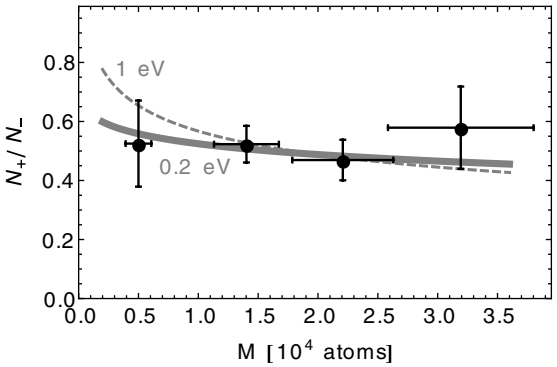

Figure 9. Ratio of positive to negative clusters. For clusters of mass M_1, the sum of slow and fast clusters is shown. Lines show the theoretical dependence (11) with the following electron T_e and ion T_i temperatures: dashed line $T_e = 1$ eV, $T_i = 300$ K; thick solid line $T_e = 0.2$ eV, T_i is in the range 300–1000 K. The thickness of this line represents the variation with T_i.

Our observations confirm that the experimental conditions significantly influence the densities of positively and negatively charged clusters. In this work a sufficient signal for positively charged clusters was detected only at an Ar flow of 15 sccm. At other Ar flows only negatively charged clusters were detected. In contrast, the high-pressure nanocluster source of [22] produces a higher number of positively charged clusters. The N_+/N_- ratio for clusters produced by another high-pressure nanocluster source [39] varies in the range from 0.2 to 1.5 depending on the experimental conditions and cluster size.

The dependence of the density ratio of positive N_+ and negative N_- clusters on the cluster mass is shown in figure 9. The N_+/N_- was evaluated as a ratio of the areas of corresponding IVDFs (fit coefficients a_+ and a_-, table 1). For clusters of mass M_1, the sum of slow and fast clusters is displayed. Figure 9 shows that the dependence of N_+/N_- on the cluster mass is very slight, if any.

For comparison with the theoretical dependence (11), plasma parameters are needed. Unfortunately these are not known for our experimental conditions. Since ions in the secondary plasma are thermalized due to collisions with buffer gas, we assume that T_i is equal to the gas temperature, i.e. $T_i = 300$ K. A change of N_+/N_- with T_i variation in the range 300–1000 K is negligibly small. It is shown by the thickness of the solid line in figure 9. By contrast, the N_+/N_- ratio is much more sensitive to a T_e variation. The solid and dashed lines in figure 9 present this dependence for electron temperatures of 0.2 eV and 1 eV, respectively.

Unfortunately the error of the N_+/N_- determination is too large for a precise evaluation of T_e and N_i/N_e. Nevertheless, a rough estimation of these parameters by a fit of the experimental points with the dependence (11) is possible. Such a fit gives us the following values: $T_e = 0.2 \pm 0.1$ eV and $N_i/N_e = 220 \pm 100$. The fit line in figure 9 corresponds to the thick solid line. The value of N_i/N_e for a cluster-containing magnetron plasma estimated by [21] is about 330 for titanium plasma and about 420 for silver plasma. Thus, the value N_i/N_e obtained in this work is within the plausible range. Electron temperatures in the magnetron discharge were studied by various researchers [40–48]. In [40] $T_e = 0.5$ eV was measured under comparable experimental conditions. In this work we have higher pressure, discharge current and distance from the cathode, which lead to lower electron temperature. As a result, $T_e \approx 0.2$ eV is also within the reasonable range.

Values for T_e and N_i/N_e allow the assessment of the fraction N_0 of neutral clusters produced by the source. Using the expressions for N_-/N_0 and N_+/N_0 ratios provided by the theoretical model [38], and considering that $N_- + N_+ + N_0 = 100\%$, we obtain $N_0 = 70$–80% for clusters in the considered size range. N_0 is found to be larger for smaller clusters and monotonically decreases with increasing cluster size.

4. Conclusions

The ion velocity distribution function (IVDF) of positively and negatively charged mass-selected nanoclusters produced by magnetron sputtering in a gas aggregation tube was investigated. IVDFs are presented for clusters with a mass M_1–M_4 corresponding to cluster diameters of about 5–10 nm. The most probable velocities measured after the clusters left the aggregation region through a small orifice of a diameter of 3 mm are in the range 80–180 m s^{-1}. In general, the measured IVDFs are well described by a Gaussian distribution. For the smallest clusters, significantly broader and asymmetric velocity distributions were observed. These characteristics can be interpreted as indicating two groups of cluster ions: one accelerated in collisions with argon atoms and one dominated by cluster–cluster interactions. Much of this interaction takes place near the orifice but also during the cluster's passage towards the QMF detection plates. The latter interaction causes an offset velocity which is not considered by the theoretical model.

The employed technique is suitable for both positively and negatively charged nanocluster ions and allows for an estimate of the relation between positively and negatively charged clusters in the beam. Comparison of the experimental results with the theoretical model can provide a method to assess the electron temperature and the ratio of electron and ion densities in the cluster-containing secondary plasma. Hence a plausible value of $T_e \approx 0.2$ eV was obtained for the present conditions. Further experiments are necessary to confirm the accuracy of this method.

Acknowledgments

This work was supported by the Deutsche Forschungsgemeinschaft (DFG) through SFB-TR24 *Fundamentals of Complex Plasmas*. Valuable discussions with Dr Vasile Vartolomei (Greifswald), Kenji Fujioka (Kiel), and the technical support of Axel Knuth and Robert Mrotzek are gratefully acknowledged.

References

[1] Cioffi N, Torsi L, Ditaranto N, Tantillo G, Ghibelli L, Sabbatini L, Bleve-Zacheo T, D'Alessio M, Zambonin P G and Traversa E 2005 Copper nanoparticle/polymer composites with antifungal and bacteriostatic properties *Chem. Mater.* **17** 5255–62

[2] Ressler T, Kniep B L, Kasatkin I and Schlögl R 2005 The microstructure of copper zinc oxide catalysts: bridging the materials gap *Angew. Chem. Int. Edn Engl.* **44** 4704–7

[3] Vukojevic S, Trapp O, Grunwaldt J-D, Kiener C and Schüth F 2005 Quasi-homogeneous methanol synthesis over highly active copper nanoparticles *Angew. Chem. Int. Edn Engl.* **44** 7978–81

[4] Gong H, Lu W, Wang L, Li G and Zhang S 2012 The effect of deposition velocity and cluster size on thin film growth by cu cluster deposition *Comput. Mater. Sci.* **65** 230–4

[5] Popok V N, Barke I, Campbell E E B and Meiwes-Broer K-H 2011 Cluster-surface interaction: From soft landing to implantation *Surf. Sci. Rep.* **66** 347–77

[6] Moseler M, Rattunde O, Nordiek J and Haberland H 2000 On the origin of surface smoothing by energetic cluster impact: Molecular dynamics simulation and mesoscopic modeling *Nucl. Instrum. Methods Phys. Res.* B **164–165** 522–36

[7] Haberland H, Insepov Z and Moseler M 1995 Molecular-dynamics simulation of thin-film growth by energetic cluster impact *Phys. Rev.* B **51** 11061–7

[8] Qiang Y, Thurner Y, Reiners Th, Rattunde O and Haberland H 1998 Hard coatings (tin, tixal1xn) deposited at room temperature by energetic cluster impact *Surf. Coat. Technol.* **100–101** 27–32

[9] Makarov G N 2011 Kinetic methods for measuring the temperature of clusters and nanoparticles in molecular beams *Phys.—Usp.* **54** 351–70

[10] Makarov G N 2008 Cluster temperature. Methods for its measurement and stabilization *Phys.—Usp.* **51** 319–53

[11] Simpson J A 1961 Design of retarding field energy analyzers *Rev. Sci. Instrum.* **32** 1283–93

[12] Böhm C and Perrin J 1993 Retarding-field analyzer for measurements of ion energy distributions and secondary electron emission coefficients in low-pressure radio frequency discharges *Rev. Sci. Instrum.* **64** 31–44

[13] Hippler R, Kredl J and Vartolomei V 2008 Ion energy distribution of an inductively coupled radiofrequency discharge in argon and oxygen *Vacuum* **83** 732–7

[14] Baloniak T, Reuter R, Flötgen C and von Keudell A 2010 Calibration of a miniaturized retarding field analyzer for low-temperature plasmas: geometrical transparency and collisional effects *J. Phys. D: Appl. Phys.* **43** 055203

[15] Hutchinson I H 2002 *Principles of Plasma Diagnostics* (Cambridge: Cambridge University Press)

[16] Ellmer K, Wendt R and Wiesemann K 2003 Interpretation of ion distribution functions measured by a combined energy and mass analyzer *Int. J. Mass Spectrom.* **223–224** 679–93

[17] Coburn J W 1970 A system for determining the mass and energy of particles incident on a substrate in a planar diode sputtering system *Rev. Sci. Instrum.* **41** 1219–23

[18] Walton S G, Fernsler R F and Leonhardt D 2007 Measurement of ion energy distributions using a combined energy and mass analyzer *Rev. Sci. Instrum.* **78** 083503

[19] Jiang N, Zhao N, Liu H and Fang T 2005 Mass-resolved retarding field energy analyzer and its measurement of ion energy distribution in helicon plasma *Nucl. Instrum. Methods Phys. Res.* B **229** 508–18

[20] Smirnov B M, Shyjumon I and Hippler R 2007 Flow of nanosize cluster-containing plasma in a magnetron discharge *Phys. Rev.* E **75** 066402

[21] Kashtanov P V, Smirnov B M and Hippler R 2007 Magnetron plasma and nanotechnology *Phys.—Usp.* **50** 455–88

[22] Polonskyi O *et al* 2012 Nanocomposite metal/plasma polymer films prepared by means of gas aggregation cluster source *Thin Solid Films* **520** 4155–62

[23] Ganeva M, Pipa A V and Hippler R 2012 The influence of target erosion on the mass spectra of clusters formed in the planar dc magnetron sputtering source *Surf. Coat. Technol.* **213** 41–7

[24] Haberland H (ed) 1995 *Clusters of Atoms and Molecules I* (Berlin: Springer)

[25] Haberland H, Karrais M, Mall M and Thurner Y 1992 Thin films from energetic cluster impact: A feasibility study *J. Vac. Sci. Technol.* A **10** 3266–71

[26] Haberland H, Mall M, Moseler M, Qiang Y, Reiners T and Thurner Y 1994 Filling of micron-sized contact holes with copper by energetic cluster impact *J. Vac. Sci. Technol.* A **12** 2925–30

[27] Pratontep S, Carroll S J, Xirouchaki C, Streun M and Palmer R E 2005 Size-selected cluster beam source based on radio frequency magnetron plasma sputtering and gas condensation *Rev. Sci. Instrum.* **76** 045103

[28] Blazek J, Bartos P, Basner R and Kersten H 2011 Distribution of charge on clusters in a magnetron discharge *Proc. 30th ICPIG (Belfast, UK, 28 August–2 September 2011)*

[29] Kousal J, Polonskyi O, Kylian O, Choukourov A, Artemenko A, Pesicka J, Slavinska D and Biederman H 2013 Characterization of nanoparticle flow produced by gas aggregation source *Vacuum* **96** 32–8

[30] Hartmann H, Popok V N, Barke I, von Oeynhausen V and Meiwes-Broer K-H 2012 Design and capabilities of an experimental setup based on magnetron sputtering for formation and deposition of size-selected metal clusters on ultra-clean surfaces *Rev. Sci. Instrum.* **83** 073304

[31] Seidl M and Brack M 1996 Liquid drop model for charged spherical metal clusters *Ann. Phys.* **245** 275–310

[32] Austin W E, Holme A E and Leck J H 1995 The mass filter: design and performance *Quadrupole Mass Spectrometry and its Applications* (*American Vacuum Society Classics*) ed P H Dawson (Woodbury, NY: AIP Press) pp 121–152

[33] Bassi D 1988 Ionization detectors II: Mass selection and ion detection *Atomic and Molecular Beam Methods* ed G Scoles (Oxford: Oxford University Press) pp 180–92

[34] Oxford Applied Research *Quadrupole Mass Filter QMF200: QMF200 Operation and Maintenance*

[35] Smirnov B 2010 *Cluster Processes in Gases and Plasmas* (Berlin: Wiley)

[36] Smirnov B M 1994 Processes in expanding and condensing gases *Phys.—Usp.* **37** 621–57

[37] Smirnov B 2012 *Nanoclusters and Microparticles in Gases and Vapors* (Berlin: De Gruyter)

[38] Smirnov B 2012 *Fundamentals of Ionized Gases* (Weinheim: Wiley)

[39] Ganeva M, Peter T, Bornholdt S, Kersten H, Strunskus T, Zaporojtchenko V, Faupel F and Hippler R 2012 Mass spectrometric investigations of nano-size cluster ions produced by high pressure magnetron sputtering *Contrib. Plasma Phys.* **52** 881–9

[40] Sheridan T E, Goeckner M J and Goree J 1991 Observation of two-temperature electrons in a sputtering magnetron plasma *J. Vac. Sci. Technol.* A **9** 688–90

[41] Sigurjonsson P and Gudmundsson J T 2008 Plasma parameters in a planar dc magnetron sputtering discharge of argon and krypton *J. Phys.: Conf. Ser.* **100** 062018

[42] Rossnagel S M and Kaufman H R 1986 Langmuir probe characterization of magnetron operation *J. Vac. Sci. Technol.* A **4** 1822–5

[43] Rossnagel S M and Kaufman H R 1988 Current–voltage relations in magnetrons *J. Vac. Sci. Technol.* A **6** 223–9

[44] Goeckner M J, Goree J and Sheridan T E 1990 Laser-induced fluorescence characterization of ions in a magnetron plasma *J. Vac. Sci. Technol.* A **8** 3920–4

[45] Hippler R, Wrehde S, Stranak V, Zhigalov O, Steffen H, Tichy M, Quaas M and Wulff H 2005 Characterization of a magnetron plasma for deposition of titanium oxide and titanium nitride films *Contrib. Plasma Phys.* **45** 348–57

[46] Spatenka P, Leipner I, Vlcek J and Musil J 1997 A comparison of internal plasma parameters in a conventional planar magnetron and a magnetron with additional plasma confinement *Plasma Sources Sci. Technol.* **6** 46

[47] Petrov I, Orlinov V, Ivanov I and Kourtev J 1988 Electrostatic probe measurements in the glow discharge plasma of a d.c. magnetron sputtering system *Contrib. Plasma Phys.* **28** 157–67

[48] Seo S-H, In J-H and Chang H-Y 2004 Measurements of electron energy distribution functions and electron transport in the downstream region of an unbalanced dc magnetron discharge *Plasma Sources Sci. Technol.* **13** 409

4.5. Surface morphology and composition of films grown by size-selected Cu nanoclusters

Vacuum 83 (2009) 719–723

Contents lists available at ScienceDirect

Vacuum

journal homepage: www.elsevier.com/locate/vacuum

Surface morphology and composition of films grown by size-selected Cu nanoclusters

Abhijit Majumdar [a,*], Marina Ganeva [a], Daniel Köpp [a], Debasish Datta [b], Puneet Mishra [b], Satyaranjan Bhattacharayya [b], Debabrata Ghose [b], Rainer Hippler [a]

[a] Institut für Physik, Ernst-Moritz-Arndt-Universität Greifswald, Felix-Hausdorff-Strasse 6, 17489 Greifswald, Germany
[b] Surface Physics Division, Saha Institute of Nuclear Physics, 1/AF Bidhan Nagar, Kolkata 700 064, India

Keywords:
Cu nanocluster films
Si substrates
X-ray photoelectron spectroscopy

A B S T R A C T

We report the investigation of morphology and composition of copper nanocluster films deposited on Si substrates. The nanoclusters are formed in an aggregation tube at room temperature and magnetron sputtering source is used to get negatively charged Cu-clusters' beam which is subsequently mass-filtered to get size-selected cluster on the substrates as soft-landing process of deposition. For composition of the films, X-ray photoelectron spectroscopy (XPS) technique is used. For morphological changes of the films both scanning electron microscopy (SEM) and atomic force microscopy (AFM) analyses are carried out. Additionally, Energy Dispersive X-ray (EDX) spectra support the compositional and structural informations of the film. The analysis of Cu nanoclusters' films reveals that initial nucleation of Cu clusters takes place in the form of isolated islands and the arrival of subsequent Cu clusters onto Si substrates has preferential aggregation around the preceding clusters forming a mound structure.

1. Introduction

One of the recent trends of nanomaterials' research is the fabrication of thin films composed of nanometer size particles or clusters. Although the main purpose of such a research is aimed at its applications, the fundamental understanding of various aspects of thin film formation and its properties is of great importance. For example, substrate plays an important role in such films formation. The morphology of such films is another crucial factor to use the films in applications of nanomaterials. The production of nanocluster films using the plasma sputtering in the form of magnetron sputtering in combination of gas condensation techniques is being considered nowadays as one of the most controlled methods for such films formation [1]. Nanocluster films are also of strong interest to catalysis studies due to large surface to volume ratio that corresponds to the porous structure of films fabricated by soft landing nanoclusters onto a substrate. The formation of nanoparticles exhibits interesting magnetic, electronic and/or optoelectronic properties [2,3].

In the present work, we investigate the chemical properties (bond structure) and the surface morphology of the Cu nanoclusters that are produced in the form of negatively charged copper clusters in a source operated at room temperature and this low energy cluster beam is deposited on Si substrates to get soft landing films composed of mass selected clusters. There are a few reports on Cu nanocluster deposition [4–6]. In these studies, the scaling aspects are mainly dealt. In our studies we showed that Cu nanoclusters deposition in early stage is dominated by the nucleation of fractal structures that subsequently spread out to form a continuous film in the existing models of DDA (deposition diffusion aggregation) and DLA (diffusion limited aggregation) concepts of nanocluster thin film formation.

2. Experimental

Cu nanoclusters were deposited using DC magnetron sputtering technique of a commercially available NC 200 nanocluster source (Oxford Applied Research [3,7]). The base pressure in the deposition chamber was $\approx 7 \times 10^{-8}$ mbar. During magnetron sputtering with Ar gas the pressure was $\approx 3 \times 10^{-3}$ mbar. The discharge power during sputtering was 130 W (325 V, plasma current 0.4 A). The Ar flow rate is regulated by means of a mass flow controller (MKS Instruments) at a constant flow of 40 sccm (standard cubic centimeter). Clusters were formed by the attachment of free sputtered atoms and by coagulation processes inside the chilled water cooled aggregation tube. The energetic negatively charged clusters ions were passed through a mass filter (QMF 200) to obtain size-selected copper nanoclusters. In the present experiment, a cluster mass of 113,000 amu is selected. The number of Cu atoms in a cluster is found to be 1750 and the corresponding size

* Corresponding author.
E-mail address: majumdar@physik.uni-greifswald.de (A. Majumdar).

0042-207X/$ – see front matter © 2008 Elsevier Ltd. All rights reserved.
doi:10.1016/j.vacuum.2008.05.022

(diameter) of a cluster obtained from the quadrupole filter is 3.4 nm (with Wigner–Seitz radius of Cu atoms 0.141 nm).

Cu nanocluster was produced in the source using the mass filter attached with the system. After the films were prepared X-ray photoelectron spectroscopy was carried out with the as-deposited Cu nanocluster films. X-ray photoelectron spectroscopy (XPS) measurements of the Cu nanoclusters were performed on a VG Microtech (CLAM2: Multi-technique 100 mm hemispherical electron analyser) X-ray photoelectron spectroscope, using Mg Kα radiation (photon energy 1253 eV) as the excitation source and the binding energy (BE) of Au (Au $4f_{7/2}$: 84.00 eV) as the reference. The XPS spectra were collected in a constant analyser energy mode, at a chamber pressure of 10^{-8} mbar and pass energy of 23.5 eV at 0.125 eV/step. After the XPS analysis the Cu nanocluster films were examined by SEM with EDX (FEG ICON) facility. The SEM was employed for this investigation in a number of tilt angles to the sample surface to get an idea about the heights of the morphological features. The EDX spectra were taken both in the region and in the spot modes for 100 s in each case. The samples were then investigated by AFM (NanoScope IV, Veeco Instr., USA) in the tapping mode under ambient condition using Si tip with nominal radius of curvature 12 nm having resonance frequency 428 kHz. The images thus obtained were flattened using the software provided by this AFM.

3. Results and discussions

Quantitative analyses as well as chemical synthesis of the Cu nanoclusters' film have been done by XPS and the measurement gives the percentage amount of copper (including Cu $2p_{3/2}$, Cu $2p_{1/2}$, Cu $3p_{3/2}$, and Cu $3p_{1/2}$) as well as silicon and oxygen. Fig. 1 shows the full scale spectrum of the Cu nanocluster film. Cu 2p, Cu 3p, Si 2p, Si 2s and O 1s bonds have been observed in the XPS analysis. The detail analysis of the peaks Si 2p and O 1s is not discussed here. Si 2s peak is not discussed here, since the atomic scattering factor (ASF) is very less in case of Si 2s to perform quantitative peak analysis by spectral deconvolution method. Large amount of oxygen is appeared due to contamination of the air [8]. A clear image of the possible chemical bonds of copper can be deduced from a deconvolution of the individual Cu 2p and Cu 3p lines into Gaussian line shapes [8].

The deconvoluted XPS spectra of Cu 2p and Cu 3p are shown in Figs. 2 and 3. The best Gaussian fits to the XPS lines resulted in

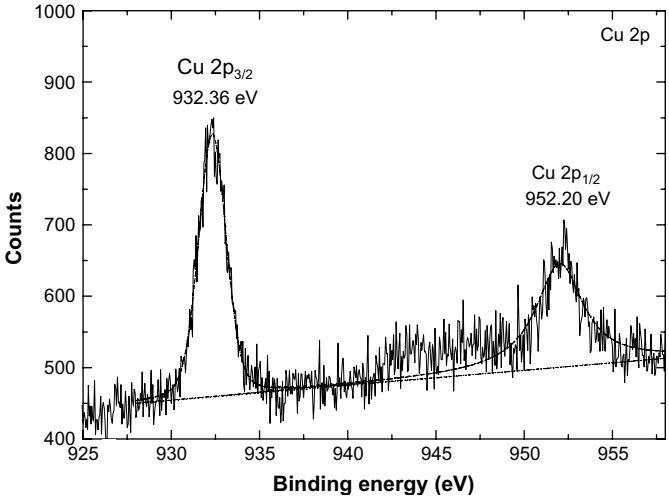

Fig. 2. Typical Cu 2p, XPS spectra of Cu nanoclusters' film deposited on Si substrate.

two different peaks for the Cu 2p line and two peaks for the Cu 3p line. Fig. 2 exhibits the peaks at 932.36 eV and 952.20 eV, which have been attributed to the Cu $2p_{3/2}$ and Cu $2p_{1/2}$ bonds, respectively. Similarly, from Fig. 3, the deconvoluted Cu 3p spectrum shows two peaks at 75.20 eV and 77.35 eV which have been assigned to Cu $3p_{3/2}$ and Cu $3p_{1/2}$ bonds, respectively [9]. Table 1 shows the peak position and the corresponding amount (%) of copper, oxygen, metal oxide, silicon, and silicon oxide in the deposited Cu nanocluster film. It has been found that copper is 13%, oxygen (total) 41%, metal oxide (CuO, oxygen bound to Cu) 11%, Si 26% and SiO (oxygen bound to Si) 9% in the deposited Cu nanocluster film. The approximated error bar of the calculated percentage amount of the chemical composition is about ±2%; depends on the XPS peak fitting parameters. Large amount of oxygen is adsorbed at the surface of the Si wafer and rest of oxygen is bound to Cu as well as to Si. Since it is ex situ measurement and the deposited Cu nanocluster film is oxidized due to air contamination.

Figs. 4–6, show the morphological behavior of Cu nanoclusters' films deposited on Si (100) substrates. Along with the

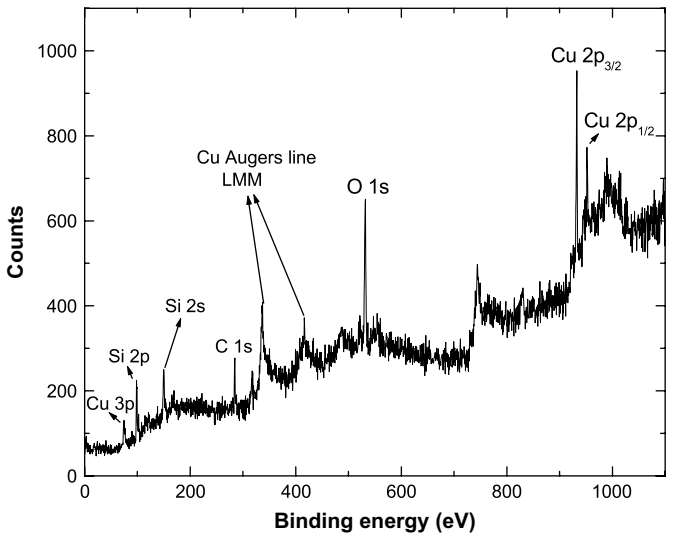

Fig. 1. Full scale spectrum of the Cu nanoclusters' film deposited on Si (100) substrate.

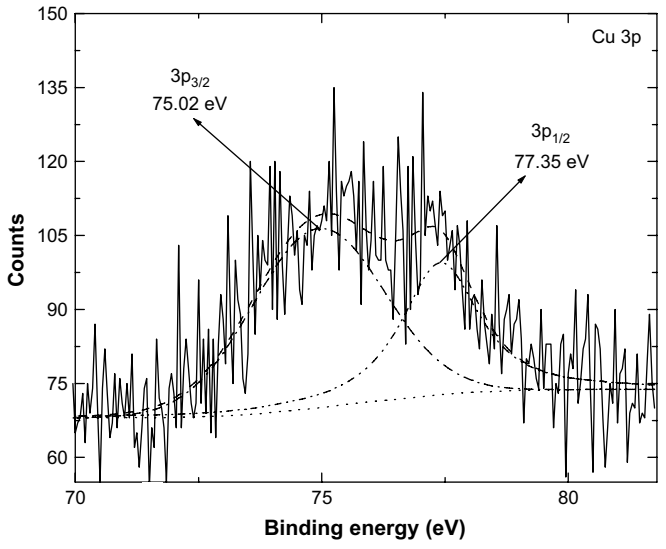

Fig. 3. Typical Cu 3p, XPS spectra of Cu nanoclusters' film deposited on Si substrate.

Table 1
Deconvoluted peak position and amount (%) of Cu (2p and 3p), O 1s and Si 2p obtained from XPS analysis

Peak	Peak position (eV)	Amount (%)
Cu $2p_{3/2}$	932.36	6
Cu $2p_{1/2}$	952.20	4
Cu $3p_{3/2}$	75.20	2
Cu $3p_{1/2}$	77.35	1
O 1s	531.95	41
Metal oxide (O bound to Cu)	530.35	11
Si	98.7	26
SiO (O bound to Si)	102.06	9

morphological studies, EDX spectra corresponding to the SEM images were taken at both region and spot modes. The SEM observation of Cu nanoclusters' films reveals that initial nucleation of Cu clusters takes place in the form of isolated island and the arrival of subsequent Cu clusters onto Si substrates has preferential aggregation around the preceding clusters forming a structure as seen in Fig. 4(a). The image of this figure shows that some parts are locally populated by Cu clusters (white contrast in the images), while the remaining (black region) portions are still Si rich. Some tiny clusters islands are also seen in the image. The morphology of these samples also shows irregular cluster islands with varied size distributions. The EDX spectra were taken from a white contrast region, where Cu rich clusters are presumably considered. The EDX pattern clearly shows only a stress signature of Cu has arrived at the region as shown in Fig. 4(a). During the deposition of Cu clusters there was a slight variation of thickness of the Cu film. However, Fig. 4(a) was taken on the perimeter of the deposited Cu film. Fig. 5(a) shows an image taken from the central part of the deposited film and here Cu islands are more prominent. This is also substantiated by the EDX spectra shown in Fig. 5(b), where Cu signal is more pronounced than that of the spectra in Fig. 6(b). However, this EDX spectrum was taken in the spot mode as indicated in Fig. 5(a) by an arrow. A closer observation shows that due to electron bombardment the cluster was deformed and took an elongated shape. In order to get more information from the SEM images we examined the Cu nanocluster film at tilt angles in the SEM observations. Fig. 6(a), shows such an image at relatively lower magnification. The morphology as seen in this image clearly shows a fractal kind of cluster evolution on Si substrate. When this image is magnified we observed the morphology as shown in Fig. 6(b), where Cu clusters are prominently seen on Si substrate. This image was taken at a tilt angle of 40°. From this image one can get some idea about the height of the clusters apart from the spatial dimension of the clusters so formed.

Atomic force microscopy (AFM) analysis of the Cu nanocluster films was carried out to investigate the morphology and to obtain information about the height of the Cu nanoclusters agglomerated on the Si substrate. Fig. 7(a) and (b) shows the morphology of the film examined by AFM in tapping mode under ambient condition. Analysis of the AFM images shows that the average height of the islands are about 17 nm, where we found diameters of these islands are about 80 nm from SEM images (Fig. 6(b)). This means that the clusters have coagulated on the substrate surface.

Three physical phenomena arise [9] when clusters are deposited on a substrate. These are (i) deposition of clusters, (ii) diffusion of clusters on the surface and (iii) interaction of the deposited clusters. Initially, as nanoclusters arrive on a substrate, the surface coverage remains low. Subsequently, the already deposited clusters along with other clusters are diffused to form islands on the substrate. Careful observations of SEM as well as AFM images reveal that the character of cluster attachment to the Si surface is similar to that in the case of formation of fractal structures when solid particles attach to a surface and can move over it. This mechanism of joining of solid particles on a surface, in accordance with the DLA model (diffusion limited aggregation) [10–13] or DDA model (deposition diffusion aggregation) [14], accounts for diffusion motion of particles on the surface. This model developed under various conditions was analyzed [15] and can be applied to the present case. According to DLA model, a cluster is assembled by adding individual particles to it. A definite number of particles are introduced into the formation region initially and the particles coalesce when they collide with one another. This will initially result in the appearance of a larger number of smaller clusters, and subsequent collisions will lead to their aggregation. In the morphology represented by Figs. 4–6, joining of clusters takes place and these connected clusters form fractal structures, i.e., fractal clusters, as seen more prominently in Fig. 6(a).

4. Conclusion

We have investigated the morphological and chemical aspects of Cu nanocluster films deposited onto silicon substrate at room temperature. Cu 2p, Cu 3p, Si 2p, Si 2s and O 1s bonds have been observed in the XPS analysis. XPS analysis reveals that the Cu nanoclusters' film composed of 12.65% of Cu, 41.28% of oxygen, 10.50% of metal oxide, 26.43% of Si 2p and 9.13% of Si O. Moreover it is observed that, the Cu nanoclusters' film is highly oxidized. The morphology shows that clusters are diffused on the surface to form

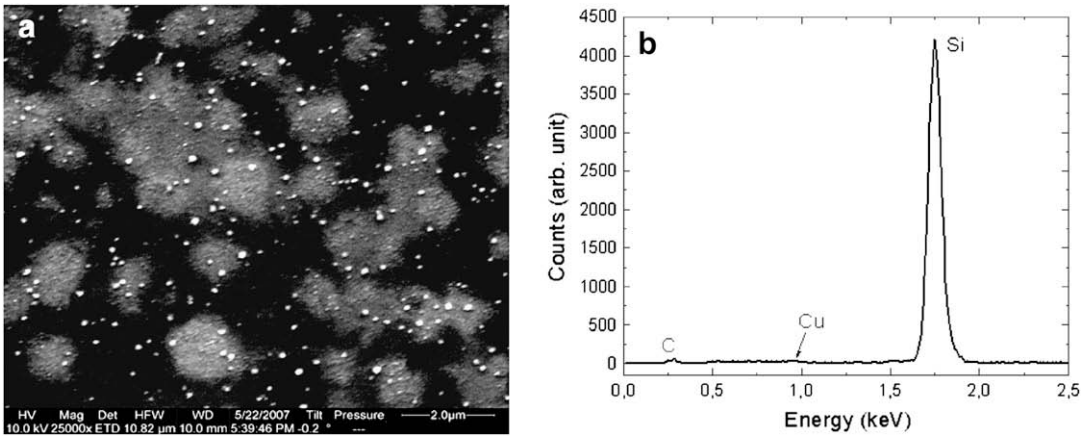

Fig. 4. Scanning electron micrograph of the size-selected (diameter = 3.4 nm) Cu nanoclusters' film deposited on Si substrate at relatively lower magnification and (b) its corresponding EDX pattern in the region mode.

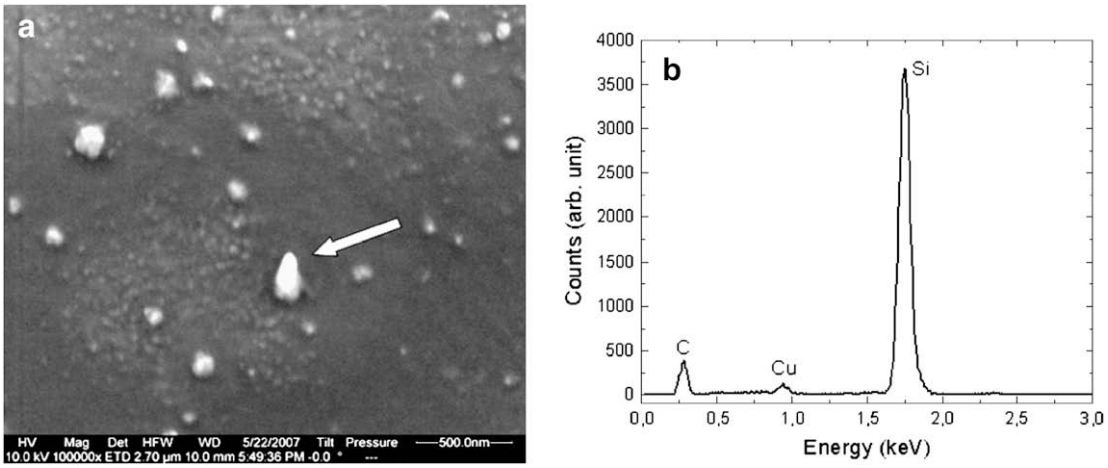

Fig. 5. Scanning electron micrograph of the size-selected (diameter = 3.4 nm) Cu nanoclusters' film deposited on Si substrate and (b) its corresponding EDX pattern in the spot mode. The spot is indicated by the arrow and it may be noted that the spot is melted due to electron bombardment (about 100 s) and the feature is elongated.

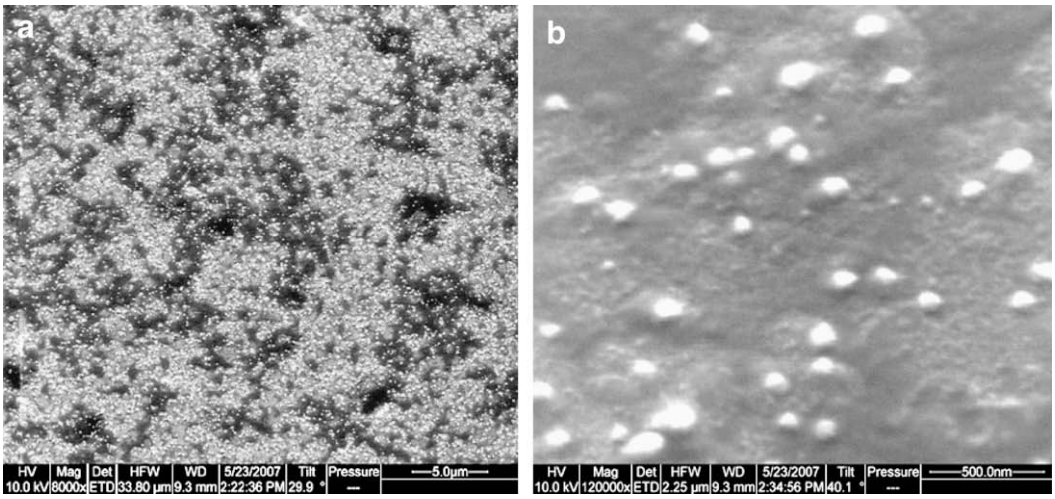

Fig. 6. Scanning electron micrograph of the size-selected (diameter = 3.4 nm) Cu nanoclusters' film deposited on Si substrate at tilt angle of 30° at a lower magnification. (b) SEM on the same region at higher magnification at a tilt angle of 40°.

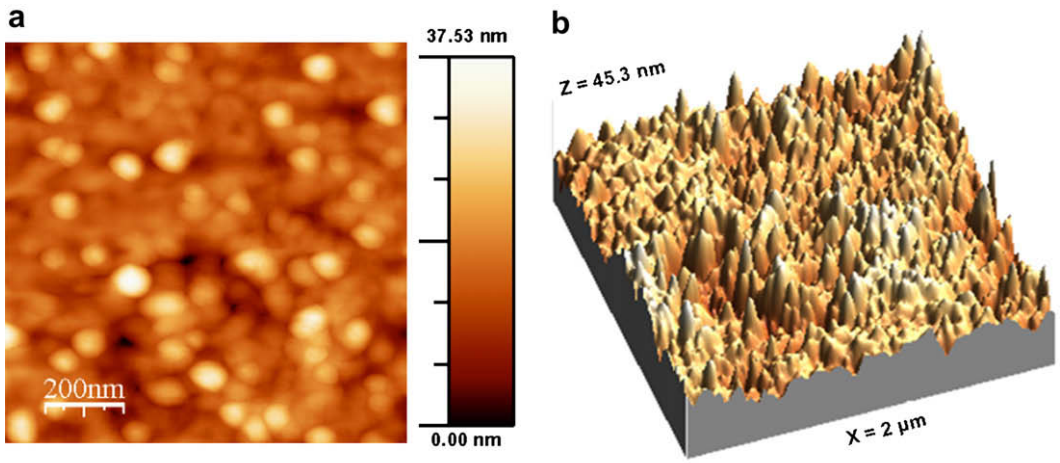

Fig. 7. Atomic force microscopy analysis of Cu nanocluster (diameter = 3.4 nm) deposited on Si substrate, showing (a) two-dimensional image with RMS roughness of 4.7 nm and average height of 15.2 nm and (b) three-dimensional image with RMS roughness of 5.4 nm and average height of 23.7 nm. These images ((a) and (b)) were taken from two regions of the deposited films.

fractal-like structure and the flattening takes place as a result of impact energy of the clusters.

Acknowledgements

Part of this work was supported by the Deutsche Forschungsgemeinschaft through SFB/TR 24. We are thankful to Prof. Tapas K. Chini for several discussions and SEM measurement.

References

[1] Pratontep S, Carrol SJ, Xirouchaki C, Streun M, Palmer RE. Rev Sci Instrum 2005;76:045103.
[2] Haberland H, Mosseler M, Qiang Y, Rattude O, Reiners T, Thunrner Y. Surf Rev Lett 1996;3:887.
[3] Haberland H, Karrais M, Mall M, Thurner Y. J Vac Sci Technol A 1992;10:3266.
[4] Palasantzas G, Koch SA, De Hosson JThM. Appl Phys Lett 2002;81:1090.
[5] Palasantzas G, Koch SA, De Hosson JThM. Rev Adv Mater Sci 2003;5:57.
[6] Shin D-W, Wang SX, Marshall AF, Kimura W, Dong C, Augustsson A, et al. Thin Solid Films 2005;473:267.
[7] For the details of our deposition system see: <http://www.oaresearch.co.uk/cluster.htm>.
[8] Moulder JF, Stickle WF, Sobol PE, Bomben KD. Handbook of X-ray photoelectron spectroscopy. Perkin–Elmer Corporation; 1992.
[9] Melinon P, Paillard V, Dupuis V, Perez A, Jensen P, Hoareau A, et al. Int J Mod Phys B 1995;9:339.
[10] Witten TA, Sander IM. Phys Rev Lett 1981;47:1400.
[11] Meakin P. Phys Rev A 1983;27:604.
[12] Meakin P. Phys Rev A 1983;27:1495.
[13] Sahimi M, McKarnin M, Nordahl T, Tirrell M. Phys Rev A 1985;32:590.
[14] Jensen P, Barabasi AL, Larralde H, Havlin S, Stanley HE. Phys Rev B 1994;50:15316.
[15] Smirnov BM. The properties of fractal clusters. Phys Rep 1990;188:1.

Chapter 5

Summary

Nano-size silver and copper clusters were produced with a DC magnetron-based gas aggregation source. The typical mass of the studied clusters was in the range of 10^4 atoms for copper clusters, and in the range of 10^3 atoms for silver clusters. The processes of cluster formation, cluster charging and cluster flow were investigated. The results of this study can be summarized as follows.

1. **Mass spectra.** The dependencies of the mass spectra of silver clusters on the buffer gas constitution (i.e. the He:Ar ratio), the discharge power, and the Ar flow rate were investigated [Ganeva et al., CPP 52, (2012)]. These were compared to the dependencies found in the TEM study of deposited films. The current study revealed that
   - the high-pressure nanocluster source produces clusters of diameter in the range of 3–20 nm, but QMF limits allow to detect only cluster ions with diameter of 3–8 nm;
   - an increase in the He:Ar ratio results in a narrower mass spectra with a smaller most probable cluster size;
   - an increase in the Ar flow rate leads to a higher cluster intensity and a slight increase in the most probable cluster size.
2. **Cluster velocity.** The ion velocity distribution functions (IVDFs) of mass selected nano-size copper clusters accelerated by an outflowing gas were investigated [Ganeva et al., PSST 22, (2013)]. IVDFs of positive and negative cluster ions with a size in the range of 510 nm were measured at different experimental conditions. Such measurements, to my knowledge, have not been performed by other researchers so far. Following has been revealed.
   - The obtained value for the most probable cluster velocity is in the range of about 80–180 m/s depending on the experimental conditions and the cluster size. Thus, clusters deposit to the substrate in a soft-landing regime.
   - The IVDFs of clusters with a size of 5 nm allows to suggest two cluster groups with different most probable velocities.

- The most probable velocities of positively charged clusters are slightly higher than those of negatively charged clusters. This suggests a potential drop $\Delta V \approx -4$ V near the chamber walls in the orifice vicinity.
- A comparison of the measured cluster velocities to those predicted by the theoretical model resulted in a further cluster acceleration after transition through the orifice, which is not predicted by the theoretical model.
- The measured cluster velocities allow for evaluation of the cluster size distribution function from the mass spectra. This is an important result for further research on the processes underlying cluster formation.

3. **Cluster charge**. The nanocluster source produces positively and negatively charged cluster ions. The ratio between positively and negatively charged clusters was estimated from measurements with a biased quadrupole mass filter (QMF) detection plate for silver clusters [Ganeva et al., CPP 52, (2012)], and evaluated from the measured IVDFs for copper clusters [Ganeva et al., PSST 22, (2013)].
   - For the high pressure nanocluster source investigated in [Ganeva et al., CPP 52, (2012)] the N_+/N_- ratio is in the range of 0.2-1.5.
   - For the experimental conditions in [Ganeva et al., PSST 22, (2013)], the N_+/N_- ratio is about 0.5.
   - Comparing the obtained N_+/N_- ratio with the ratio in the theoretical model allows us to assess the electron temperature T_e in the secondary plasma in the aggregation region as well as N_i/N_e [Ganeva et al., PSST 22, (2013)]. The estimated $T_e \approx 0.2$ eV is in good agreement with results of other researchers and $N_i/N_e \approx 220$ is within the plausible range.
4. During the cluster beam characterization, a shift of the mass spectra in time was noted [Majumdar, Köpp, Ganeva et al., RSI 80 (2009)], while all of the experimental conditions were kept constant. This effect, which so far has not been described by previous researchers, was systematically investigated and quantitatively characterized [Ganeva et al., Surf&Coat 213, (2012)]. The results reveal that mass spectra are dramatically influenced by the magnetron target lifetime. Hence, for the production of a cluster beam with a stable and reproducible size distribution, consideration of the target lifetime is crucial.
5. Analysis of the morphology of the deposited monolayer films [Ganeva et al., CPP 52, (2012)] revealed that no fractal structures are formed in the cluster beam. Consequently, the cluster aggregation process is negligible and can be excluded from the gas aggregation sources considered here. This means that cluster growth in the aggregation region is governed by one of three main processes: atom attachment, coagulation, coalescence — or by a combination of these processes.

To conclude, the results of the present work include an experimental and theoretical investigation of the effects, which are of great importance for the production of thin cluster films, as well as for the generation of cluster beams with the desired properties.

Bibliography

[1] Hellmut Haberland, editor. *Clusters of atoms and molecules I.* Springer Verlag Berlin Heidelberg, 1995.

[2] Pablo Jensen. Growth of nanostructures by cluster deposition: Experiments and simple models. *Reviews of Modern Physics*, 71(5):1695–1735, Oct 1999.

[3] Alexis T. Bell. The impact of nanoscience on heterogeneous catalysis. *Science*, 299(5613):1688–1691, 2003.

[4] M. Valden, X. Lai, and D. W. Goodman. Onset of catalytic activity of gold clusters on titania with the appearance of nonmetallic properties. *Science*, 281(5383):1647–1650, 1998.

[5] Claude R. Henry. Catalysis by nanoparticles. In Ulrich Heiz and Uzi Landman, editors, *Nanocatalysis*, NanoScience and Technology, pages 245–268. Springer Berlin Heidelberg, 2007.

[6] B. Mishra, Bhavesh B. Patel, and Sanjay Tiwari. Colloidal nanocarriers: a review on formulation technology, types and applications toward targeted drug delivery. *Nanomedicine: Nanotechnology, Biology and Medicine*, 6(1):9–24, 2010.

[7] Tarek M. Fahmy, Peter M. Fong, Amit Goyal, and W. Mark Saltzman. Targeted for drug delivery. *Materials Today*, 8(8, Supplement):18–26, 2005.

[8] Jun Sung Kim, Eunye Kuk, Kyeong Nam Yu, Jong-Ho Kim, Sung Jin Park, Hu Jang Lee, So Hyun Kim, Young Kyung Park, Yong Ho Park, Cheol-Yong Hwang, Yong-Kwon Kim, Yoon-Sik Lee, Dae Hong Jeong, and Myung-Haing Cho. Antimicrobial effects of silver nanoparticles. *Nanomedicine: Nanotechnology, Biology and Medicine*, 3(1):95–101, 2007.

[9] Guogang Ren, Dawei Hu, Eileen W.C. Cheng, Miguel A. Vargas-Reus, Paul Reip, and Robert P. Allaker. Characterisation of copper oxide nanoparticles for antimicrobial applications. *International Journal of Antimicrobial Agents*, 33(6):587–590, 2009.

[10] Davide Brambilla, Benjamin Le Droumaguet, Julien Nicolas, S. Hossein Hashemi, Lin-Ping Wu, S. Moein Moghimi, Patrick Couvreur, and Karine Andrieux. Nanotechnologies for alzheimer's disease: diagnosis, therapy, and safety issues. *Nanomedicine: Nanotechnology, Biology and Medicine*, 7(5):521–540, 2011.

[11] Nicola Cioffi, Luisa Torsi, Nicoletta Ditaranto, Giuseppina Tantillo, Lina Ghibelli, Luigia Sabbatini, Teresa Bleve-Zacheo, Maria D'Alessio, P. Giorgio Zambonin, and Enrico Traversa. Copper nanoparticle/polymer composites with antifungal and bacteriostatic properties. *Chemistry of Materials*, 17(21):5255–5262, 2005.

[12] Thorsten Ressler, Benjamin L. Kniep, Igor Kasatkin, and Robert Schlögl. The microstructure of copper zinc oxide catalysts: Bridging the materials gap. *Angewandte Chemie International Edition*, 44(30):4704–4707, 2005.

[13] Sascha Vukojevic, Oliver Trapp, Jan-Dierk Grunwaldt, Christoph Kiener, and Ferdi Schüth. Quasi-homogeneous methanol synthesis over highly active copper nanoparticles. *Angewandte Chemie International Edition*, 44(48):7978–7981, 2005.

[14] Jose Ruben Morones, Jose Luis Elechiguerra, Alejandra Camacho, Katherine Holt, Juan B Kouri, Jose Tapia Ramrez, and Miguel Jose Yacaman. The bactericidal effect of silver nanoparticles. *Nanotechnology*, 16(10):2346, 2005.

[15] O. Polonskyi, P. Solar, O. Kylian, M. Drabik, A. Artemenko, J. Kousal, J. Hanus, J. Pesicka, I. Matolinova, E. Kolibalova, D. Slavinska, and H. Biederman. Nanocomposite metal/plasma polymer films prepared by means of gas aggregation cluster source. *Thin Solid Films*, 520(12):4155–4162, 2012.

[16] P. Solar, O. Polonskyi, A. Choukourov, A. Artemenko, J. Hanus, H. Biederman, and D. Slavinska. Nanostructured thin films prepared from cluster beams. *Surface and Coatings Technology*, 205:S42–S47, 2011.

[17] T. Peter, M. Wegner, V. Zaporojtchenko, T. Strunskus, S. Bornholdt, H. Kersten, and F. Faupel. Metal/polymer nanocomposite thin films prepared by plasma polymerization and high pressure magnetron sputtering. *Surface and Coatings Technology*, 205:S38–S41, 2011.

[18] F. Faupel, V. Zaporojtchenko, H. Greve, U. Schrmann, V. S. K. Chakravadhanula, Ch. Hanisch, A. Kulkarni, A. Gerber, E. Quandt, and R. Podschun. Deposition of nanocomposites by plasmas. *Contributions to Plasma Physics*, 47(7):537–544, 2007.

[19] Franz Faupel, Vladimir Zaporojtchenko, Thomas Strunskus, and Mady Elbahri. Metal-polymer nanocomposites for functional applications. *Advanced Engineering Materials*, 12(12):1177–1190, 2010.

[20] M. Di Vece, S. Palomba, and R. E. Palmer. Pinning of size-selected gold and nickel nanoclusters on graphite. *Phys. Rev. B*, 72:073407, Aug 2005.

[21] S. J. Carroll, S. Pratontep, M. Streun, R. E. Palmer, S. Hobday, and R. Smith. Pinning of size-selected ag clusters on graphite surfaces. *J. Chem. Phys.*, 113(18):7723–7727, 2000.

[22] Dieter Vollath. *Nanomaterials. An introduction to Synthesis, Properties and Applications.* WILEY-VCH, Weinheim, 2008.

[23] A. S. Edelstein and R. C. Cammarata, editors. *Nanomaterials: Synthesis, Properties and Applications.* Institute of Physics Publishing Bristol and Philadelphia, 1996.

[24] T. Theivasanthi and M. Alagar. Studies of copper nanoparticles effects on microorganisms. *Annals of Biological Research*, 2(3):368–373, 2011.

[25] R.S. Berry and R. D. Levine. Survey of structure, energetics and dynamics of clusters. In Tamotsu Kondow and Fumitaka Mafune, editors, *Progress in Experimentsl and Theoretical Studies of Clusters*, Advanced Series in Physical Chemistry - Vol. 13, pages 1–77. World Scientific Publishing, 2003.

[26] A. Terasaki. Physical and chemical properties of metal clusters in the gas phase and on solid surfaces. In Tamotsu Kondow and Fumitaka Mafune, editors, *Progress in Experimentsl and Theoretical Studies of Clusters*, Advanced Series in Physical Chemistry - Vol. 13, pages 121–154. World Scientific Publishing, 2003.

[27] Ulrich Schürmann, Whitney Hartung, Haile Takele, Vladimir Zaporojtchenko, and Franz Faupel. Controlled syntheses of agpolytetrafluoroethylene nanocomposite thin films by co-sputtering from two magnetron sources. *Nanotechnology*, 16(8):1078, 2005.

[28] Humberto Lara, Nilda Ayala-Nez, Liliana Ixtepan Turrent, and Cristina Rodrguez Padilla. Bactericidal effect of silver nanoparticles against multidrug-resistant bacteria. *World Journal of Microbiology and Biotechnology*, 26:615–621, 2010.

[29] Chun-Nam Lok, Chi-Ming Ho, Rong Chen, Qing-Yu He, Wing-Yiu Yu, Hongzhe Sun, Paul Tam, Jen-Fu Chiu, and Chi-Ming Che. Silver nanoparticles: partial oxidation and antibacterial activities. *Journal of Biological Inorganic Chemistry*, 12:527–534, 2007.

[30] Hengfeng Gong, Wei Lu, Lumin Wang, Gongping Li, and Shixun Zhang. The effect of deposition velocity and cluster size on thin film growth by cu cluster deposition. *Computational Materials Science*, 65:230–234, 2012.

[31] Vladimir N. Popok, Ingo Barke, Eleanor E.B. Campbell, and Karl-Heinz Meiwes-Broer. Cluster-surface interaction: From soft landing to implantation. *Surface Science Reports*, 66(10):347–377, 2011.

[32] Michael Moseler, Oliver Rattunde, Johannes Nordiek, and Hellmut Haberland. On the origin of surface smoothing by energetic cluster impact: Molecular dynamics simulation and mesoscopic modeling. *Nuclear Instruments and Methods in Physics Research Section B: Beam Interactions with Materials and Atoms*, 164165(0):522–536, 2000.

[33] Hellmut Haberland, Zinetulla Insepov, and Michael Moseler. Molecular-dynamics simulation of thin-film growth by energetic cluster impact. *Phys. Rev. B*, 51:11061–11067, Apr 1995.

[34] Y. Qiang, Y. Thurner, Th. Reiners, O. Rattunde, and H. Haberland. Hard coatings (tin, tixal1xn) deposited at room temperature by energetic cluster impact. *Surface and Coatings Technology*, 100–101:27–32, 1998.

[35] Grigorii N Makarov. Kinetic methods for measuring the temperature of clusters and nanoparticles in molecular beams. *Physics-Uspekhi*, 54(4):351–370, 2011.

[36] G. N. Makarov. Cluster temperature. methods for its measurement and stabilization. *Physics-Uspekhi*, 51(4):319–353, 2008.

[37] Paolo Milani and Salvatore Iannotta. *Cluster Beam Synthesis of Nanostructured Materials*. Springer, 1999.

[38] John A. Blackman, editor. *Metallic Nanoparticles*. Elsevier, 2009.

[39] John A. Thornton and Alan S. Penfold. Cylindrical magnetron sputtering. In John L. Vossen and Werner Kern, editors, *Thin film processes*, pages 75–113. Academic Press, Inc., 24–28 Oval Road, London NW1 7DX, 1978.

[40] Robert K. Waits. Planar magnetron sputtering. In John L. Vossen and Werner Kern, editors, *Thin film processes*, pages 131–173. Academic Press, Inc., 24–28 Oval Road, London NW1 7DX, 1978.

[41] Hellmut Haberland, Martin Karrais, Martin Mall, and Yonca Thurner. Thin films from energetic cluster impact: A feasibility study. *J. Vac. Sci. Technol. A*, 10(5):3266–3271, 1992.

[42] Hellmut Haberland, Martin Mall, Michael Moseler, You Qiang, Thomas Reiners, and Yonca Thurner. Filling of micron-sized contact holes with copper by energetic cluster impact. *J. Vac. Sci. Technol. A*, 12(5):2925–2930, 1994.

[43] S. Pratontep, S. J. Carroll, C. Xirouchaki, M. Streun, and R. E. Palmer. Size-selected cluster beam source based on radio frequency magnetron plasma sputtering and gas condensation. *Rev. Sci. Instrum.*, 76(4):045103, 2005.

[44] M. Ganeva, A.V. Pipa, and R. Hippler. The influence of target erosion on the mass spectra of clusters formed in the planar dc magnetron sputtering source. *Surface and Coatings Technology*, 213:41–47, 2012.

[45] M. Ganeva, T. Peter, S. Bornholdt, H. Kersten, T. Strunskus, V. Zaporojtchenko, F. Faupel, and R. Hippler. Mass spectrometric investigations of nano-size cluster ions produced by high pressure magnetron sputtering. *Contributions to Plasma Physics*, 52(10):881–889, 2012.

[46] Thomas Welzel and Klaus Ellmer. The influence of the target age on laterally resolved ion distributions in reactive planar magnetron sputtering. *Surface and Coatings Technology*, 205, Supplement 2(0):S294 – S298, 2011.

[47] Brian Chapman. *Glow Discharge Processes. Sputtering and Plasma Etching.* John Wiley and Sons, Inc., 1980.

[48] R De Gryse, D Depla, S Mahieu, and J Haemers. Rotatable magnetron sputtering: downscaling for better understanding. *Materials Technology: Advanced Performance Materials*, 26(1):3–9, 2011.

[49] R. De Gryse, J. Haemers, W.P. Leroy, and D. Depla. Thirty years of rotatable magnetrons. *Thin Solid Films*, 520(18):5833–5845, 2012.

[50] R. Kukla, T. Krug, R. Ludwig, and K. Wilmes. A highest rate self-sputtering magnetron source. *Vacuum*, 41(79):1968–1970, 1990.

[51] C. B. Garrett, 1984. US Patent No 4 444 643.

[52] Jindrich Musil, Jaroslav Vlcek, and Pavel Baroch. Magnetron discharges for thin films plasma processing. In Yves Pauleau, editor, *Materials Surface Processing by Directed Energy Techniques*, pages 67–110. Elsevier, 2006.

[53] G. Bräuer, B. Szyszka, M. Vergöhl, and R. Bandorf. Magnetron sputtering — milestones of 30 years. *Vacuum*, 84(12):1354–1359, 2010.

[54] I. Pilch, D. Söderström, N. Brenning, and U. Helmersson. Size-controlled growth of nanoparticles in a highly ionized pulsed plasma. *Applied Physics Letters*, 102(3):033108, 2013.

[55] Vitezslav Stranak, Stephan Block, Steffen Drache, Zdenek Hubicka, Christiane A. Helm, Lubomir Jastrabik, Milan Tichy, and Rainer Hippler. Size-controlled formation of cu nanoclusters in pulsed magnetron sputtering system. *Surface and Coatings Technology*, 205(8–9):2755–2762, 2011.

[56] A. Ayesh, S. Thaker, N. Qamhieh, and H. Ghamlouche. Size-controlled pd nanocluster grown by plasma gas-condensation method. *Journal of Nanoparticle Research*, 13:1125–1131, 2011.

[57] Ales Marek, Jan Valter, Stanislav Kadlec, and Jiri Vyskocil. Gas aggregation nanocluster source reactive sputter deposition of copper and titanium nanoclusters. *Surface and Coatings Technology*, 205:S573–S576, 2011.

[58] M. Gracia-Pinilla, E. Martnez, G. Vidaurri, and E. Prez-Tijerina. Deposition of size-selected cu nanoparticles by inert gas condensation. *Nanoscale Research Letters*, 5:180–188, 2010.

[59] A.N. Banerjee, R. Krishna, and B. Das. Size controlled deposition of cu and si nano-clusters by an ultra-high vacuum sputtering gas aggregation technique. *Applied Physics A: Materials Science and Processing*, 90:299–303, 2008.

[60] Omar Kamalou, Jimmy Rangama, Jean-Marc Ramillon, Patrick Guinement, and Bernd A. Huber. Production of pulsed, mass-selected beams of metal and semiconductor clusters. *Rev. Sci. Instr.*, 79(6):063301, 2008.

[61] I. Shyjumon, M. Gopinadhan, O. Ivanova, M. Quaas, H. Wulff, C. A. Helm, and R. Hippler. Structural deformation, melting point and lattice parameter studies of size selected silver clusters. *The European Physical Journal D - Atomic, Molecular, Optical and Plasma Physics*, 37:409–415, 2006.

[62] Ibrahimkutty Shyjumon, Manesh Gopinadhan, Christiane A. Helm, Boris M. Smirnov, and Rainer Hippler. Deposition of titanium/titanium oxide clusters produced by magnetron sputtering. *Thin Solid Films*, 500(1-2):41–51, 2006.

[63] Abhijit Majumdar, Marina Ganeva, Daniel Köpp, Debasish Datta, Puneet Mishra, Satyaranjan Bhattacharayya, Debabrata Ghose, and Rainer Hippler. Surface morphology and composition of films grown by size-selected cu nanoclusters. *Vacuum*, 83(4):719–723, 2008.

[64] Abhijit Majumdar, Daniel Köpp, Marina Ganeva, Debasish Datta, Satyaranjan Bhattacharyya, and Rainer Hippler. Development of metal nanocluster ion source based on dc magnetron plasma sputtering at room temperature. *Review of Scientific Instruments*, 80(9):095103, 2009.

[65] David T. Wu. Nucleation theory. volume 50 of *Solid State Physics*, pages 37–187. Academic Press, 1996.

[66] V.I. Kalikmanov. Classical nucleation theory. In *Nucleation Theory*, volume 860 of *Lecture Notes in Physics*, pages 17–41. Springer Netherlands, 2013.

[67] L. Granasy. Comparison of modern theories of vapor condensation. *AIP Conference Proceedings*, 534(1):209–212, 2000.

[68] L. D. Landau and E. M. Lifshitz. *Physical Kinetics*, volume 10 of *Course of theoretical physics*. Pergamon Press, Oxford, 1981.

[69] B. M. Smirnov. Processes involving clusters and small particles in a buffer gas. *Physics-Uspekhi*, 54(7):691–721, 2011.

[70] L. D. Landau and E. M. Lifshitz. *Statistical Physics*, volume 5 of *Course of theoretical physics*. Pergamon Press, Oxford, 1980.

[71] P. V. Kashtanov, B. M. Smirnov, and R. Hippler. Magnetron plasma and nanotechnology. *Physics-Uspekhi*, 50(5):455–488, 2007.

[72] Boris M. Smirnov, Ibrahimkutty Shyjumon, and Rainer Hippler. Flow of nanosize cluster-containing plasma in a magnetron discharge. *Phys. Rev. E*, 75:066402, Jun 2007.

[73] P.V. Kashtanov and B.M. Smirnov. Nanoclusters: Properties and processes. *High Temperature*, 48:846–859, 2010.

[74] Boris Smirnov. *Nanoclusters and Microparticles in Gases and Vapors*. Germany: De Gruyter, 2012.

[75] I.M. Lifshitz and V.V. Slyozov. The kinetics of precipitation from supersaturated solid solutions. *Journal of Physics and Chemistry of Solids*, 19(1–2):35–50, 1961.

[76] D. Weaire and S. Mcmurry. Some fundamentals of grain growth. volume 50 of *Solid State Physics*, pages 1–36. Academic Press, 1996.

[77] M. Seidl and M. Brack. Liquid drop model for charged spherical metal clusters. *Annals of Physics*, 245(2):275 – 310, 1996.

[78] C. G. Granqvist and R. A. Buhrman. Ultrafine metal particles. *Journal of Applied Physics*, 47(5):2200–2219, 1976.

[79] Boris Briehl and Herbert M. Urbassek. Monte carlo simulation of growth and decay processes in a cluster aggregation source. *Journal of Vacuum Science & Technology A: Vacuum, Surfaces, and Films*, 17(1):256–265, 1999.

[80] L. Rosenthal, A. Filinov, M. Bonitz, V. Zaporojtchenko, and F. Faupel. Diffusion and growth of metal clusters in nanocomposites: A kinetic monte carlo study. *Contributions to Plasma Physics*, 51(10):971–980, 2011.

[81] N Lümmen and T Kraska. Investigation of the formation of iron nanoparticles from the gas phase by molecular dynamics simulation. *Nanotechnology*, 15(5):525, 2004.

[82] M. Bonitz, L. Rosenthal, K. Fujioka, V. Zaporojtchenko, F. Faupel, and H. Kersten. Towards a particle based simulation of complex plasma driven nanocomposite formation. *Contributions to Plasma Physics*, 52(10):890–898, 2012.

[83] Marina Ganeva, Andrei V Pipa, Boris M Smirnov, Pavel V Kashtanov, and Rainer Hippler. Velocity distribution of mass-selected nano-size cluster ions. *Plasma Sources Science and Technology*, 22(4):045011, 2013.

[84] Felix Sharipov. Numerical simulation of rarefied gas flow through a thin orifice. *Journal of Fluid Mechanics*, 518:35–60, 2004.

[85] W. Jitschin, M. Ronzheimer, and S. Khodabakhshi. Gas flow measurement by means of orifices and venturi tubes. *Vacuum*, 53(12):181–185, 1999.

[86] Wolfgang Jitschin. Gas flow measurement by the thin orifice and the classical venturi tube. *Vacuum*, 76(1):89–100, 2004.

[87] N. Hadacek, J.P. Prin, and F. Viargues. Pressure drop for a rarefied-gas flow through a tube with a thermal gradient at low temperature. *Vacuum*, 60(1-2):85–88, 2001.

[88] Takashi Abe. Rarefied gas flow analysis by direct simulation monte carlo method in body-fitted coordinate system. *Journal of Computational Physics*, 83(2):424–432, 1989.

[89] Oleg Sazhin. Pressure-driven flow of rarefied gas through a slit at a various pressure ratios. *Journal of Vacuum Science & Technology A: Vacuum, Surfaces, and Films*, 30(2):021603, 2012.

[90] S. Varoutis, D. Valougeorgis, O. Sazhin, and F. Sharipov. Rarefied gas flow through short tubes into vacuum. *Journal of Vacuum Science & Technology A: Vacuum, Surfaces, and Films*, 26(2):228–238, 2008.

[91] Felix Sharipov. Transient flow of rarefied gas through a short tube. *Vacuum*, 90:25–30, 2013.

[92] Felix Sharipov. Transient flow of rarefied gas through an orifice. *Journal of Vacuum Science & Technology A: Vacuum, Surfaces, and Films*, 30(2):021602, 2012.

[93] Felix Sharipov and Dalton V. Kozak. Rarefied gas flow through a thin slit into vacuum simulated by the monte carlo method over the whole range of the knudsen number. *Journal of Vacuum Science & Technology A: Vacuum, Surfaces, and Films*, 27(3):479–484, 2009.

[94] G.A. Bird. *Molecular gas dynamics and the direct simulation of gas flows*. Clarendon Press, Oxford, 1994.

[95] Boris Smirnov. *Fundamentals of Ionized Gases*. Wiley, Weinheim, 2012.

[96] Shyjumon Ibrahimkutty. *Production, deposition and characterization of metal nanoclusters using a gas aggregation source*. PhD thesis, Ernst-Moritz-Arndt-Universität Greifswald, 2005.

[97] Y. Watanabe. Formation and behaviour of nano/micro-particles in low pressure plasmas. *Journal of Physics D: Applied Physics*, 39(19):R329, 2006.

[98] Boris M Smirnov. Cluster plasma. *Physics-Uspekhi*, 43(5):453, 2000.

[99] B. M. Smirnov. Processes in expanding and condensing gases. *Physics-Uspekhi*, 37(7):621–657, 1994.

[100] J. Goree. Ion trapping by a charged dust grain in a plasma. *Phys. Rev. Lett.*, 69:277–280, Jul 1992.

[101] Ruben Wiese, Vladimir Sushkov, Holger Kersten, Venkata R Ikkurthi, Ralf Schneider, and Rainer Hippler. Behavior of a porous particle in a radiofrequency plasma under pulsed argon ion beam bombardment. *New Journal of Physics*, 12(3):033036, 2010.

[102] T. E. Sheridan, M. J. Goeckner, and J. Goree. Observation of two-temperature electrons in a sputtering magnetron plasma. *Journal of Vacuum Science & Technology A: Vacuum, Surfaces, and Films*, 9(3):688–690, 1991.

[103] P Sigurjonsson and J T Gudmundsson. Plasma parameters in a planar dc magnetron sputtering discharge of argon and krypton. *Journal of Physics: Conference Series*, 100(6):062018, 2008.

[104] S. M. Rossnagel and H. R. Kaufman. Langmuir probe characterization of magnetron operation. *Journal of Vacuum Science & Technology A: Vacuum, Surfaces, and Films*, 4(3):1822–1825, 1986.

[105] S. M. Rossnagel and H. R. Kaufman. Current–voltage relations in magnetrons. *Journal of Vacuum Science and Technology A: Vacuum, Surfaces, and Films*, 6(2):223–229, 1988.

[106] M. J. Goeckner, J. Goree, and T. E. Sheridan. Laser-induced fluorescence characterization of ions in a magnetron plasma. *Journal of Vacuum Science & Technology A: Vacuum, Surfaces, and Films*, 8(6):3920–3924, 1990.

[107] Samuel D. Ekpe, Francisco J. Jimenez, David J. Field, Martin J. Davis, and Steven K. Dew. Effect of magnetic field strength on deposition rate and energy flux in a dc magnetron sputtering system. *Journal of Vacuum Science & Technology A: Vacuum, Surfaces, and Films*, 27(6):1275–1280, 2009.

[108] D. J. Field, S. K. Dew, and R. E. Burrell. Spatial survey of a magnetron plasma sputtering system using a langmuir probe. *Journal of Vacuum Science & Technology A: Vacuum, Surfaces, and Films*, 20(6):2032–2041, 2002.

[109] Petr Spatenka, Igor Leipner, Jaroslav Vlcek, and Jindrich Musil. A comparison of internal plasma parameters in a conventional planar magnetron and a magnetron with additional plasma confinement. *Plasma Sources Science and Technology*, 6(1):46, 1997.

[110] Sang-Hun Seo, Jung-Hwan In, and Hong-Young Chang. Measurements of electron energy distribution functions and electron transport in the downstream region of an unbalanced dc magnetron discharge. *Plasma Sources Science and Technology*, 13(3):409, 2004.

[111] R. Hippler, S. Wrehde, V. Stranak, O. Zhigalov, H. Steffen, M. Tichy, M. Quaas, and H. Wulff. Characterization of a magnetron plasma for deposition of titanium oxide and titanium nitride films. *Contributions to Plasma Physics*, 45(5-6):348–357, 2005.

[112] I. Petrov, V. Orlinov, I. Ivanov, and J. Kourtev. Electrostatic probe measurements in the glow discharge plasma of a d. c. magnetron sputtering system. *Contributions to Plasma Physics*, 28(2):157–167, 1988.

[113] I Ivanov, Sv Statev, V Orlinov, and R Shkevov. Electron energy distribution function in a dc magnetron sputtering discharge. *Vacuum*, 43(8):837 – 842, 1992.

[114] S. Bornholdt, J. Ye, S. Ulrich, and H. Kersten. Energy fluxes in a radio-frequency magnetron discharge for the deposition of superhard cubic boron nitride coatings. *Journal of Applied Physics*, 112(12):123301, 2012.

[115] Jaroslav Kousal, Oleksandr Polonskyi, Ondrej Kylian, Andrei Choukourov, Anna Artemenko, Josef Pesicka, Danka Slavinska, and Hynek Biederman. Characterization of nanoparticle flow produced by gas aggregation source. *Vacuum*, 96:32–38, 2013.

[116] David R. Lide, editor. *CRC Handbook of Chemistry and Physics*. CRC Press/Taylor and Francis, Boca Ralton, FL, 89th edition, 2009.

[117] W. Eckstein. Calculated sputtering, reflection and range values. Technical Report 9/132, IPP, 2002.

[118] R. Behrisch, editor. *Sputtering by Particle Bombardment I*. Springer Verlag Berlin Heidelberg New York, 1981.

[119] Tadayoshi Ono, Takahiro Kenmotsu, and Tetsuya Muramoto. Simulation of the sputtering process. In Diederik Depla and Stijn Mahieu, editors, *Reactive Sputter Deposition*, volume 109 of *Springer Series in Materials Science*, pages 1–42. Springer Berlin Heidelberg, 2008.

[120] J. L. Vossen and J. J. Cuomo. Glow discharge sputter deposition. In John L. Vossen and Werner Kern, editors, *Thin film processes*, pages 75–113. Academic Press, Inc., 24–28 Oval Road, London NW1 7DX, 1978.

[121] Srim software. `http://srim.org`.

[122] J.P. Biersack and W. Eckstein. Sputtering studies with the monte carlo program trim.sp. *Applied Physics A*, 34:73–94, 1984.

[123] N. Matsunami, Y. Yamamura, Y. Itikawa, N. Itoh, Y. Kazumata, S. Miyagawa, K. Morita, and R. Shimizu. A semiempirical formula for the energy dependence of the sputtering yield. *Radiation Effects*, 57(1–2):15–21, 1981.

[124] Y. Yamamura, N. Matsunami, and N. Itoh. Theoretical studies on an empirical formula for sputtering yield at normal incidence. *Radiation Effects*, 71(1-2):65–86, 1983.

[125] Y. Yamamura and Shigeru Shindo. An empirical formula for angular dependence of sputtering yields. *Radiation Effects*, 80(1–2):57–72, 1984.

[126] YASUNORI YAMAMURA and HIRO TAWARA. Energy dependence of ion-induced sputtering yields from monatomic solids at normal incidence. *Atomic Data and Nuclear Data Tables*, 62(2):149–253, 1996.

[127] Nils Laegreid and G. K. Wehner. Sputtering yields of metals for ar^+ and ne^+ ions with energies from 50 to 600 ev. *Journal of Applied Physics*, 32(3):365–369, 1961.

[128] P.J Kelly and R.D Arnell. Magnetron sputtering: a review of recent developments and applications. *Vacuum*, 56(3):159–172, 2000.

[129] Annemie Bogaerts, Evi Bultinck, Ivan Kolev, Laurent Schwaederl, Koen Van Aeken, Guy Buyle, and Diederik Depla. Computer modelling of magnetron discharges. *Journal of Physics D: Applied Physics*, 42(19):194018, 2009.

[130] T. Peter, S. Rehders, U. Schürmann, T. Strunskus, V. Zaporojtchenko, and F. Faupel. High rate deposition system for metal-cluster / $sio_xc_yh_z$-polymernanocomposite thin films. *Journal of Nanoparticle Research*, 15(6):1–8, 2013.

[131] W. Paul and H. Steinwedel. Ein neues massenspektrometer ohne magnetfeld. *Zeitschrift Naturforschung Teil A*, 8:448–450, 1953.

[132] P. H. Dawson. Principles of operation. In Peter H. Dawson, editor, *Quadrupole mass spectrometry and its applications*, pages 9–64. AIP Press, 1995.

[133] D. Bassi. Ionization detectors ii: Mass selection and ion detection. In Giacinto Scoles, editor, *Atomic and Molecular Beam Methods*, pages 180–192. Oxford University Press, 1988.

[134] W. Paul and M. Raether. Das elektrische massenfilter. *Zeitschrift für Physik A Hadrons and Nuclei*, 140:262–273, 1955. 10.1007/BF01328923.

[135] W. Paul, H. P. Reinhard, and U. von Zahn. Das elektrische massenfilter als massenspektrometer und isotopentrenner. *Zeitschrift für Physik*, 152:143–182, 1958.

[136] W.E Austin, A.E. Holme, and J.H. Leck. The mass filter: design and performance. In Peter H. Dawson, editor, *Quadrupole mass spectrometry and its applications*, pages 121–152. AIP Press, 1995.

[137] J.E. Campana. Elementary theory of the quadrupole mass filter. *International Journal of Mass Spectrometry and Ion Physics*, 33(2):101–117, 1980.

[138] Vladimir V. Titov. Detailed study of the quadrupole mass analyzer operating within the first, second, and third (intermediate) stability regions. i. analytical approach. *Journal of the American Society for Mass Spectrometry*, 9(1):50–69, 1998.

[139] N.V. Konenkov and J.T. Dowell. Transmission of the quadrupole mass filter in the intermediate stability zone separation mode. *International Journal of Mass Spectrometry and Ion Processes*, 164(3):201–206, 1997.

[140] Oxford Applied Research. *Quadrupole Mass Filter QMF200*.

[141] John Elvans Smith and Myra Lee Jordan. Mathematical and graphical interpretation of the log-normal law for particle size distribution analysis. *Journal of Colloid Science*, 19(6):549–559, 1964.

[142] K. Blaum, Ch. Geppert, P. Müller, W. Nrtershuser, K. Wendt, and B.A. Bushaw. Peak shape for a quadrupole mass spectrometer: comparison of computer simulation and experiment. *International Journal of Mass Spectrometry*, 202(1–3):81–89, 2000.

[143] Gianangelo Bracco. Comparison of quadrupole mass filters equipped with rods of different convexity: An analysis by finite element methods and trajectory simulations. *International Journal of Mass Spectrometry*, 278(1):75–88, 2008.

[144] Gianangelo Bracco. Comparison of quadrupole mass filters with hyperbolic and cylindrical rods working in the third stability zone. *International Journal of Mass Spectrometry*, 303(2–3):212–219, 2011.

[145] T.J. Hogan and S. Taylor. Performance simulation of a quadrupole mass filter operating in the first and third stability zones. *Instrumentation and Measurement, IEEE Transactions on*, 57(3):498–508, march 2008.

[146] Christian Bohm and Jerome Perrin. Retarding-field analyzer for measurements of ion energy distributions and secondary electron emission coefficients in low-pressure radio frequency discharges. *Review of Scientific Instruments*, 64(1):31–44, 1993.

[147] J. Arol Simpson. Design of retarding field energy analyzers. *Review of Scientific Instruments*, 32(12):1283–1293, 1961.

[148] D Gahan, S Daniels, C Hayden, P Scullin, D O'Sullivan, Y T Pei, and M B Hopkins. Ion energy distribution measurements in rf and pulsed dc plasma discharges. *Plasma Sources Science and Technology*, 21(2):024004, 2012.

[149] Tim Baloniak, Rüdiger Reuter, Christoph Flötgen, and Achim von Keudell. Calibration of a miniaturized retarding field analyzer for low-temperature plasmas: geometrical transparency and collisional effects. *Journal of Physics D: Applied Physics*, 43(5):055203, 2010.

[150] Tim Baloniak, Rüdiger Reuter, Christoph Flötgen, and Achim von Keudell. Calibration of a miniaturized retarding field analyzer for low-temperature plasmas: geometrical transparency and collisional effects. *Journal of Physics D: Applied Physics*, 43(5):055203, 2010.

[151] Vasile Vartolomei. *ECWR Plasma Parameter Characterisation and Tuning for Applications to Thin Film Deposition (Indium Oxide)*. PhD thesis, Ernst-Moritz-Arndt-Universität Greifswald, 2004.

[152] *Influence of grid position on retarding field energy analyzer parameters*, 2011. E. M. Khilkevitch and A. S. Smirnov, IX Workshop on Frontiers in Low Temperature Plasma Diagnostics.

[153] I.H. Hutchinson. *Principles of plasma diagnostics*. Cambridge University Press, 2002.

[154] K Ellmer, R Wendt, and K Wiesemann. Interpretation of ion distribution functions measured by a combined energy and mass analyzer. *International Journal of Mass Spectrometry*, 223224:679–693, 2003.

[155] J. W. Coburn. A system for determining the mass and energy of particles incident on a substrate in a planar diode sputtering system. *Review of Scientific Instruments*, 41(8):1219–1223, 1970.

[156] Nan Jiang, Ning Zhao, Hongfei Liu, and Tongzhen Fang. Mass-resolved retarding field energy analyzer and its measurement of ion energy distribution in helicon plasma. *Nuclear Instruments and Methods in Physics Research Section B: Beam Interactions with Materials and Atoms*, 229(34):508–518, 2005.

[157] S. G. Walton, R. F. Fernsler, and D. Leonhardt. Measurement of ion energy distributions using a combined energy and mass analyzer. *Review of Scientific Instruments*, 78(8):083503, 2007.

[158] Rainer Hippler, Jana Kredl, and Vasile Vartolomei. Ion energy distribution of an inductively coupled radiofrequency discharge in argon and oxygen. *Vacuum*, 83(4):732–737, 2008.

[159] M. Takebe and S. Kumashiro. Computer simulation of the quadrupole mass filter. *Nuclear Instruments and Methods in Physics Research Section A: Accelerators, Spectrometers, Detectors and Associated Equipment*, 363(12):411–415, 1995.

[160] Z. L. Wang. Transmission electron microscopy of shape-controlled nanocrystals and their assemblies. *The Journal of Physical Chemistry B*, 104(6):1153–1175, 2000.

[161] Gernot Friedbacher. Scanning probe microscopy. In H. Bubert and H. Jenett, editors, *Surface and Thin Film Analysis*, pages 276–290. Wiley-VCH Verlag GmbH, 2002.

[162] G. Binnig, C. F. Quate, and Ch. Gerber. Atomic force microscope. *Phys. Rev. Lett.*, 56:930–933, Mar 1986.

[163] Max Knoll. Aufladepotentiel und sekundäremission elektronenbestrahlter körper. *Zeitschrift für technische Physik*, 16:467–475, 1935.

[164] Manfred Ardenne. Das elektronen-rastermikroskop. theoretische grundlagen. *Zeitschrift für Physik*, 109:553–572, 1938.

[165] Manfred Ardenne. Das elektronen-rastermikroskop. praktische ausführung. *Zeitschrift für technische Physik*, 19:407–416, 1938.

[166] Debbie J Stokes. Principles of sem. In *Principles and Practice of Variable Pressure/Environmental Scanning Electron Microscopy (VP-ESEM)*, pages 17–62. John Wiley & Sons, Ltd, 2008.

[167] Joseph I. Goldstein, Dale E. Newbury, Patrick Echlin, David C. Joy, Charles Fiori, and Eric Lifshin. *Scanning Electron Microscopy and X-ray Microanalysis*. Plenum Press, New York and London, 1981.

[168] Henning Bubert and John C. Rivière. electron detection. In H. Bubert and H. Jenett, editors, *Surface and Thin Film Analysis*, pages 6–85. Wiley-VCH Verlag GmbH, 2002.

[169] J. Lindhard and M. Scharff. Energy dissipation by ions in the kev region. *Physical Review*, 124(1):128–130, 1961.

[170] M. P. Seah, C. A. Clifford, F. M. Green, and I. S. Gilmore. An accurate semi-empirical equation for sputtering yields i: for argon ions. *Surface and Interface Analysis*, 37(5):444–458, 2005.

List of Figures

List of Tables

Appendix A

Sputtering yield

A.1. Sputtering yield for normal incidence

According to [119, 124], sputtering yield of monoatomic solids for normal incidence of projectiles can be expressed with the following semi-empirical Yamamura formulae:

$$Y(E) = 0.042 \frac{Q(Z_t)\alpha\left(\frac{M_t}{M_i}\right)}{U_s} \frac{S_n(E)}{1 + \Gamma k_e \varepsilon^{0.3}} \left[1 - \sqrt{\frac{E_{th}}{E}}\right]^s \tag{A.1}$$

where E is a projectile energy, M_i, M_t are the masses of a projectile and a target atom in a.m.u., respectively, and the numerical factor in units of Å^{-2}. The factor Γ has the form:

$$\Gamma = \frac{W(Z_t)}{1 + \left(\frac{M_i}{7}\right)^3} \tag{A.2}$$

U_s is the surface binding energy of the target material, $W(Z_t)$, $Q(Z_t)$, s — are dimensionless parameters, tabulated in [126]. For Cu targets these parameters are:

$$U_s = 3.49;\ Q = 1.0;\ W = 0.73;\ s = 2.5 \tag{A.3}$$

The best-fit values of α are described in the following manner [119]:

$$\alpha\left(\frac{M_t}{M_i}\right) = \begin{cases} 0.249\left(\frac{M_t}{M_i}\right)^{0.56} + 0.0035\left(\frac{M_t}{M_i}\right)^{1.5} & \text{if } M_i \le M_t, \\ 0.0875\left(\frac{M_t}{M_i}\right)^{-0.15} + 0.165\left(\frac{M_t}{M_i}\right) & \text{if } M_i \ge M_t. \end{cases} \tag{A.4}$$

E_{th} is the sputtering threshold energy and is expressed by the following best-fit functional relation:

$$\frac{E_{th}}{U_s} = \begin{cases} \frac{6.7}{\gamma} & \text{if } M_i \ge M_t, \\ \frac{1+5.7(M_i/M_t)}{\gamma} & \text{if } M_i \le M_t. \end{cases} \tag{A.5}$$

Where γ is energy transfer factor in elastic collision defined as:

$$\gamma = \frac{4M_iM_t}{(M_i + M_t)^2} \tag{A.6}$$

k_e is the Lindhard electronic stopping coefficient [169]:

$$k_e = \frac{0.079\,(M_i + M_t)^{\frac{3}{2}}\, Z_i^{\frac{2}{3}} Z_t^{\frac{1}{2}}}{M_i^{\frac{3}{2}} M_t^{\frac{1}{2}} \left(Z_i^{\frac{2}{3}} + Z_t^{\frac{2}{3}}\right)^{\frac{3}{4}}} \tag{A.7}$$

$S_n(E)$ is a nuclear stopping cross section in units eV*Å^2 per atom:

$$S_n(E) = \frac{84.78 \cdot Z_i \cdot Z_t}{\left(Z_i^{\frac{2}{3}} + Z_t^{\frac{2}{3}}\right)^{\frac{1}{2}}} \frac{M_i}{M_i + M_t} s_n^{TF}(\varepsilon) \tag{A.8}$$

ε is reduced LSS energy in eV [169]:

$$\varepsilon(E) = \frac{0.03255 \cdot E \cdot M_t}{(M_i + M_t)\, Z_i Z_t \sqrt{Z_i^{\frac{2}{3}} + Z_t^{\frac{2}{3}}}} \tag{A.9}$$

s_n^{TF} is reduced nuclear stopping cross section approximated by an analytic fit to the Thomas-Fermi potential [125]:

$$s_n^{TF}(\varepsilon) = \frac{3.441\sqrt{\varepsilon}\log\left(\varepsilon + 2.718\right)}{1 + 6.355\sqrt{\varepsilon} + \varepsilon\left(6.882\sqrt{\varepsilon} - 1.708\right)} \tag{A.10}$$

A.2. Angular dependence of sputtering yield

The semi-empirical formula of dependency of the sputtering yield on the projectile incident angle was first presented by Yamamura [124, 125] and later improved by Seah [170]. According to [170]:

$$Y(E,\theta) = Y(E,0) \cdot (\cos\theta)^{-f} \exp\left[-f \cdot \cos\theta_{\text{opt}} \cdot \left(\frac{1}{\cos\theta} - 1\right)\right] \tag{A.11}$$

where order of unity f expressed as:

$$f = f_s \cdot \left(1 + 2.5 \cdot \frac{\sqrt{\frac{E_{th}}{E}}}{1 - \sqrt{\frac{E_{th}}{E}}}\right) \tag{A.12}$$

Seah [170] provides a good description for f_s with the maximum error of 1% and a standard deviation below 0.5%:

$$f_s = 1.747 + 0.885 \cdot \left(\frac{M_t}{100}\right) - 2.588 \cdot \left(\frac{M_t}{100}\right)^2 + 2.263 \cdot \left(\frac{M_t}{100}\right)^3 - 0.899 \cdot \left(\frac{M_t}{100}\right)^4 + 0.136 \cdot \left(\frac{M_t}{100}\right)^5 \tag{A.13}$$

θ_{opt} is the angle of incidence for the maximum emission yield:

$$\theta_{\text{opt}} = 90^\circ - 286.0\Psi^{0.45} \tag{A.14}$$

where

$$\Psi = \left(\frac{a_{12}}{r}\right)^{1.5} \cdot \left[\frac{Z_i \cdot Z_t}{\sqrt{Z_i^{2/3} + Z_t^{2/3}} \cdot E}\right]^{0.5} \tag{A.15}$$

Where r is the average interatomic spacing in nm:

$$r^3 = \frac{10^{24} M_t}{\rho \cdot N_A} \tag{A.16}$$

where N_A is Avogadro's number and ρ is the target density in kg·m^{-3}.
Parameter a_{12} is given by:

$$a_{12} = \left(\frac{9\pi^2}{128}\right)^{\frac{1}{3}} \cdot \frac{a_0}{\sqrt{Z_i^{2/3} + Z_t^{2/3}}} \tag{A.17}$$

where $a_0 = 0.053$ nm is the Bohr radius.

Appendix B

Remote control

Fig. B.1 shows the operator panel of the Labview software developed to control the experimental parameters of the nanocluster source. The discharge control section accounts for the setting of the discharge current and voltage. The mass flow control section allows for controlling the two channels of MKS 247 4 Channel readout, to set the gas flow rate. The temperature control section contains the indicator of the current temperature measured by the thermocouple, the temperature threshold, (i.e. the desired temperature), and the desired accuracy (delta field). The QMF Setup section accounts for the QMF settings, i.e. frequency and amplitude of the AC voltage, and for the resolution. The measured mass spectrum is plotted on the right-hand side, which is also where the control buttons to start and stop the mass spectra measurement are placed. The pressure section contains the pressure indicators for all connected pressure gauges (1, 2, 3 in Fig. 3.4). The Keithley setup section allows for setting the bias voltage if needed. All sections are designed to be independent from each other, so that disconnection of for example the QMF does not influence the control other experimental parameters.

Figure B.2 schematically presents the details of the control unit box developed in the present work. Left: pinouts of Meilhaus ME-3000 and ADLINK PCI6216 measurement cards. Center: photo of the box containing the electronics and electronic circuits used to obtain the temperature from the thermocouple, to control the magnet valve for cooling of the chamber walls by liquid nitrogen, and to control the power supply. Right: pictures of the controlled devices.

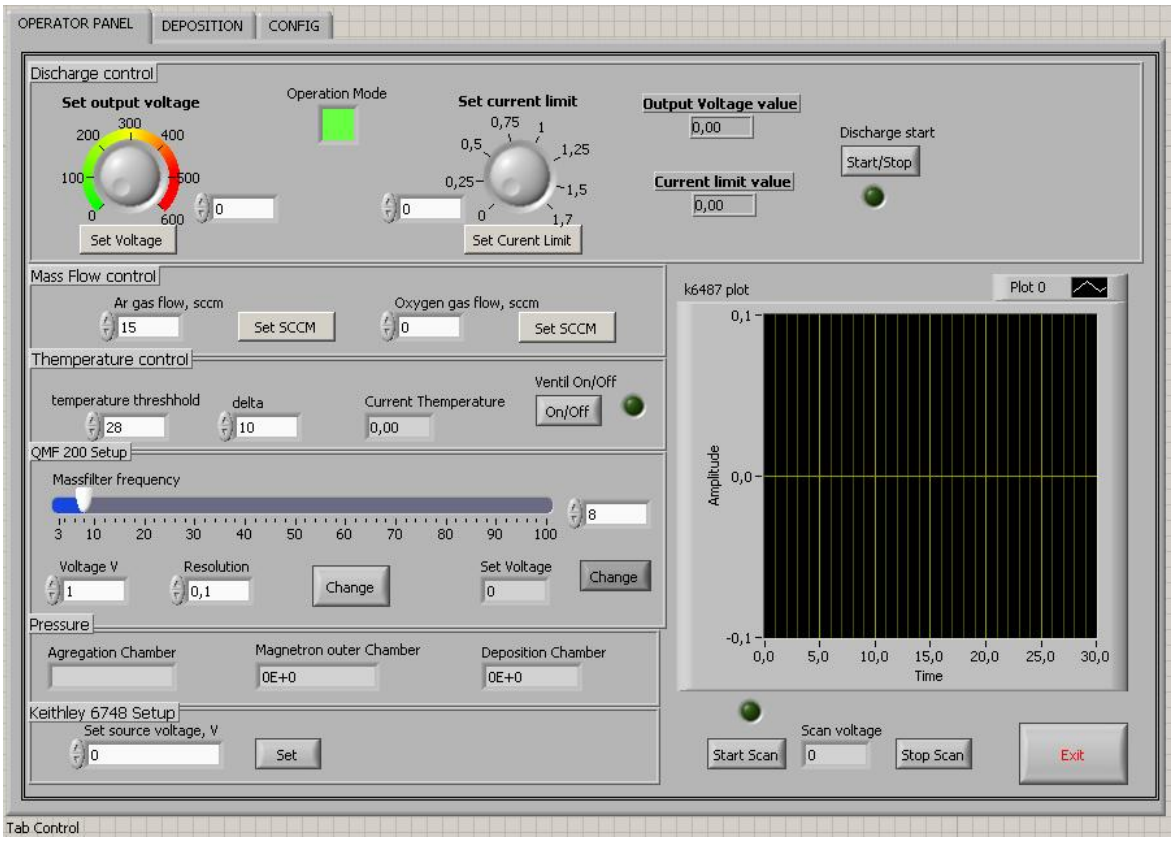

Figure B.1.: Operator panel of the Labview software developed to control the experimental parameters of the nanocluster source.

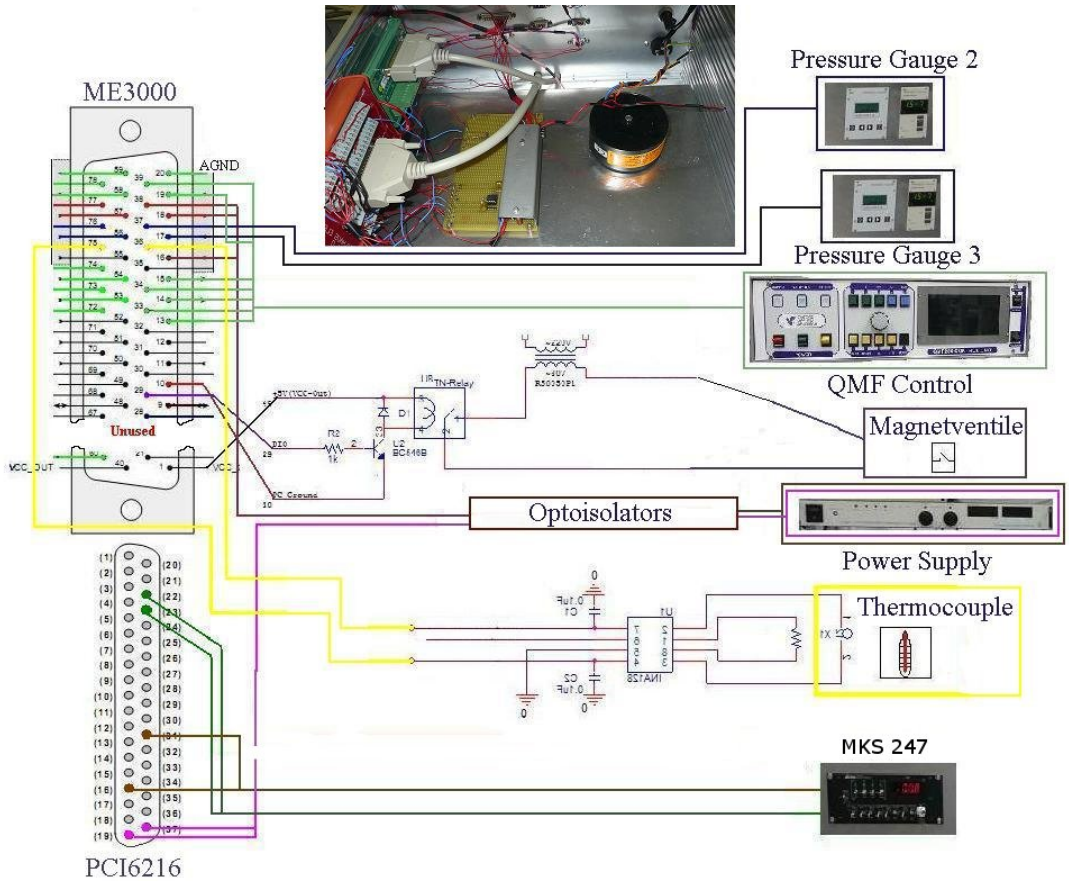

Figure B.2.: Schematics of the remote control unit developed in the present work. Left: pinouts of Meilhaus ME-3000 and ADLINK PCI6216 measurement cards. Center: photo of the box containing the electronics and electronic circuits. Right: controlled devices. Thanks to Anastasia Schiller for this picture.

Appendix C

Selbständigkeitserklärung

Hiermit erkläre ich, dass diese Arbeit bisher von mir weder an der Mathematisch-Naturwissenschaftlichen Fakultät der Ernst-Moritz-Arndt-Universität Greifswald noch einer anderen wissenschaftlichen Einrichtung zum Zwecke der Promotion eingereicht wurde.

Ferner erkläre ich, dass ich diese Arbeit selbständig verfasst und keine anderen als die darin angegebenen Hilfsmittel und Hilfen benutzt und keine Textabschnitte eines Dritten ohne Kennzeichnung übernommen habe.

Greifswald, den 18.03.2013 Marina Ganeva

Appendix D

Peer-Review Publications

1. A. Rai, A. Mutzke, G. Bandelow, R. Schneider, **M. Ganeva**, A. V. Pipa, and R. Hippler:
   Operational limit of a planar DC magnetron cluster source due to target erosion
   Nucl. Instrum. Meth. B, **submitted**, (2013).

2. **M. Ganeva**, A. V. Pipa, B. M. Smirnov, P. V. Kashtanov, and R. Hippler:
   Velocity distribution of mass-selected nano-size cluster ions
   Plasma Sources Sci. Technol., **22**, 045011, (2013).

3. G. Karapetyan, **M. Ganeva**, and R. Hippler:
   Directional sensitivity of MuSTAnG muon telescope
   Journal of Space Weather and Space Climate, **3**, A16, (2013).

4. **M. Ganeva**, S. Peglow, R. Hippler, M. Berkova, and V. Yanke:
   Seasonal variations of the muon flux seen by muon telescope MuSTAnG
   Journal of Physics: Conference Series, **409**(1), 012242, (2013).

5. **M. Ganeva**, A. V. Pipa, and R. Hippler:
   The influence of target erosion on the mass spectra of clusters formed in the planar DC magnetron sputtering source
   Surface and Coatings Technology, **213**, 41–47, (2012).

6. **M. Ganeva**, T. Peter, S. Bornholdt, H. Kersten, T. Strunskus, V. Zaporojtchenko, F. Faupel, and R. Hippler
   Mass Spectrometric Investigations of Nano-Size Cluster Ions Produced by High Pressure Magnetron Sputtering
   Contributions to Plasma Physics, **52** (10), 881–889, (2012).

7. A. Majumdar, D. Köpp, **M. Ganeva**, D. Datta, S. Bhattacharyya, and R. Hippler
   Development of metal nanocluster ion source based on dc magnetron plasma sputtering at room temperature
   Review of Scientific Instruments, **80** (9), 095103 (2009).

8. A. Majumdar, **M. Ganeva**, D. Köpp, D. Datta, P. Mishra, S. Bhattacharyya, D. Ghose, and R. Hippler
   Surface morphology and composition of films grown by size-selected Cu nanoclusters
   Vacuum, **83** (4), 719–723, (2008).

Appendix E

Conference contributions

E.1. Poster

- M. Ganeva, A. V. Pipa, and R. Hippler, "Measurement of ion velocity distributions (IVDFs) of mass selected nano-sized cluster ions". DPG Frühjahrstagung, 25th of February – 1st of March 2013, Jena, Germany.

- M. Ganeva and R. Hippler, "Velocity distributions of mass selected nanoclusters produced by DC magnetron gas aggregation source". 16. Fachtagung für Plasmatechnologie, 18–20 of February 2013, Greifswald, Germany.

- M. Ganeva, T. Peter, S. Bornholdt, M. Fröhlich, H. Kersten, T. Strunskus, V. Zaporojtchenko, F. Faupel and R. Hippler, "Influence of He:Ar ratio on the size distribution of cluster ions produced by high pressure magnetron sputtering". 13th International Conference on Plasma Surface Engineering, September 10–14, 2012, Garmisch-Partenkirchen, Germany.

- M. Ganeva and R. Hippler, "Velocity of mass-selected Cu nanoclusters produced in the DC magnetron nanocluster source". 3rd Graduate Summer Institute *Complex Plasmas*, 30th of July – 8th of August 2012, South Orange, NJ (USA).

- M. Ganeva, S. Peglow, R. Hippler, M. Berkova, and V. Yanke, "Seasonal variations of the muon flux seen by muon telescope MuSTAnG". 23rd European Cosmic Ray Symposium, 3–7 of July, 2012, Moscow, Russia.

- M. Ganeva, A. V. Pipa, and R. Hippler, "Variation of cluster size distribution with target aging measured in planar DC magnetron sputtering source". DPG Frühjahrstagung, 12–16 of March 2012, Stuttgart, Germany.

- T. K. Kim, M. Ganeva, J. Reich, and S. Wolff, "Analysis of the Hinode Magnetograms". Presented at Wernher von Braun Memorial Symposium, October 24-26 2011, UAHuntsville, USA.

- M. Ganeva, T. Peter, S. Bornholdt, H. Kersten, T. Strunskus, V. Zaporojtchenko, F. Faupel and R. Hippler, "Measurement of size distribution of cluster beam produced by high pressure magnetron sputtering". International Workshop *Physics of Complex Plasmas*, Potsdam, September 26–28, 2011.

- M. Ganeva and R. Hippler, "Measurement of IEDF of mass-selected nanoclusters produced in a gas aggregation DC magnetron discharge". Presented at IX Workshop on Frontiers in Low Temperature Plasma Diagnostics, 9–12 of May 2011, Greifswald/Zinnowitz, Germany.

- M. Ganeva and R. Hippler "Stability of cluster formation in a DC magnetron sputtering source". DPG Frühjahrstagung, 28–31 of March 2011, Kiel, Germany.

- R. Hippler, V. Stranak and M. Ganeva. "Growth and dynamics of particles in plasmas". SFB-TR24 Meeting, November 2008, Greifswald

- A. Majumdar, M. Ganeva, D. Köpp, D. Datta, P. Mishra, S. R. Bhattacharayya, D. Ghose, R. Hippler,"Surface morphology and composition of films grown by size-selected Cu-nanoclusters". Symposium on Vacuum based Science and Technology (5-7 September, 2007, Greifswald, Germany) P13

- G. V. Zhuvikin, M. Ganeva "The morphological study and characterization of cluster structures produced by the plasma polymerization deposition". Presented at the International Wilhelm and Else Heraeus Summerschool on Computational Many-Particle Physics.

E.2. Talks

- M. Ganeva, R. Hippler, "Velocity of mass-selected Cu nanoclusters". 3rd Graduate Summer Institute *Complex Plasmas*, 30th of July – 8th of August 2012, South Orange, NJ (USA).

- M. Ganeva, T. K. Kim, J. Reich, S. Wolff, "Analysis of the Hinode Magnetograms". 1st Joint Space Weather Summer Camp, 17th of July – 14th of August 2011, UAHuntsville, USA.

- M. Ganeva, R. Hippler, "Stability of cluster formation in a DC magnetron sputtering source". German-Czech Workshop on Formation of Nanoparticles in Plasmas, 4–6 of April 2011, St.-Peter Ording, Germany.

Appendix F

Lebenslauf

Marina Ganeva

Felix-Hausdorff-Str. 6
17489 Greifswald
+49 3834 864783
ganeva@gmail.com

F.1. Berufserfahrung

11/2005–09/2013	Institut für Physik, EMAU Greifswald, Felix-Hausdorff-Str. 6, 17489 Greifswald: wissenschaftliche Mitarbeiterin. Schwerpunkte: Magnetron Sputtern, Massenspektrometrie (QMF), Plasmadiagnostik, Nanopartikel Bildung und Beschichtung; Softwareentwicklung für Experimentsteuerung und Datenanalyse: Labvew, Wolfram Mathematica, Igor Pro, C++, Python.
02/2004–10/2005	Mobile Information Technologies, Sankt Petersburg, Russland: UNIX System Administrator/Software developer. Schwerpunkte: Red Hat Linux, ALT Linux, Free BSD, Radlinux, C, C++, Python, PHP, Perl, MySQL, PostgreSQL, XML/XSLT; CVS, SVN.

F.2. Ausbildung

11/2005–06/2013	Ernst-Moritz-Arndt Universität Greifswald: Promotion in Arbeitsgruppe Prof. Dr. Rainer Hippler. Promotionsthema: "Formation of metal nano-size clusters with a DC magnetron-based gas aggregation source". Note: *sehr gut*.
08/2001–02/2004	Staatliche Universität Sankt Petersburg, Russland: Masterarbeit (Atom und Molekülphysik). Thema: "Untersuchung der Morphologie von durch Plasmabeschichtung erzeugten Cluster-Strukturen". Note: *sehr gut*.
08/1996–07/2001	Staatliche Universität Sankt Petersburg, Russland: Bachelorarbeit (Optik und Spektroskopie). Thema: "Untersuchung der Transformation photometrischer Größen der Abbildung in komplexen optischen Systemen". Note: *sehr gut*.
08/1994–07/1996	Akademische Gymnasium (Internat No.45) der Staatlichen Universität der Stadt Sankt Petersburg, Russland. Abslussarbeit zum Thema "Die Anwendung von Interferenz-Techniken zur Untersuchung des Stoffwechsels von wirbellosen, quasistationären Wasserorganismen". Note: *sehr gut*.

F.3. Teilnahme an der Sommerschule

- 3rd Graduate Summer Institute *Complex Plasmas*, 30th of July – 8th of August 2012, South Orange, NJ (USA).
- *1st Joint Space Weather Summer Camp*, 17th of July – 14th of August 2011, Neustrelitz-Kühlungsborn-Rostock-Juliusruh-Greifswald (Germany), Huntsville and Boulder (USA).
- European Summer School *Plasma Applications in Material Science (PAMS)*, 16th–27th of August 2010, Greifswald, Germany.
- Greifswald-Hoboken-Kiel Summer Institute *Complex Plasmas*, 5th–13th of August 2010, Greifswald, Germany.
- International Wilhelm und Else Heraeus Summer School on *Computarional Many-Particle Physics*, 18th–29th of September 2006, Greifswald, Germany.

Acknowledgment

First and foremost I would like to express my sincerest gratitude to Prof. Dr. Rainer Hippler for giving me an opportunity to do my Ph.D. in his group at the Institute of Physics and for his guidance to my work. I also gratefully appreciate the financial support for my work by the University of Greifswald and by the DFG through SFB-TR24 "Fundamentals of Complex Plasmas".

I am especially indebted to my friend and colleague Dr. Andrei Pipa for our hot, long, stimulating and inspiring discussions, his co-authorship, and his kind support. I thank my children, Alisa and Kirill, because their smiles make me happy. I acknowledge the support of my husband, who took care of our children when I attended conferences and who allowed me to work on my thesis. I cannot find words to express my gratitude to Dr. med. habil. S.M. Schmidt, Dr. med. habil. R. Bruns, and to the pediatric surgery department of the University Hospital of Greifswald for saving the life and health of my daughter in 2005–2007 when she was seriously ill. Without them, I would not have been able to complete this thesis.

I would like to thank Dr. Vasile Vartolomei for teaching me about probe diagnostics, Dr. Vit Stranak for helping me to repair the magnetron, and both for valuable discussions. This thesis would not have been possible without the technical support of Axel Knuth, Robert Mrotzek, Michael Beck and Henrik Kotzan. I am happy have the opportunity to express my gratitude to Dr. Ruslan Kozakov, Dr. Pavel Kudrna, and Wladimir and Anastasia Schiller for their invaluable help with the electronics during the development of the NC-200 remote control. I would also like to thank Sergey Klemeshev for teaching me about the basics of electronics. It has helped me a lot in the work for my thesis. Many thanks to Sven Bornholdt and Tilo Peter. I enjoyed our team-work very much!

My sincerest thanks and appreciation to Prof. Boris Smirnov and Dr. Pavel Kashtanov for our fruitful discussions, their co-authorship, and their support with the theoretical analysis. I am indebted to Prof. Dr. Helm and Dr. Oxana Ivanova for the AFM measurements and their valuable advices. I am also thankful to Prof. Dr. Wulff and Dr. Marion Quaas for the GIXRD measurements.

I am also indebted to Peter Poete, Dr. Nazirah Jetha (organizers), DLR, the University of Huntsville (Alabama, USA) and the government of Mecklenburg-Vorpommern

(financial support) for giving me the incredible opportunity to attend the 1st Joint Space Weather Summer Camp. It was unforgettable experience! I also thank Ann-Pierra Herrendorf for her help with the maintainance of the muon telescope MuSTAnG.

Finally, I would like to express my deepest gratitude to all my friends, colleagues, and co-authors from Greifswald, Kiel, Russia, Poland and the Czech Republic, for the warm and friendly working atmosphere, the interesting discussions, valuable comments, proofreading of my German texts, and the pleasure of team-work.